

DTIC FILE COPY

SECURITY CLASSIFICATION OF THIS PAGE

REPORT DOCUMENTATION PAGE

Form Approved
OMB No. 0704-01881a. REPORT SECURITY CLASSIFICATION
UNCLASSIFIED

1b. RESTRICTIVE MARKINGS

NONE

2a. SECURITY CLASSIFICATION AUTHORITY

3. DISTRIBUTION / AVAILABILITY OF REPORT
APPROVED FOR PUBLIC RELEASE;
DISTRIBUTION UNLIMITED.

AD-A217 455

5. MONITORING ORGANIZATION REPORT NUMBER(S)
AFIT/CI/CIA-89-1116a. NAME OF PERFORMING ORGANIZATION
AFIT STUDENT AT
TX A&M Univ6b. OFFICE SYMBOL
(if applicable)7a. NAME OF MONITORING ORGANIZATION
AFIT/CIA

6c. ADDRESS (City, State, and ZIP Code)

7b. ADDRESS (City, State, and ZIP Code)

Wright-Patterson AFB OH 45433-6583

8a. NAME OF FUNDING / SPONSORING
ORGANIZATION8b. OFFICE SYMBOL
(if applicable)

9. PROCUREMENT INSTRUMENT IDENTIFICATION NUMBER

8c. ADDRESS (City, State, and ZIP Code)

10. SOURCE OF FUNDING NUMBERS

PROGRAM
ELEMENT NO.PROJECT
NO.TASK
NO.WORK UNIT
ACCESSION NO.

11. TITLE (Include Security Classification) (UNCLASSIFIED)

ROTORDYNAMIC ANALYSIS WITH SHELL ELEMENTS FOR THE TRANSFER MATRIX METHOD

12. PERSONAL AUTHOR(S)

EDWARD ANTHONY L'ANTIGUA

13a. TYPE OF REPORT

THESIS/DISSERTATION

13b. TIME COVERED

FROM TO

14. DATE OF REPORT (Year, Month, Day)

1989

15. PAGE COUNT

154

16. SUPPLEMENTARY NOTATION

APPROVED FOR PUBLIC RELEASE IAW AFR 190-1

ERNEST A. HAYGOOD, 1st Lt, USAF

Executive Officer, Civilian Institution Programs

17. COSATI CODES

FIELD

GROUP

SUB-GROUP

18. SUBJECT TERMS (Continue on reverse if necessary and identify by block number)

19. ABSTRACT (Continue on reverse if necessary and identify by block number)

DTIC
S ELECTE D
FEB 01 1990
Des

90 02 01 033

20. DISTRIBUTION / AVAILABILITY OF ABSTRACT

☒ UNCLASSIFIED/UNLIMITED ☐ SAME AS RPT. ☐ DTIC USERS

21. ABSTRACT SECURITY CLASSIFICATION

UNCLASSIFIED

22a. NAME OF RESPONSIBLE INDIVIDUAL

ERNEST A. HAYGOOD, 1st Lt, USAF

22b. TELEPHONE (Include Area Code)

(513) 255-2259

22c. OFFICE SYMBOL

AFIT/CI

ABSTRACT

Rotordynamic Analysis with Shell Elements
for the Transfer Matrix Method. (August 1989)

Edward Anthony L'Antigua, B.M.E., The Georgia Institute of Technology

Chair of Advisory Committee: Dr. Jorgen L. Nikolajsen

Shell finite elements were used to model conical sections with a range in parameters; axial length, radius, wall thickness, cone angle and Young's modulus. The parameters were chosen to cover the complete range of rotors, casings, and housings used throughout the turbomachinery industry. Flexibility coefficients were generated for these structures. The need for these flexibilities to be used in the current day rotordynamics transfer matrix computer programs is demonstrated. The flexibility coefficients are presented in nondimensional tables and plots for ease in use by turbomachinery design engineers and analysts in industry. *Thesis h2*

Accession For	
NTIS CR&I	<input checked="" type="checkbox"/>
DTIC TAB	<input type="checkbox"/>
Unannounced	<input type="checkbox"/>
Justification	
By	
Date	
Author(s)	
Title	
Subject	
A-1	



ROTORDYNAMIC ANALYSIS WITH SHELL ELEMENTS
FOR THE TRANSFER MATRIX METHOD

A Thesis

by

EDWARD ANTHONY L'ANTIGUA

Submitted to the Office of Graduate Studies of
Texas A&M University
in partial fulfillment of the requirements for the degree of

MASTER OF SCIENCE

August 1989

Major Subject: Mechanical Engineering


ROTORDYNAMIC ANALYSIS WITH SHELL ELEMENTS
FOR THE TRANSFER MATRIX METHOD

A Thesis

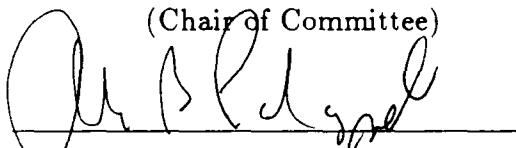
by

EDWARD ANTHONY L'ANTIGUA

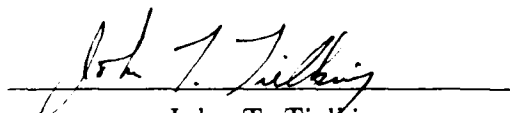
Approved as to style and content by:


Jorgen L. Nikolajsen


(Chair of Committee)


Alan B. Palazzolo

(Member)


John T. Tielking

(Member)


for Michael J. Rabins

(Head of Department)

August 1989

DEDICATION

I, in honor of, dedicate this work to my parents who gave their lives for my brothers, my sisters and me. I love them.

ACKNOWLEDGEMENTS

I am grateful to the U.S. Air Force and the common people of these United States of America who have made this research possible.

I gratefully acknowledge Dr. Jorgen L. Nikolajsen for his consistent kindness and extraordinarily good direction in the completion of this work.

I am very pleased to acknowledge my brothers in Christ, Vinai Rojanavanich for the text typing of this work. Murray E. Moore for his work on the plots and diagrams, and J. Howard Kelly for the use of his transfer matrix program and guidance for the demonstration herein.

Most importantly, I need to praise Almighty God my Savior, Jesus Christ, without whom, none of any of this would be possible; He gave me life when I had none.

TABLE OF CONTENTS

	Page
ABSTRACT	iii
DEDICATION	iv
ACKNOWLEDGEMENTS	v
TABLE OF CONTENTS	vi
LIST OF TABLES	viii
LIST OF FIGURES	xii
NOMENCLATURE	xix
1. INTRODUCTION	1
2. THEORETICAL BACKGROUND	5
2.1 Field Transfer Matrix Development	6
2.1.1 General Structure Element	9
2.1.2 Timoshenko Beam Element	10
2.1.3 Cantilevered Structure Flexibilities	11
2.1.4 Cantilevered Beam Flexibilities	11
2.1.5 Shaft-Beam Convergence	11
2.1.6 Conical Flexibility Transformation	12
2.2 Point Transfer Matrix for Conical Sections	16
2.2.1 Lumped Masses and Polar Moments of Inertia	18
2.2.2 Lumped Diametral Moments of Inertia	20
2.3 Shell Theory	21
2.3.1 Shells of Revolution	21
2.3.2 Finite Element Solution	23
3. OVALIZATION RESEARCH	26
3.1 Ovalization of Shells of Revolution	26

	Page
3.2 Computational Analysis	33
3.3 Experimental Verification	37
3.4 Ovalization Conclusions	39
3.5 Additional Comments	40
4. FINITE ELEMENT COMPUTATIONAL ANALYSIS	41
4.1 Models Defined	41
4.2 Boundary Conditions	43
4.3 Mesh Analysis	43
5. NUMERICAL RESULTS AND DISCUSSION	56
5.1 Negligible Ovalization	57
5.2 Design Data Generation	58
5.3 Model Verification	102
5.3.1 Cantilevered Cylinders	102
5.3.2 Conical Flexibility Transformations	117
5.4 Including Shear in Beam Theory	118
5.5 Rotor Transfer Matrix Demonstrations	126
5.5.1 60° Cone Test Piece	127
5.5.2 Space Shuttle Main Engine High Pressure Oxidizer Turbopump (SSME HPOTP)	131
6. CONCLUSION	137
REFERENCES	138
APPENDIX A	142
APPENDIX B	145
APPENDIX C	148
APPENDIX D	152
VITA	154

LIST OF TABLES

	Page
Table 1. Nondimensional Ovalization ($\frac{\Delta w}{t}$) for Thin Cylindrical Shells Under Varying Bending Load with $(\frac{t}{r}) = .01$, and Varying $(\frac{l}{r})$ ratio.	36
Table 2. Nondimensional Flexibilities (aEr) for Cylindrical Sections ($\theta = 0$) with Varying $(\frac{l}{r})$ and $(\frac{t}{r})$ Ratios.	59
Table 3. Nondimensional Flexibilities ($bEr^2 = \alpha Er^2$) for Cylindrical Sections ($\theta = 0$) with Varying $(\frac{l}{r})$ and $(\frac{t}{r})$ Ratios.	60
Table 4. Nondimensional Flexibilities (βEr^3) for Cylindrical Sections ($\theta = 0$) with Varying $(\frac{l}{r})$ and $(\frac{t}{r})$ Ratios.	61
Table 5. Nondimensional Flexibilities (aEr) for Conical Sections with $(\frac{t}{r}) = .0125$, Varying θ , and Varying $(\frac{l}{r})$ Ratio.	62
Table 6. Nondimensional Flexibilities (aEr) for Conical Sections with $(\frac{t}{r}) = .025$, Varying θ , and Varying $(\frac{l}{r})$ Ratio.	63
Table 7. Nondimensional Flexibilities (aEr) for Conical Sections with $(\frac{t}{r}) = .05$, Varying θ , and Varying $(\frac{l}{r})$ Ratio.	64
Table 8. Nondimensional Flexibilities (aEr) for Conical Sections with $(\frac{t}{r}) = .1$, Varying θ , and Varying $(\frac{l}{r})$ Ratio.	65
Table 9. Nondimensional Flexibilities (aEr) for Conical Sections with $(\frac{t}{r}) = .2$, Varying θ , and Varying $(\frac{l}{r})$ Ratio.	66
Table 10. Nondimensional Flexibilities ($bEr_{+\theta}^2 = \alpha Er_{-\theta}^2$) for Conical Sections with $(\frac{t}{r}) = .0125$, Varying θ , and Varying $(\frac{l}{r})$ Ratio.	67

Page

Table 11.	Nondimensional Flexibilities ($bEr_{+\theta}^2 = \alpha Er_{-\theta}^2$) for Conical Sections with $(\frac{t}{r}) = .025$, Varying θ , and Varying $(\frac{l}{r})$ Ratio.	68
Table 12.	Nondimensional Flexibilities ($bEr_{+\theta}^2 = \alpha Er_{-\theta}^2$) for Conical Sections with $(\frac{t}{r}) = .05$, Varying θ , and Varying $(\frac{l}{r})$ Ratio.	69
Table 13.	Nondimensional Flexibilities ($bEr_{+\theta}^2 = \alpha Er_{-\theta}^2$) for Conical Sections with $(\frac{t}{r}) = .1$, Varying θ , and Varying $(\frac{l}{r})$ Ratio.	70
Table 14.	Nondimensional Flexibilities ($bEr_{+\theta}^2 = \alpha Er_{-\theta}^2$) for Conical Sections with $(\frac{t}{r}) = .2$, Varying θ , and Varying $(\frac{l}{r})$ Ratio.	71
Table 15.	Nondimensional Flexibilities ($\alpha Er_{+\theta}^2 = bEr_{-\theta}^2$) for Conical Sections with $(\frac{t}{r}) = .0125$, Varying θ , and Varying $(\frac{l}{r})$ Ratio.	72
Table 16.	Nondimensional Flexibilities ($\alpha Er_{+\theta}^2 = bEr_{-\theta}^2$) for Conical Sections with $(\frac{t}{r}) = .025$, Varying θ , and Varying $(\frac{l}{r})$ Ratio.	73
Table 17.	Nondimensional Flexibilities ($\alpha Er_{+\theta}^2 = bEr_{-\theta}^2$) for Conical Sections with $(\frac{t}{r}) = .05$, Varying θ , and Varying $(\frac{l}{r})$ Ratio.	74
Table 18.	Nondimensional Flexibilities ($\alpha Er_{+\theta}^2 = bEr_{-\theta}^2$) for Conical Sections with $(\frac{t}{r}) = .1$, Varying θ , and Varying $(\frac{l}{r})$ Ratio.	75

Table 19.	Nondimensional Flexibilities ($\alpha Er_{+\theta}^2 = bEr_{-\theta}^2$) for Conical Sections with $(\frac{t}{r}) = .2$, Varying θ , and Varying $(\frac{l}{r})$ Ratio.	76
Table 20.	Nondimensional Flexibilities (βEr^3) for Conical Sections with $(\frac{t}{r}) = .0125$, Varying θ , and Varying $(\frac{l}{r})$ Ratio.	77
Table 21.	Nondimensional Flexibilities (βEr^3) for Conical Sections with $(\frac{t}{r}) = .025$, Varying θ , and Varying $(\frac{l}{r})$ Ratio.	78
Table 22.	Nondimensional Flexibilities (βEr^3) for Conical Sections with $(\frac{t}{r}) = .05$, Varying θ , and Varying $(\frac{l}{r})$ Ratio.	79
Table 23.	Nondimensional Flexibilities (βEr^3) for Conical Sections with $(\frac{t}{r}) = .1$, Varying θ , and Varying $(\frac{l}{r})$ Ratio.	80
Table 24.	Nondimensional Flexibilities (βEr^3) for Conical Sections with $(\frac{t}{r}) = .2$, Varying θ , and Varying $(\frac{l}{r})$ Ratio.	81
Table 25.	Cantilevered Cylinder Displacements Comparison of A.S.M. method with F.E.M.	103
Table 26.	Beam theory Closed Form Nondimensional Flexibilities ($bEr^2 = \alpha Er^2$) for Cylindrical Sections ($\theta = 0$) with Varying $(\frac{l}{r})$ and $(\frac{t}{r})$ Ratios.	105
Table 27.	Beam theory Closed Form Nondimensional Flexibilities (βEr^3) for Cylindrical Sections ($\theta = 0$) with Varying $(\frac{l}{r})$ and $(\frac{t}{r})$ Ratios.	106
Table 28.	Beam theory Closed Form Nondimensional Flexibilities (aEr) with ($K_s = .75$) for Cylindrical Sections ($\theta = 0$) with Varying $(\frac{l}{r})$ and $(\frac{t}{r})$ Ratios.	119

	Page
Table 29. Beam theory Closed Form Nondimensional Flexibilities (aEr) for Cylindrical Sections ($\theta = 0$) with Varying ($\frac{t}{r}$) and ($\frac{t}{r}$) Ratios.	120
Table 30. SSME HPOTP Critical Speeds Comparison between the A.S.M. Method and the Shell Element Transfer Matrix Method.	135

LIST OF FIGURES

	Page
Fig. 1. Tip deflections of a cantilevered section	7
Fig. 2. General structure element under shear and bending	8
Fig. 3. Positive and negative angle conical sections with dimensioning	13
Fig. 4. Conical flexibility transformation illustration	15
Fig. 5. "Point"- "Field" shaft sections diagram	17
Fig. 6. Conical section center of mass diagram	19
Fig. 7. Shell element of revolution	22
Fig. 8. ANSYS quadrilateral shell element	25
Fig. 9. Brazier's nonlinear solution compared with St. Venant's linear solution	29
Fig. 10. Brazier's coordinate system for a cylindrical cross section	30
Fig. 11. Brazier flattening (ovalization)	31
Fig. 12. Antonenko mechanization of ovalization	32
Fig. 13. STAGS computer code envelope curve for Brazier flattening	35
Fig. 14. Brazier's experimental plot compared with Brazier's theoretical plot compared with St. Venant's linear plot	38
Fig. 15. Varying conical sections schematic	42
Fig. 16. Cantilevered conical section with tip loading	44
Fig. 17. Flat plate element geometrical constraints	45
Fig. 18. ANSYS mesh with $(\frac{l}{r}) = 1$ and $\theta = 0$	46
Fig. 19. ANSYS mesh with $(\frac{l}{r}) = 1$ and $\theta = 15$	47
Fig. 20. ANSYS mesh with $(\frac{l}{r}) = 1$ and $\theta = 30$	48

	Page
Fig. 21. ANSYS mesh with $(\frac{l}{r}) = 1$ and $\theta = 45$	49
Fig. 22. ANSYS mesh with $(\frac{l}{r}) = 1$ and $\theta = 60$	50
Fig. 23. ANSYS mesh with $(\frac{l}{r}) = 1$ and $\theta = 75$	51
Fig. 24. ANSYS mesh with $(\frac{l}{r}) = .25$ and $\theta = 45$	52
Fig. 25. ANSYS mesh with $(\frac{l}{r}) = .5$ and $\theta = 45$	53
Fig. 26. ANSYS mesh with $(\frac{l}{r}) = 2$ and $\theta = 45$	54
Fig. 27. ANSYS mesh with $(\frac{l}{r}) = 4$ and $\theta = 45$	55
Fig. 28. Nondimensional flexibility plots (aEr) for conical sections with $(\frac{t}{r} = 0.0125)$, varying θ and varying $(\frac{l}{r})$ ratio.	82
Fig. 29. Nondimensional flexibility plots (aEr) for conical sections with $(\frac{t}{r} = 0.025)$, varying θ and varying $(\frac{l}{r})$ ratio.	83
Fig. 30. Nondimensional flexibility plots (aEr) for conical sections with $(\frac{t}{r} = 0.05)$, varying θ and varying $(\frac{l}{r})$ ratio.	84
Fig. 31. Nondimensional flexibility plots (aEr) for conical sections with $(\frac{t}{r} = 0.1)$, varying θ and varying $(\frac{l}{r})$ ratio.	85
Fig. 32. Nondimensional flexibility plots (aEr) for conical sections with $(\frac{t}{r} = 0.2)$, varying θ and varying $(\frac{l}{r})$ ratio.	86
Fig. 33. Nondimensional flexibility plots ($bEr_{-\theta}^2 = \alpha Er_{-\theta}^2$) for conical sections with $(\frac{t}{r} = 0.0125)$, varying θ and varying $(\frac{l}{r})$ ratio.	87
Fig. 34. Nondimensional flexibility plots ($bEr_{-\theta}^2 = \alpha Er_{-\theta}^2$) for conical sections with $(\frac{t}{r} = 0.025)$, varying θ and varying $(\frac{l}{r})$ ratio.	88
Fig. 35. Nondimensional flexibility plots ($bEr_{-\theta}^2 = \alpha Er_{-\theta}^2$) for conical sections with $(\frac{t}{r} = 0.05)$, varying θ and varying $(\frac{l}{r})$ ratio.	89

Fig. 36.	Nondimensional flexibility plots ($bEr_{+\theta}^2 = \alpha Er_{-\theta}^2$) for conical sections with ($\frac{t}{r} = 0.1$), varying θ and varying ($\frac{l}{r}$) ratio.	90
Fig. 37.	Nondimensional flexibility plots ($bEr_{-\theta}^2 = \alpha Er_{-\theta}^2$) for conical sections with ($\frac{t}{r} = 0.2$), varying θ and varying ($\frac{l}{r}$) ratio.	91
Fig. 38.	Nondimensional flexibility plots ($\alpha Er_{-\theta}^2 = bEr_{-\theta}^2$) for conical sections with ($\frac{t}{r} = 0.0125$), varying θ and varying ($\frac{l}{r}$) ratio.	92
Fig. 39.	Nondimensional flexibility plots ($\alpha Er_{+\theta}^2 = bEr_{-\theta}^2$) for conical sections with ($\frac{t}{r} = 0.025$), varying θ and varying ($\frac{l}{r}$) ratio.	93
Fig. 40.	Nondimensional flexibility plots ($\alpha Er_{+\theta}^2 = bEr_{-\theta}^2$) for conical sections with ($\frac{t}{r} = 0.05$), varying θ and varying ($\frac{l}{r}$) ratio.	94
Fig. 41.	Nondimensional flexibility plots ($\alpha Er_{-\theta}^2 = bEr_{-\theta}^2$) for conical sections with ($\frac{t}{r} = 0.1$), varying θ and varying ($\frac{l}{r}$) ratio.	95
Fig. 42.	Nondimensional flexibility plots ($\alpha Er_{+\theta}^2 = bEr_{-\theta}^2$) for conical sections with ($\frac{t}{r} = 0.2$), varying θ and varying ($\frac{l}{r}$) ratio.	96
Fig. 43.	Nondimensional flexibility plots (βEr^3) for conical sections with ($\frac{t}{r} = 0.0125$), varying θ and varying ($\frac{l}{r}$) ratio.	97
Fig. 44.	Nondimensional flexibility plots (βEr^3) for conical sections with ($\frac{t}{r} = 0.025$), varying θ and varying ($\frac{l}{r}$) ratio.	98

Fig. 45.	Nondimensional flexibility plots (βEr^3) for conical sections with ($\frac{t}{r} = 0.05$), varying θ and varying ($\frac{l}{r}$) ratio.	99
Fig. 46.	Nondimensional flexibility plots (βEr^3) for conical sections with ($\frac{t}{r} = 0.1$), varying θ and varying ($\frac{l}{r}$) ratio.	100
Fig. 47.	Nondimensional flexibility plots (βEr^3) for conical sections with ($\frac{t}{r} = 0.2$), varying θ and varying ($\frac{l}{r}$) ratio.	101
Fig. 48.	Beam theory closed form nondimensional flexibility plots compared to finite element nondimensional flexibility plots ($bEr^2 = \alpha Er^2$) for cylindrical sections ($\theta = 0$) with varying ($\frac{l}{r}$) ratio and ($\frac{t}{r} = .0125$.)	107
Fig. 49.	Beam theory closed form nondimensional flexibility plots compared to finite element nondimensional flexibility plots ($bEr^2 = \alpha Er^2$) for cylindrical sections ($\theta = 0$) with varying ($\frac{l}{r}$) ratio and ($\frac{t}{r} = .025$.)	108
Fig. 50.	Beam theory closed form nondimensional flexibility plots compared to finite element nondimensional flexibility plots ($bEr^2 = \alpha Er^2$) for cylindrical sections ($\theta = 0$) with varying ($\frac{l}{r}$) ratio and ($\frac{t}{r} = .05$.)	109
Fig. 51.	Beam theory closed form nondimensional flexibility plots to finite element nondimensional flexibility plots ($bEr^2 = \alpha Er^2$) for cylindrical sections ($\theta = 0$) with varying ($\frac{l}{r}$) ratio and ($\frac{t}{r} = .1$.)	110

- Fig. 52. Beam theory closed form nondimensional flexibility plots
to finite element nondimensional flexibility plots
($bEr^2 = \alpha Er^2$) for cylindrical sections ($\theta = 0$) with
varying ($\frac{l}{r}$) ratio and ($\frac{t}{r} = .2$.) 111
- Fig. 53. Beam theory closed form nondimensional flexibility plots
to finite element nondimensional flexibility plots
($3Er^3$) for cylindrical sections ($\theta = 0$) with
varying ($\frac{l}{r}$) ratio and ($\frac{t}{r} = .0125$.) 112
- Fig. 54. Beam theory closed form nondimensional flexibility plots
to finite element nondimensional flexibility plots
($3Er^3$) for cylindrical sections ($\theta = 0$) with
varying ($\frac{l}{r}$) ratio and ($\frac{t}{r} = .025$.) 113
- Fig. 55. Beam theory closed form nondimensional flexibility plots
to finite element nondimensional flexibility plots
($3Er^3$) for cylindrical sections ($\theta = 0$) with
varying ($\frac{l}{r}$) ratio and ($\frac{t}{r} = .05$.) 114
- Fig. 56. Beam theory closed form nondimensional flexibility plots
to finite element nondimensional flexibility plots
($3Er^3$) for cylindrical sections ($\theta = 0$) with
varying ($\frac{l}{r}$) ratio and ($\frac{t}{r} = .1$.) 115
- Fig. 57. Beam theory closed form nondimensional flexibility plots
to finite element nondimensional flexibility plots
($3Er^3$) for cylindrical sections ($\theta = 0$) with
varying ($\frac{l}{r}$) ratio and ($\frac{t}{r} = .2$.) 116

Fig. 58.	Beam theory closed form nondimensional flexibility plots to finite element nondimensional flexibility plots (aEr) for cylindrical sections ($\theta = 0$) with varying ($\frac{l}{r}$) ratio and ($\frac{t}{r} = .0125$.)	121
Fig. 59.	Beam theory closed form nondimensional flexibility plots to finite element nondimensional flexibility plots (aEr) for cylindrical sections ($\theta = 0$) with varying ($\frac{l}{r}$) ratio and ($\frac{t}{r} = .025$.)	122
Fig. 60.	Beam theory closed form nondimensional flexibility plots to finite element nondimensional flexibility plots (aEr) for cylindrical sections ($\theta = 0$) with varying ($\frac{l}{r}$) ratio and ($\frac{t}{r} = .05$.)	123
Fig. 61.	Beam theory closed form nondimensional flexibility plots to finite element nondimensional flexibility plots (aEr) for cylindrical sections ($\theta = 0$) with varying ($\frac{l}{r}$) ratio and ($\frac{t}{r} = .1$.)	124
Fig. 62.	Beam theory closed form nondimensional flexibility plots to finite element nondimensional flexibility plots (aEr) for cylindrical sections ($\theta = 0$) with varying ($\frac{l}{r}$) ratio and ($\frac{t}{r} = .2$.)	125
Fig. 63.	60° cone test piece with dimensioning	128
Fig. 64.	Three stepped beam model of the 60° cone test piece	129
Fig. 65.	Cone test piece fundamental mode shape	130
Fig. 66.	Space Shuttle Main Engine High Pressure Oxidizer Turbopump Assembly (SSME HPOTP)	132

	Page
Fig. 67. Campbell diagram for the A.S.M. method	133
Fig. 68. Campbell diagram for the shell element transfer matrix method	134
Fig. 69. SSME HPOTP 9000 rpm mode shape	136
Fig. 70. Cone with negative attitude loading for the transformation identities development	149

NOMENCLATURE

a	= flexibility coefficient relating Y_i displacement to shear loading (V_i)
a_n	= (a) flexibility coefficient for a negative cone angle, $(-\theta)$
a_p	= (a) flexibility coefficient for a positive cone angle, θ
A	= point on the Brazier flattening curve representing maximum bending moment at buckling
A_c	= cross sectional area
b	= flexibility coefficient relating Y_i displacement to moment loading (M_{i-1})
b_n	= (b) flexibility coefficient for a negative cone angle, $-\theta$
b_p	= (b) flexibility coefficient for a positive cone angle, θ
c	= measurement of the severity of curvature of the structure bending axis under load
C_e	= finite element width in the circumferential direction
C_f	= compressive force
C_M	= conical section center of mass
$d(Vol)$	= differential element of volume
$D.E.$	= structure differential element
e_x	= in-plane strain in the x direction of the element plane defined by the x normal
e_y	= in-plane strain in the y direction of the element plane defined by the y normal
e_{xy}	= in-plane strain in the x or y direction of the element plane defined by the y or x normal respectively
e_{xz}	= transverse strain in the z direction of the element plane defined by the x normal

- e_{yz} = transverse strain in the z direction of the element plane defined by the y normal
 e_{zz} = transverse strain in the z direction of the element plane defined by the z normal
 E = Young's modulus of elasticity
 $f_{\theta y}$ = flexibility of the structure for the rotational deflection under shear loading
 $f_{\theta\theta}$ = flexibility of the structure for the rotational deflection under bending moment loading
 $f_{y\theta}$ = flexibility of the structure for the radial deflection under bending moment loading
 f_{yy} = flexibility of the structure for the radial deflection under shear loading
 G = shear modulus of elasticity
 I = cross sectional area moment of inertia
 I_D = diametral moment of inertia
 $(I_D)_1$ = lumped diametral moment of inertia at the small radius cone end
 $(I_D)_2$ = lumped diametral moment of inertia at the large radius cone end
 I_p = polar moment of inertia
 $(I_p)_1$ = lumped polar moment of inertia at the small radius cone end
 $(I_p)_2$ = lumped polar moment of inertia at the large radius cone end
 K = linear spring constant in the point matrix
 K_s = shear form factor
 $K_{\theta,-1}$ = torsional spring constant in the point matrix
 l = length of structure element

l_c	= finite element length in the axial direction
m	= mass of the point station
M	= mass of the hollow conical section
\overline{M}	= maximum bending moment for the structure prior to failure
M_1	= lumped mass at small radius cone end
M_b	= pure bending moment applied to the structure's rigid ends
M_{cr}	= critical bending moment at which buckling begins
M_i	= pure bending moment at structure right end
M_{i-1}	= pure bending moment at structure left end
M_{in}	= mass of the conical section based on a solid cross section with inner radius
M_o	= mass of the conical section based on a solid cross section with outer radius
M_z	= pure bending moment about z axis
N_{θ_s}	= normal force on the shell element of revolution in the θ_s direction
N_{θ_s, ϕ_s}	= shear force on the shell element of revolution in the ϕ_s direction
N_{ϕ_s}	= normal force on the shell element of revolution in the ϕ_s direction
N_{ϕ_s, θ_s}	= shear force on the shell element of revolution in the θ_s direction
r	= cylindrical or conical section small end radius measured from structure centerline axis to midwall thickness
r_1	= circular radius of curvature for the differential angle, $d\phi_s$, of the shell element of revolution
r_2	= circular radius of curvature of the angle, ϕ_s , of the shell element of revolution.
r_3	= circular radius of curvature of the angle, ϕ_s , of the shell

element of revolution.

- r_c = radius of curvature of the structure bending axis under load
- r_i = cylindrical or conical section small end inside radius measured from structure centerline axis to inside wall
- r_o = cylindrical or conical section small end outside radius measured from structure centerline axis to outside wall
- $(R_1)_{in}$ = inner radius of the conical section small end
- $(R_1)_o$ = outer radius of the conical section small end
- $(R_2)_{in}$ = inner radius of the conical section large end
- $(R_2)_o$ = outer radius of the conical section large end
- $(R_{CM})_{in}$ = inner radius at the cone section center of mass
- $(R_{CM})_o$ = outer radius at the cone section center of mass
- t = conical or cylindrical section uniform wall thickness
- T_f = tension force
- u = displacement in the x direction
- v = displacement in the y direction
- V_i = shear load at structure right end
- V_{i-1} = shear load at structure left end
- Vol = volume
- Y_i = structure element right end radial displacement under load
- Y_{i-1} = structure element left end radial displacement under load
- Y_m = structure right end radial displacement under a unit moment load and zero shear load
- Y_v = structure right end radial displacement under a unit shear load and zero moment load

Z	= normal force on the shell element in the z direction
α	= flexibility coefficient relating θ_i displacement to shear loading (V_{i-1})
α_n	= (α) flexibility coefficient for a negative cone angle, $-\theta$
α_p	= (α) flexibility coefficient for a positive cone angle, θ
β	= flexibility coefficient relating θ_i displacement to moment loading (M_{i-1})
β_n	= (β) flexibility coefficient for a negative cone angle, $-\theta$
β_p	= (β) flexibility coefficient for a positive cone angle, θ
$\{\delta e\}^T$	= transpose of the strain vector
δU	= virtual strain energy
δV	= virtual work
Δw	= change in structure midlength diameter in direction of loading
θ	= conical section cone angle
θ_c	= finite element arc angle
θ_i	= structure element right end rotational displacement under load
θ_{i-1}	= structure element left end rotational displacement under load
θ_m	= structure right end rotational displacement under a unit moment load and zero shear load
θ_s	= shell element of revolution rotation about the element z axis
θ_v	= structure right end rotational displacement under a unit shear load and zero moment load
ν	= Poisson's ratio
π	= ratio of the circumference of a circle divided by the diameter
ρ	= mass density of the structure material

- σ = stress at a point in the shell
- $\{\sigma\}$ = stress vector associated with the strain vector by the constitutive equations
- ϕ = $\theta_i + \theta_{i-1}$, the angle associated with the radius of curvature of the structure bending axis under load
- ϕ_s = shell element of revolution rotation about the element x axis
- ψ = angular coordinate location for the Brazier coordinate system
- ω = structure natural frequency
- ∞ = infinity

1. INTRODUCTION

In the turbomachinery industry, the emphasis is to develop more and more efficient engines with higher reliability at a minimum cost. In the long run, the bulk of the cost is encountered when there are compromises on reliability and thus maintainability of the engine. Millions and eventually billions of dollars can be saved by increasing reliability and decreasing maintenance down time required for the advanced turbomachine. The primary cause for decreased reliability and high maintenance costs of the engine is vibration during operation. The study of how to control and minimize the vibration loading input to the various members of the engine assembly is by no means simple

An ideal method of solving these vibration problems is to be able to analytically predict the vibrations during the design and development phase of the engine. One tool used by Rotordynamicists today is the transfer matrix method. The method developed by Mykelstad (1944), Prohl (1945), Koenig (1961), Sevcik (1963), Lund et al., (1967), Hibner (1975), and Various other authors is maintaining its popularity due to its relative ease in use and fast computer solution time.

This work is mainly concerned with improving the accuracy and range of application of the transfer matrix method used in rotordynamics analysis. Current day rotordynamics transfer matrix programs are based on modelling the rotor sections with closed form beam theory solutions. However, many advanced engines today such as used in aircraft applications have thin walled conical section

This thesis follows the style of the *ASME Journal of Vibration, Acoustics, Stress, and Reliability in Design*.

rotors which cannot be modeled as beam sections. In addition, the whole engine must be modeled including the housings and casings which also do not deform according to beam theory.

There have been recent publications proposing various methods for solving this problem of inaccuracy due to the beam modelling used in the transfer matrix approach. Rouch et al., (1979), Nelson (1980), To (1981), Greenhill et al., (1985), and Gupta (1986) have all worked on developing new finite elements for the finite element method as an alternative to the transfer matrix method. In the pursuit of increased accuracy, many major turbomachinery engine manufacturers have generated highly complex and very expensive finite element modelling of complete engine structures. Becker et al., (1988) has published one such general finite element method for rotordynamics analysis. However more accurate the analysis may become, there is a high dollar cost for the engineering and computer time involved in the finite element modelling of today's advanced turbomachinery such as the light weight high performance jet aircraft engines.

Shell finite element analysis was used to generate the design data presented in this work. The design data can now be used in the transfer matrix method by design engineers and analysts without having to do any shell finite element modeling. Not only will this result in engineering and computer cost savings but it will also free up engineers and analysts to work on other problems in turbomachinery which need to be solved. Beamish et al., (1988) has presented a paper on this approach, however, using the finite element frequency method of determining the design data. The finite element frequency method was also published by Beamish et al., (1986). Thompson et al., (1988) modeled the complete LM2500 U.S. Navy gas turbine engine using the transfer matrix method

with finite element conical section flexibilities. Although the conical section flexibilities were determined for only the specific LM2500 gas turbine engine, his demonstration serves as an excellent validation of the shell finite element transfer matrix approach presented in this work.

The design data are developed herein by modeling conical sections of industry specifications using shell finite elements. The flexibility coefficients for the complete range of structural geometries encountered within industry have been generated. These values are tabulated and plotted in nondimensional form for ease in application by turbomachinery design engineers and analysts. The method of replacing the old inaccurate beam flexibility coefficients with the shell generated flexibility coefficients adds no complexity to the current transfer matrix analysis. Rather, it actually decreases computer solution time by decreasing the number of stations in the analysis and can greatly increase accuracy of critical speed predictions, especially in rotors with thin conical sections.

In this work, axisymmetric cantilevered shells with nonaxisymmetric loads were modeled. The left end of the structure was held fixed and the right end cantilevered. The right end was then tip loaded first by a unit moment load and second by a unit shear load. The tip radial and rotational displacements were measured for the two separate load cases in turn. By using the force, displacement and flexibility mathematics relations, the needed flexibilities and thus nondimensional flexibility coefficients were obtained.

From the beginning of this work, the effects of cross section ovalization of the hollow structures under load were raised as a potential problem. The effects on the linearity of the flexibility coefficients was found negligible for the loading expected in turbomachinery applications. A literature survey on the theory of

this ovalization was conducted and is presented including actual quantification of these effects.

2. THEORETICAL BACKGROUND

In order to demonstrate the improvement of using shell elements in the transfer matrix method, a review of the current method is presented. The special considerations of using shell elements is also presented. The field transfer matrix for a general elastic structure is developed. The special case of the Timoshenko beam element using advanced strength of materials (A.S.M.) for the field transfer matrix is also presented. The flexibilities of both the general structure element and specific case beam element are developed. Convergence of flexibility values as the general structure approaches a beam structure is discussed. The flexibility transformations of a general structure loaded at opposite ends in turn is developed.

The point transfer matrix for the conical shell structure cannot be modeled by conventional lumping at the ends of discrete beam sections. *Large errors for the lumped masses, polar and diametral moments of inertia will result when the structure is modeled in this manner.* The lumped masses, polar and diametral moments of inertia are shown as developed in Beamish et al., (1988).

The nonaxisymmetric partial differential equations for shells of revolution are presented and discussed. The finite element method of solution was chosen because of its ease in this application. The shell finite elements are discussed along with the method of solution.

2.1 Field Transfer Matrix Development

The field transfer matrix can be developed for an elastic structure of any geometry provided the proper boundary conditions are applied. The energy and displacement principles of both Betti's Reciprocal Theorem and Maxwell's Reciprocal Theorem (Tuma, 1969) and the theory of advanced strength of materials have been applied in the development of the transfer matrices contained herein. Both ends of the general elastic structure have been constrained to remain rigid. These are essential boundary conditions in order that the theory of transfer matrices can accurately model the strain energy state and deflections of the structure under load. The deflections were measured as shown in Fig. 1. The general form of the transfer matrix which governs the relation between the state of the structure at the left end, $(i - 1)$, and at the right end, (i) , is;

$$\begin{Bmatrix} Y_i \\ \theta_i \\ M_i \\ V_i \end{Bmatrix} = \begin{bmatrix} 1 & l & b & a \\ 0 & 1 & \beta & \alpha \\ 0 & 0 & 1 & l \\ 0 & 0 & 0 & 1 \end{bmatrix} \begin{Bmatrix} Y_{i-1} \\ \theta_{i-1} \\ M_{i-1} \\ V_{i-1} \end{Bmatrix} \quad (1)$$

The state variables of radial displacement, angular displacement, moment loading and shear loading are illustrated in Fig. 2. (For the derivation of equation (1), see APPENDIX A.)

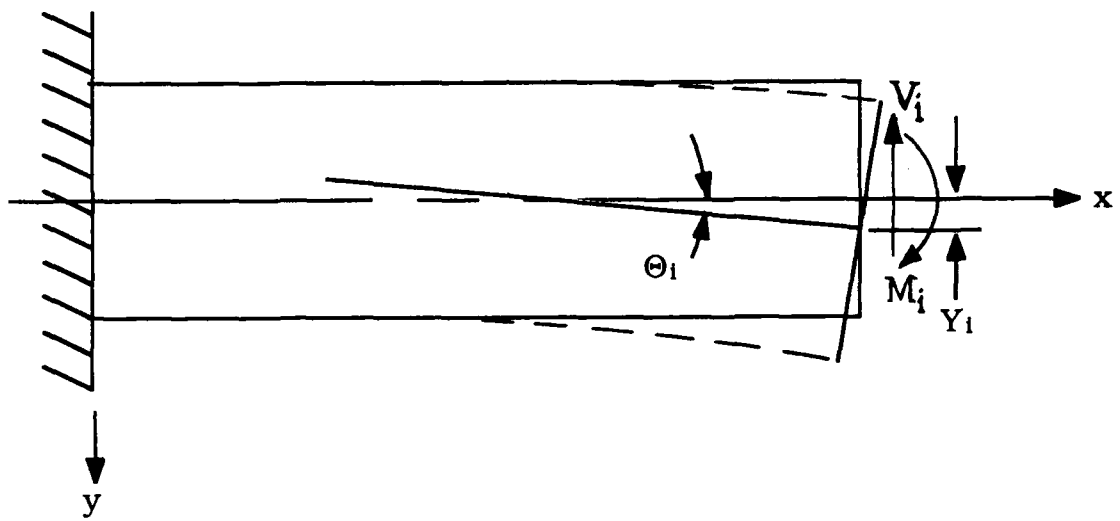


Fig. 1. Tip deflections of a cantilevered section.

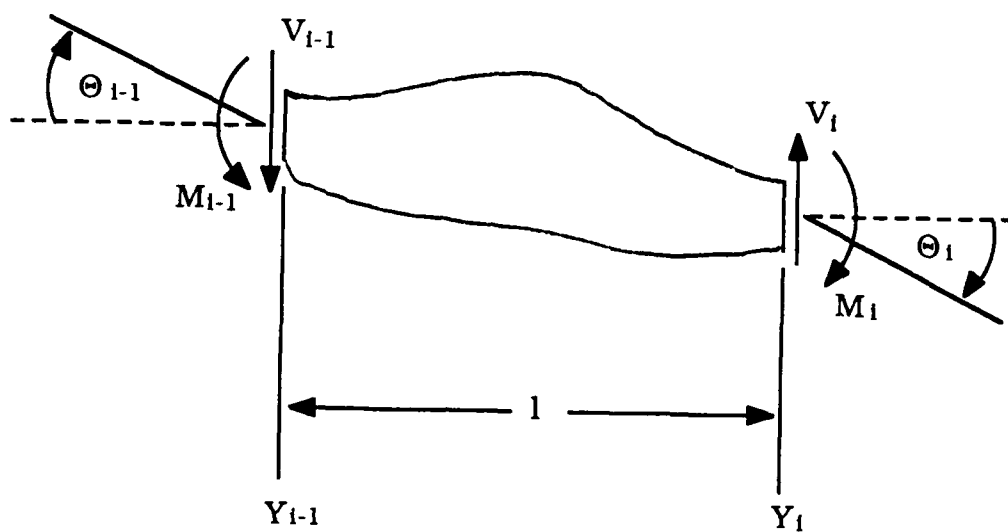


Fig. 2. General structure element under shear and bending.

2.1.1 General Structure Element

It is shown in APPENDIX A for a general structure element that the state variables at the right end can be related to those at the left by the flexibilities of the element. This can be stated in the form of the transfer matrix of equation (2)

$$\begin{Bmatrix} Y_i \\ \theta_i \\ M_i \\ V_i \end{Bmatrix} = \begin{bmatrix} 1 & l & f_{y\theta} & l(f_{y\theta}) - f_{yy} \\ 0 & 1 & f_{\theta\theta} & l(f_{\theta\theta}) - f_{\theta y} \\ 0 & 0 & 1 & l \\ 0 & 0 & 0 & 1 \end{bmatrix} \begin{Bmatrix} Y_{i-1} \\ \theta_{i-1} \\ M_{i-1} \\ V_{i-1} \end{Bmatrix} \quad (2)$$

It is important at this point to note from equation (2) how the general flexibility coefficients, a , b , α , and β , of conical structures can be obtained. The flexibilities of the structure $f_{y\theta}$, f_{yy} , $f_{\theta\theta}$, and $f_{\theta y}$, shown in equation (2), can be obtained by inverting the stiffness matrix of the structure. Thus the problem of generating the previously unknown conical shell structure transfer matrix flexibility coefficients is reduced to obtaining the inverse of the stiffness matrix of the structure. This has been achieved by the tip loading method explained in the Introduction. (For the derivation of equation (2), see APPENDIX A.)

2.1.2 Timoshenko Beam Element

It can be shown for a Timoshenko beam element that the state variables at the right end can be related to those at the left by the use of closed form expressions. This relation can be stated in the form of the transfer matrix of equation (3).

$$\begin{Bmatrix} Y_i \\ \theta_i \\ M_i \\ V_i \end{Bmatrix} = \begin{bmatrix} 1 & l & \frac{l^2}{2EI} & \frac{l^3}{6EI} - \frac{l}{GA_c K_s} \\ 0 & 1 & \frac{l}{EI} & \frac{l^2}{2EI} \\ 0 & 0 & 1 & l \\ 0 & 0 & 0 & 1 \end{bmatrix} \begin{Bmatrix} Y_{i-1} \\ \theta_{i-1} \\ M_{i-1} \\ V_{i-1} \end{Bmatrix} \quad (3)$$

This closed formed transfer matrix is developed using advanced strength of materials. (For the derivation of equation (3), see APPENDIX A.) Current day transfer matrix computational programs are based on different forms of equation (3). Some neglect the shear term ($\frac{l}{GA_c K_s}$) and others who include the term often use a generalized constant shear form factor, $K_s = 0.75$. Both of these current practices can severely limit the applicability of transfer matrix analysis to the wide spectrum of rotor modeling discussed in the Introduction. The errors are quantified in section 5.4.

2.1.3 Cantilevered Shaft Flexibilities

In order to determine the conical shell flexibilities a , b , α , and β , it is first advantageous to reduce these to expressions based on the tip deflections of the cantilevered conical section under unit tip loading. These are;

$$a = l(Y_m) + Y_v \quad (4)$$

$$b = Y_m \quad (5)$$

$$\alpha = l(\theta_m) + \theta_v \quad (6)$$

$$\beta = \theta_m \quad (7)$$

(These equations are developed in APPENDIX B.)

2.1.4 Cantilevered Beam Flexibilities

The flexibility coefficients a , b , α , and β for a Timoshenko beam element including shear from advanced strength of materials can be obtained using the methods of section 2.1.3. (This is also shown in APPENDIX B.) The closed form expressions are;

$$a = \frac{l^3}{6EI} - \frac{l}{GA_cK_s} \quad (8)$$

$$b = \alpha = \frac{l^2}{2EI} \quad (9)$$

$$\beta = \frac{l}{EI} \quad (10)$$

2.1.5 Shaft-Beam Convergence

The theory used in the development of equations (4), (5), (6) and (7) has no basic assumptions limiting the geometry of the structure. Thus it should follow that as the geometry of the structure approaches that of a Timoshenko

beam element, the corresponding flexibility coefficients a , b , α , and β should converge upon the closed form expressions of equations (8), (9) and (10). This is demonstrated and discussed in the numerical results and discussion of section 5.

2.1.6 Conical Flexibility Transformation

By applying the principles of both Betti's Reciprocal Theorem of energy and Maxwell's Reciprocal Theorem of displacements (Tuma, 1969) with transfer matrix mathematics, a very simple transformation is developed relating the conical shell flexibility coefficients of a positive angle cone to the same geometry but of a negative angle. (See Fig. 3.) The equations are;

$$a_n = a_p \quad (11)$$

$$b_n = \alpha_p \quad (12)$$

$$\alpha_n = b_p \quad (13)$$

$$\beta_n = \beta_p \quad (14)$$

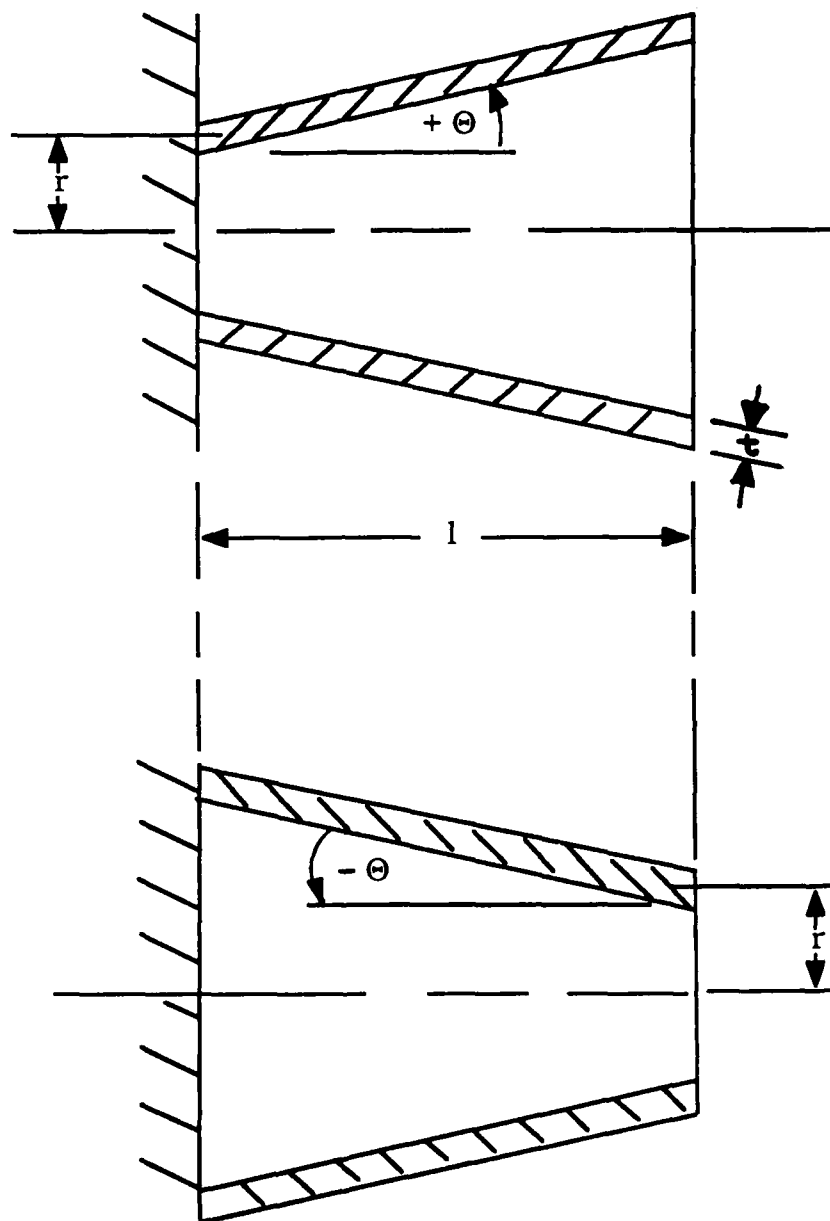
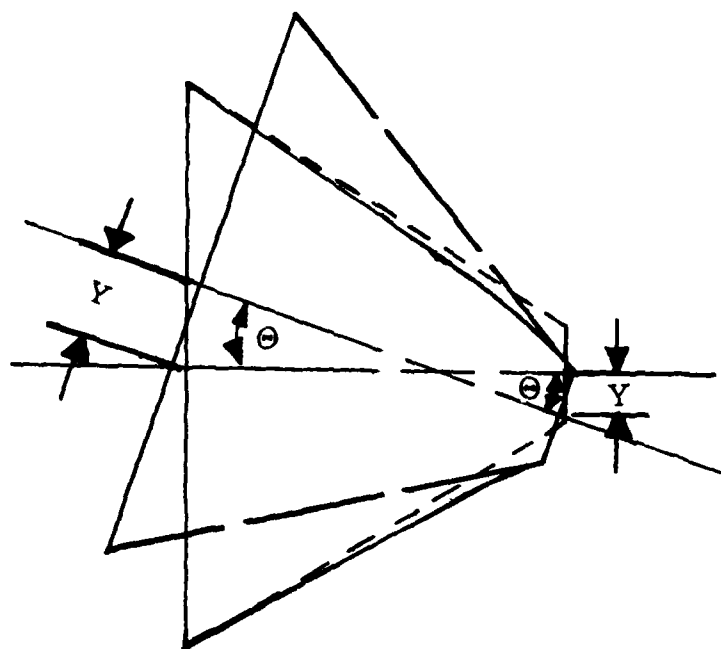


Fig. 3. Positive and negative angle conical sections with dimensioning.

(See APPENDIX C for the derivation of equations (11) through (14).) For the conical flexibility transformation illustration of Fig. 4, both the large left end and small right end are constrained to remain rigid. The solid line walls represent the deformed structure under load, either shear or bending or combined. By first considering the undeformed negative angle structure, fixing the left end, and loading the right end (positive attitude loading), the deformed structure of the solid line results. Conversely, by fixing the right end of the positive angle structure and loading the left end (negative attitude loading), the identical deformed structure of the solid line results. This is due to the rigid end constraints. It is important to note that the deformed structures of each attitude loading have identical stress and strain energy states. The tip deflections are measured as previously defined in Fig. 1. The equivalent rotational displacements are easily seen. The radial displacement transformations are developed in APPENDIX C.



- Loaded structure
for both positive
and negative attitude
- Unloaded structure,
negative attitude, (small end fixed).
- Unloaded structure,
positive attitude, (large end fixed).

Fig. 4. Conical flexibility transformation illustration.

2.2 Point Transfer Matrix for Conical Sections.

The point transfer matrix represents the lumped masses, polar moments of inertia and diametral moments of inertia of the rotor shaft or casing sections lumped at the "point" between any two sections (or stations) of the complete rotor-bearing system. Other dynamic effects of the complete system are assembled into the point transfer matrix but are not discussed here because of their independence of the shaft modeling. These other dynamic contributions, for example, are bearings, seals, supports and foundations. (See Fig.5 for an illustration of the "point" transfer section.) In order to describe the terms in the "point" transfer matrix, consider the simplified special case of forward circular synchronous whirl due to unbalance response;

$$\begin{Bmatrix} Y_i \\ \theta_i \\ M_i \\ V_i \end{Bmatrix} = \begin{bmatrix} 1 & 0 & 0 & 0 \\ 0 & 1 & 0 & 0 \\ 0 & \omega^2(I_{D,i-1} - I_{P,i-1}) - K_\theta & 1 & 0 \\ (K_{i-1} - M_{i-1}\omega^2) & 0 & 0 & 1 \end{bmatrix} \begin{Bmatrix} Y_{i-1} \\ \theta_{i-1} \\ M_{i-1} \\ V_{i-1} \end{Bmatrix} \quad (15)$$

When modeling a conical section as a shell rather than a series of stepped beams, the lumped masses, polar moments of inertia and diametral moments of inertia cannot be evenly divided between the two points on either end of the conical shaft section. Dividing evenly is the correct method for cylindrical sections, but large errors up to changes in order of magnitude will result if this is attempted for conical sections, especially for large cone angle sections. Beamish et al., (1988), by taking the geometrical properties into account, has developed closed form expressions for the lumped masses, polar moments of inertia and diametral moments of inertia for conical sections.

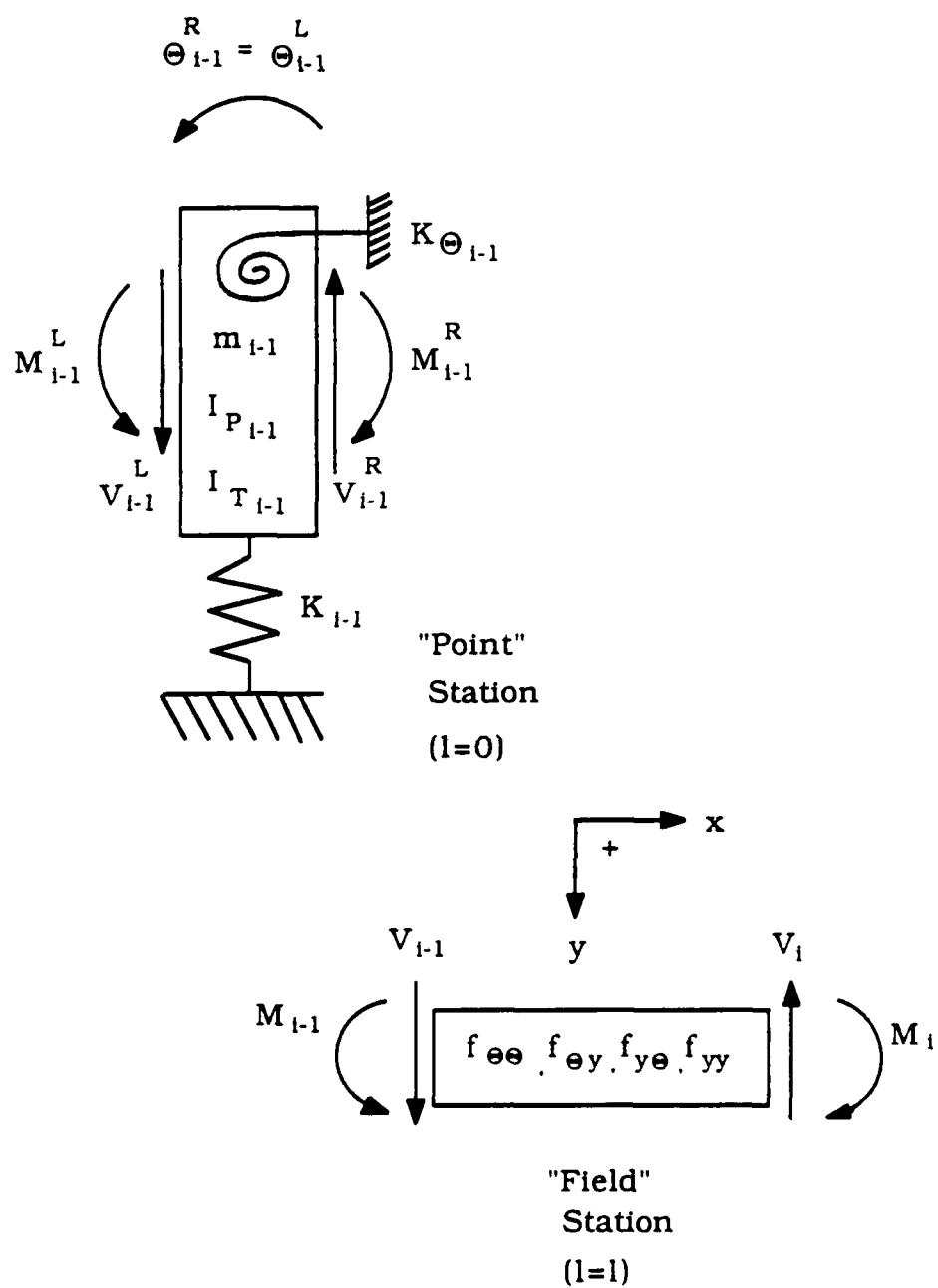


Fig. 5. "Point"- "Field" shaft sections diagram.

2.2.1 Lumped Masses and Polar Moments of Inertia

Referring to Fig. 6, according to Beamish et al., (1988), the lumped mass at the small radius cone end is

$$M_1 = (1 - \frac{C_M}{l})M \quad (16)$$

and the lumped mass at the large radius cone end is

$$M_2 = (\frac{C_M}{l})M \quad (17)$$

where the mass of the entire conical section is

$$\begin{aligned} M &= \frac{\rho\pi l}{3}(M_o - M_{in}) \\ &= \frac{\rho\pi l}{3} [(R_1^2 + R_1 R_2 + R_2^2)_o - (R_1^2 + R_1 R_2 + R_2^2)_{in}] \end{aligned} \quad (18)$$

and the cone center of mass is

$$C_M = \frac{(R_{C_{M_o}})M_o - (R_{C_{M_{in}}})M_{in}}{M_o - M_{in}} \quad (19)$$

The outside radius is

$$R_{C_{M_o}} = \frac{l}{4} \left[\frac{(R_1^2 + 2R_1 R_2 + 3R_2^2)}{(R_1^2 + R_1 R_2 + R_2^2)} \right]_o \quad (20)$$

and the inside radius is

$$R_{C_{M_{in}}} = \frac{l}{4} \left[\frac{(R_1^2 + 2R_1 R_2 + 3R_2^2)}{(R_1^2 + R_1 R_2 + R_2^2)} \right]_{in} \quad (21)$$

The lumped polar moment of inertia at the small radius cone end is

$$(I_p)_1 = (1 - \frac{C_M}{l})I_p \quad (22)$$

and the lumped polar moment of inertia at the large radius cone end is

$$(I_p)_2 = (\frac{C_M}{l})I_p \quad (23)$$

where the polar moment of inertia for the entire conical section is

$$\begin{aligned} I_p &= \frac{\rho\pi l}{10} [(R_1^4 + R_1^3 R_2 + R_1^2 R_2^2 + R_1 R_2^3 + R_2^4)_o \\ &\quad - (R_1^4 + R_1^3 R_2 + R_1^2 R_2^2 + R_1 R_2^3 + R_2^4)_{in}] \end{aligned} \quad (24)$$

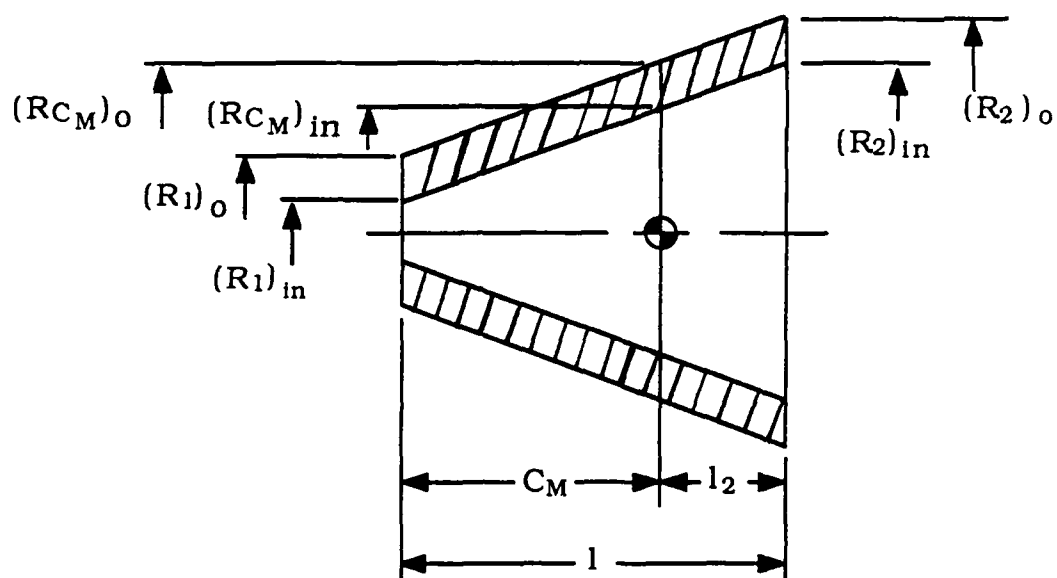


Fig. 6. Conical section center of mass diagram.

2.2.2 Lumped Diametral Moments of Inertia

Referring to Fig.6 and section 2.2.1, the diametral moment of inertia for the entire cone is given by

$$I_D = \rho\pi \left\{ \left[\frac{l}{20}(R_1^4 + R_1^3 R_2 + R_1^2 R_2^2 + R_1 R_2^3 + R_2^4) + l^3 \left(\frac{R_1^2}{30} + \frac{R_1 R_2}{10} + \frac{R_2^2}{5} \right) \right]_o - \left[\frac{l}{20}(R_1^4 + R_1^3 R_2 + R_1^2 R_2^2 + R_1 R_2^3 + R_2^4) + l^3 \left(\frac{R_1^2}{30} + \frac{R_1 R_2}{10} + \frac{R_2^2}{5} \right) \right]_{in} \right\} \quad (25)$$

and the lumped diametral moment of inertia at the small radius cone end is solved for by the substitution

$$(I_D)_1 = I_D \quad \text{with} \quad \begin{cases} l = l_1 = C_M \\ (R_2)_o = (R_{C_M})_o \\ (R_2)_{in} = (R_{C_M})_{in} \end{cases} \quad (26)$$

and the lumped diametral moment of inertia at the large radius cone end is solved for by substitution

$$(I_D)_2 = I_D \quad \text{with} \quad \begin{cases} l = l_2 \\ (R_1)_o = (R_{C_M})_o \\ (R_1)_{in} = (R_{C_M})_{in} \end{cases} \quad (27)$$

The outer and inner radii at the cone section center of mass are

$$\begin{aligned} (R_{C_M})_o &= (R_1)_o + \left(\frac{C_M}{l} \right) (R_2 - R_1)_o \\ (R_{C_M})_{in} &= (R_1)_{in} + \left(\frac{C_M}{l} \right) (R_2 - R_1)_{in} \end{aligned} \quad (28)$$

2.3 Shell Theory

The analysis of uniform shells of revolution under edge loading is by no means a trivial problem. The loading is nonaxisymmetric, thus resulting in a nonaxisymmetric distribution of stresses and strains throughout the shell. The solution to the nonaxisymmetric partial differential equations for the cylinder (simplified special case of cone with cone angle $\theta = 0$, see Fig. 3.) is also nontrivial. An exhaustive literature search was conducted resulting in no closed form solution found for either conical or cylindrical shells of revolution.

2.3.1 Shells of Revolution

As stated in Timoshenko et al., (1959), the governing equations for shells of revolution are

$$\frac{N_{\phi_s}}{r_1} + \frac{N_{\theta_s}}{r_2} = -Z \quad (29)$$

with the nonaxisymmetric partial differential equations

$$\frac{\partial}{\partial \phi_s}(N_{\phi_s} r_3) + \frac{\partial N_{\theta_s, \phi_s}}{\partial \theta_s} r_1 - N_{\theta_s, r_1} \cos \phi_s + Y r_1 r_3 = 0 \quad (30)$$

and

$$\frac{\partial}{\partial \phi_s}(r_3 N_{\phi_s, \theta_s}) + \frac{\partial N_{\theta_s}}{\partial \theta_s} r_1 + N_{\theta_s, \phi_s} r_1 \cos \phi_s + X r_3 r_1 = 0 \quad (31)$$

(See Fig. 7 for an illustration of these normal and shearing forces.) It is important to note that the solution of these equations will yield the membrane stresses only.

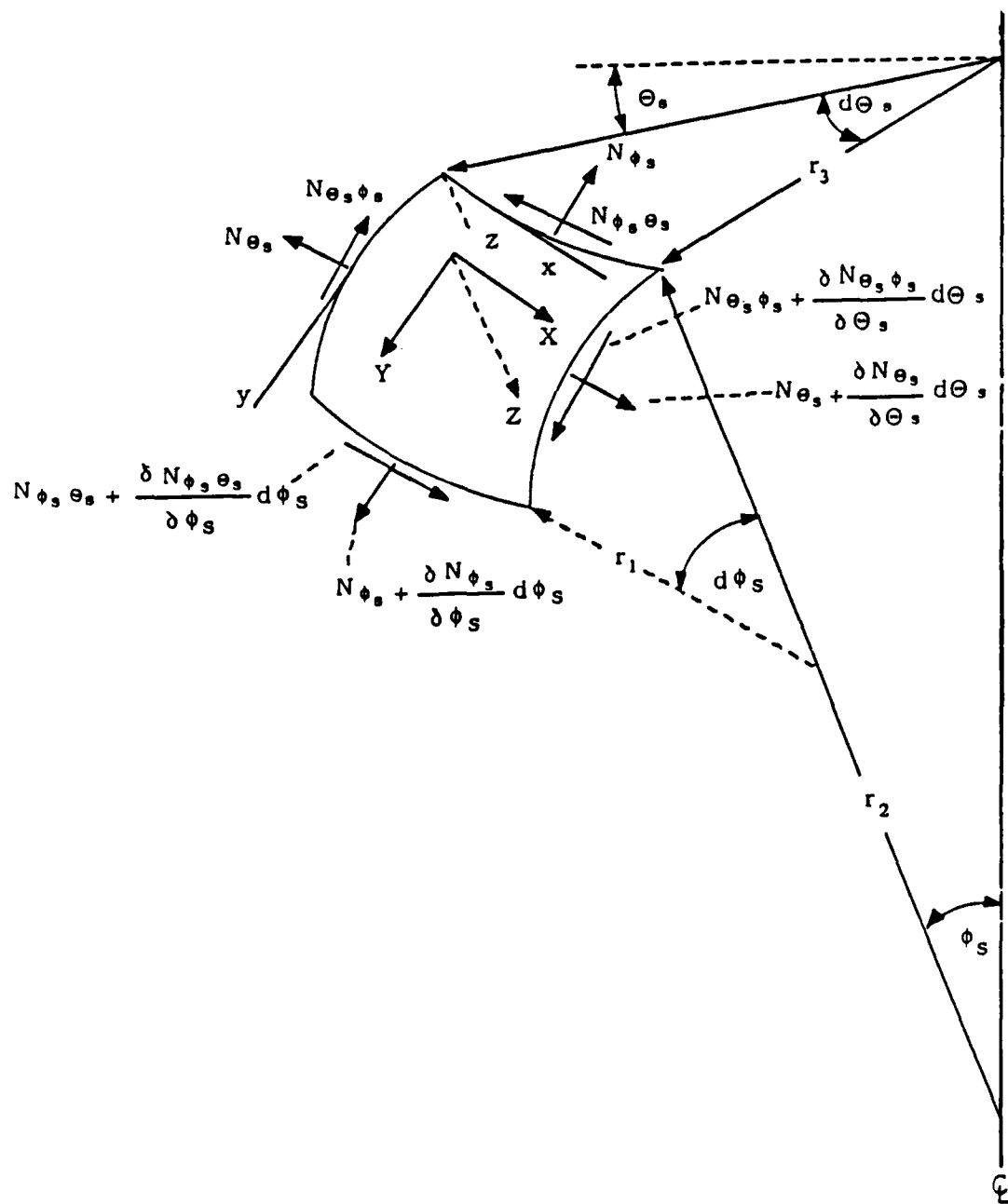


Fig. 7. Shell element of revolution.

2.3.2 Finite Element Solution

The finite element method was chosen to solve for the flexibility coefficients for shells of revolution. An assemblage of thin "quadrilateral shells" from the ANSYS Engineering Analysis System (1985) were used. (See Fig. 8 for an illustration of the ANSYS quadrilateral shell element.) The global stiffness matrix was assembled by ANSYS taking into account both membrane (in-plane) and bending (out-of-plane) stresses. The element is actually a thin flat plate derived from thin plate theory simplified by the Kirchhoff assumptions:

- i) Straight lines initially perpendicular to the reference surface remain straight and perpendicular to that surface after deformation. (Therefore, no out-of-plane shear deformation is included in the analysis.)
- ii) Line segments initially perpendicular to the undeformed reference surface suffer neither extension nor contraction. (No thickness changes.)

The element stiffness matrix is assembled by accounting for the stiffness contributions due to in-plane stresses and out-of-plane stresses separately and then assembling these contributions together to form the element stiffness matrix.

First, for the in-plane membrane stresses, from the additional Kirchhoff assumption;

- iii) The transverse stresses are assumed small in comparison to in-plane membrane stresses. (Thus for the strains, $e_{xz} = e_{yz} = e_{zz} = 0$).

and the theory of elasticity, the strain relations become;

$$e_x = \frac{\partial u}{\partial x} \quad (32)$$

$$e_y = \frac{\partial v}{\partial y} \quad (33)$$

$$e_{xy} = \frac{\partial u}{\partial y} + \frac{\partial v}{\partial x} \quad (34)$$

In addition, for the in-plane stresses, small rotational stresses are accounted for using the method of Zienkiewicz (1977). Next, for the out-of-plane bending finite element shape functions, the above Kirchhoff assumption (iii) does not apply. The method of the DKT Triangle of Batoz et al., (1980) and Razzaque (1984) is used for the development of these out-of-plane bending strain contributions to the element stiffness matrix.

Once the strain relations and displacement functions are defined as above, ANSYS uses the energy method of solution for the loaded structure. The principle of virtual work used is

$$\delta V = \delta U \quad (35)$$

where the virtual strain energy is expressed as

$$\delta U = \int_{Vol} \{\delta e\}^T \{\sigma\} d(Vol) \quad (36)$$

where the strain vector is as defined in equations (32), (33), (34) with the displacement functions of Zienkiewicz (1977), Batoz et al., (1980) and Razzaque (1984) substituted in the equations for u and v . The stress vector is associated with the strain vector by the constitutive equations.

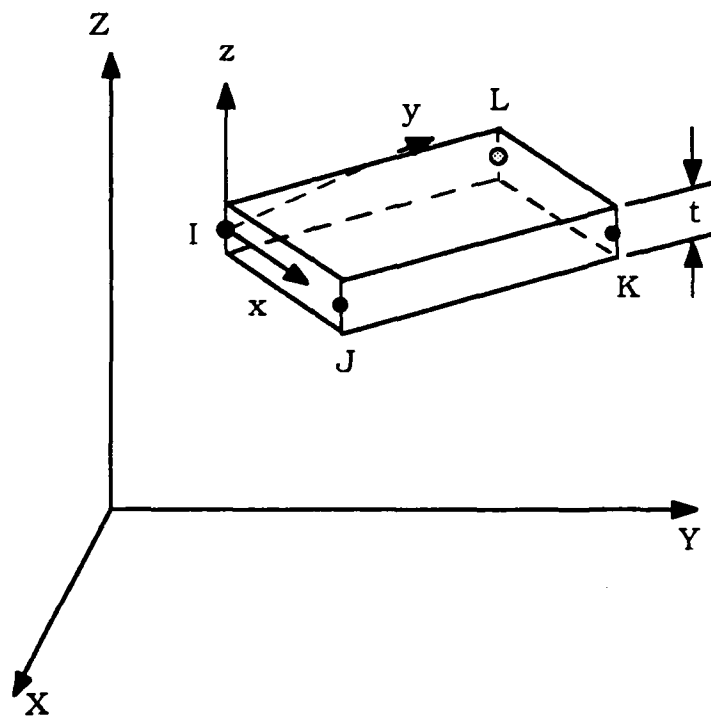


Fig. 8. ANSYS quadrilateral shell element.

3. OVALIZATION RESEARCH

The ovalization research was accomplished in order to quantify the effect of ovalization on the shell flexibility coefficients. It was determined that the effects were negligible for the shell geometries and loading applicable in the rotordynamics industry.

3.1 Ovalization of Shells of Revolution

One objective of this research was to investigate and determine the effect of ovalization on the transverse bending behavior of thin-walled shells of revolution as used for example in gas turbine engine casings. Ovalization is a geometric nonlinear deformation process. This nonlinear behavior to collapse of shell structures under a bending load is a complex problem even for shells of simple geometry.

L.G. Brazier (1927) is attributed with the first theoretical analysis attempting to quantify ovalization in his paper entitled "On the Flexure of Thin Cylindrical Shells and other "Thin" Sections." For pure bending, Brazier (1927) used the theory of minimum strain energy coupled with the theory of flexure displacement for a circular cylindrical thin-walled shell of infinite length. To obtain the equations of equilibrium, first and second order terms were taken into account giving rise to the nonlinear equations. According to Brazier (1927), the shear effects quantified in third and higher order terms need not be taken into account as long as the cylindrical shells are "sufficiently thin." With the equations developed for an infinitely long cylinder, no boundary condition end effects had to be accounted for. Because maximum ovalization occurs at maximum length over radius ratio ($\frac{l}{r}$), any decrease in the ($\frac{l}{r}$) ratio will decrease the amount of ovalization predicted by Brazier (1927) for an infinitely long cylindrical shell.

As seen in Fig. 9, the linear theory of flexure developed by St. Venant (as stated in Brazier (1927)) predicts a much different force-displacement relationship than the nonlinear prediction given by Brazier (1927). Note here that the axis centerline curvature, c , is inversely proportional to the radius of curvature, r_c . It should be noted that St. Venant's solution had only taken first order terms of flexure into account, thus predicting the bending behavior of a non-deforming circular rigid cross section along the entire length of the cylindrical shell. However, it should also be noted that for small displacements of cylindrical shells of small ($\frac{l}{r}$) ratios, St. Venant's linear theory of flexure is very accurate. Theoretically, all finite length cylindrical shells will behave in a manner somewhere between the two limiting cases of St. Venant and Brazier (1927).

The need here is to quantify the effect of ovalization on the flexibility coefficients for cylindrical shells of practical engineering application such as gas-turbine engine casings. Referring to Fig. 9, St. Venant's solution is represented by the equation;

$$M_b = E\pi r^3 t c \quad (37)$$

However, the governing differential equation presented by Brazier (1927) is;

$$\frac{\partial^6 v}{\partial \psi^6} + 2 \frac{\partial^4 v}{\partial \psi^4} + \frac{\partial^2 v}{\partial \psi^2} = \frac{-18c^2 r^5}{t^2} (1 - \nu^2) \sin(2\psi) \quad (38)$$

(These variables are illustrated in Fig. 10.) The solution is represented by the equation;

$$M_b = \frac{E\pi r^3 t}{2} \left[2c - \frac{3r^4 c^3 (1 - \nu^2)}{t^2} \right] \quad (39)$$

For a maximum bending moment denoted by point A of Fig. 9;

$$\overline{M} = \frac{2\sqrt{2}E\pi r t^2}{9(1 - \nu^2)^{\frac{1}{2}}} \quad (40)$$

and,

$$\Delta w = \frac{2}{9}r \quad (41)$$

(See Fig. 11 for an illustration of this Δw Brazier flattening (ovalization).) It should be noted that for pure bending, the Brazier flattening of equation (41) gives the maximum ovalizing at point A of Fig. 9.)

According to Antonenko (1981), "*The phenomenon of ovalization of a circular cross section in the bending of a shell as a beam is attributable to the effect of additional loads which arise in the process of curvature of the shell axis. The pattern of loading may be described as follows. In bending of the shell axis, tensile axial forces on the convex side and compressive forces on the concave side yield resultants directed toward the shell axis. Ovalization of the cross section takes place under the influence of these loads.*" (Refer to Fig. 12 for a graphical representation of these resultant forces.) Antonenko (1981) accounted for ovalization in an infinite system of coupled differential equations which he solved by successive approximations. Antonenko claims that ovalization need be taken into account only for cylindrical shells with large ($\frac{l}{r}$) ratios and very small ($\frac{t}{r}$) ratios (thin-walled) only. No limiting ratios were given. However, limiting ratios are established in the following Ovalization Research Section.

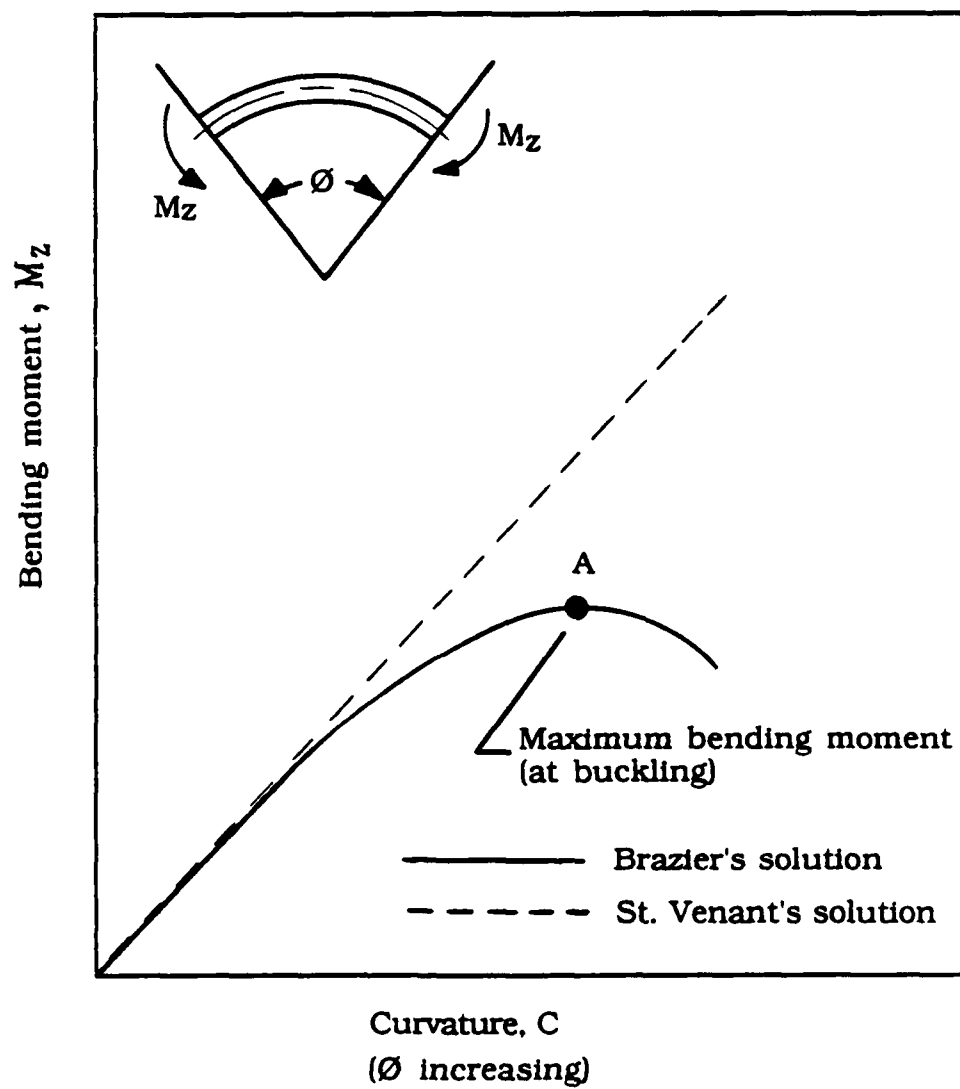


Fig.9. Brazier's nonlinear solution compared with St. Venant's linear solution.

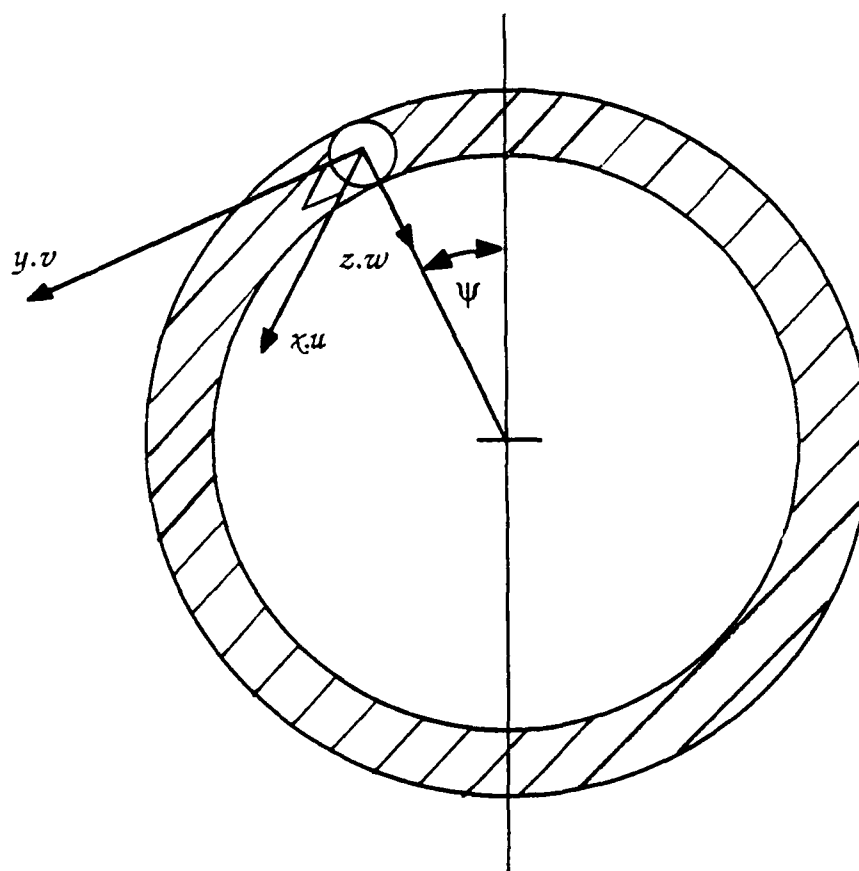


Fig. 10. Brazier's coordinate system for a cylindrical cross section.

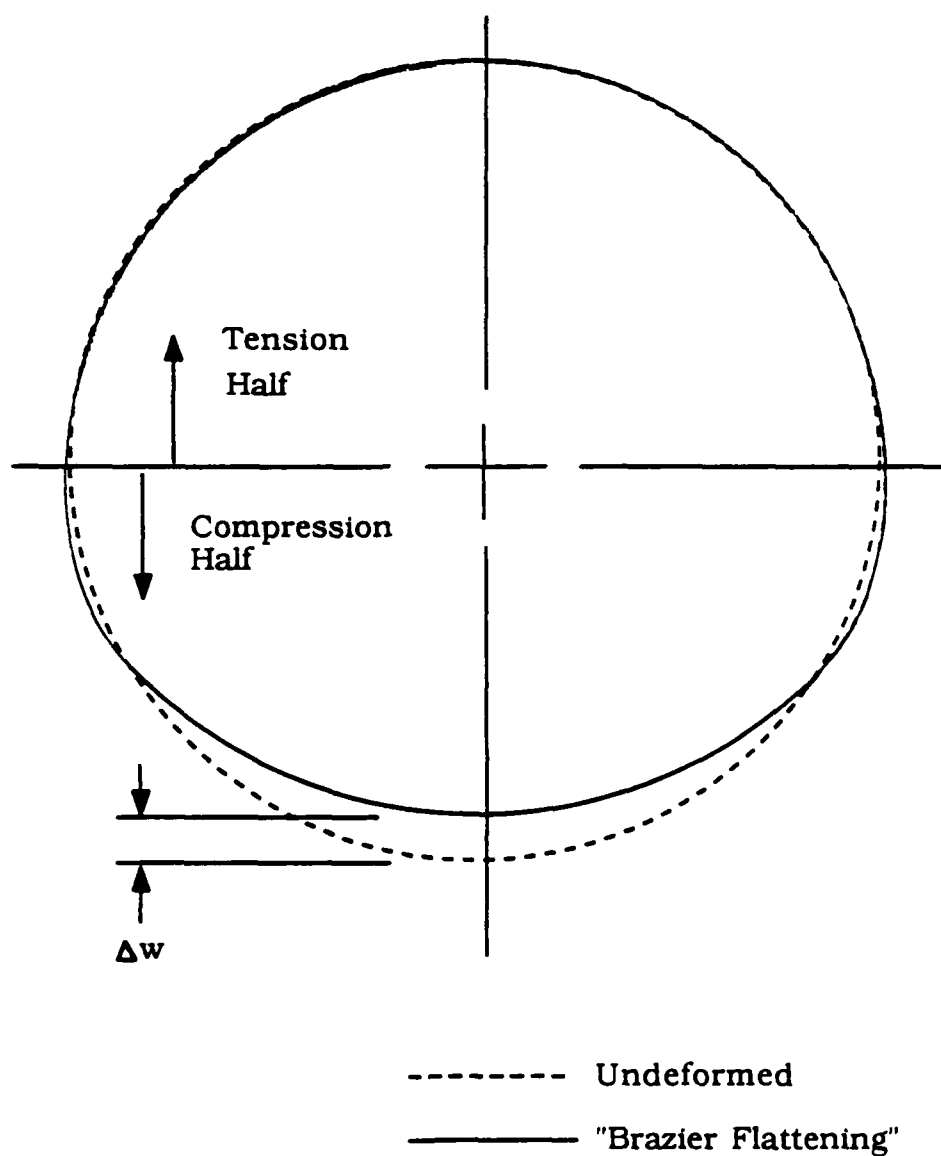
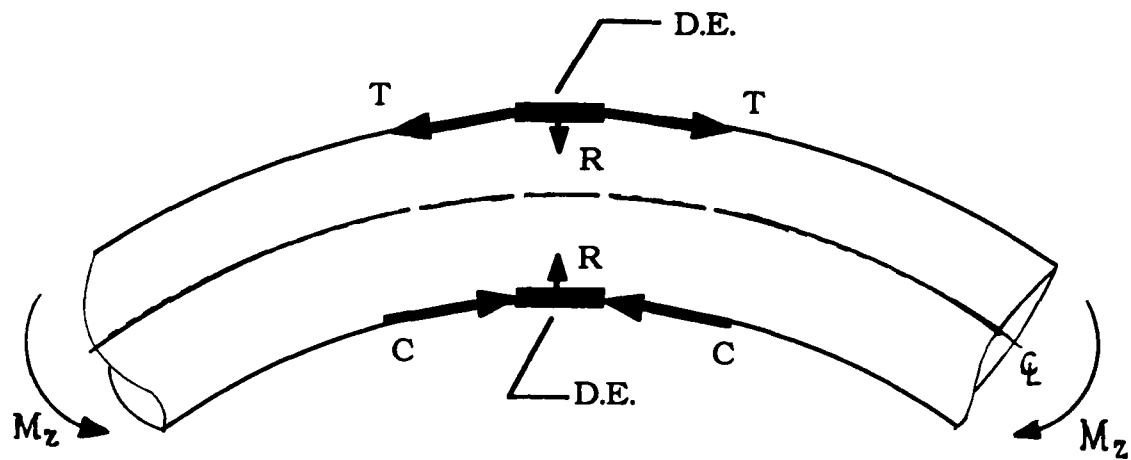


Fig. 11. Brazier flattening (ovalization.)



C: Compressive force
T: Tension force
R: Resultant force
D.E.: Differential element

Fig. 12. Antonenko mechanization of ovalization.

3.2 Computational Analysis

Stephens et al., (1975) generated finite difference models using the STAGS computer code. The models were isotropic cylindrical shells with $(\frac{t}{r}) = .01$, $E = 1.0 \times 10^7 \text{ psi.}$ and $\nu = 0.3$. The $(\frac{l}{r})$ ratio was varied from model to model. A moment couple for pure bending, M , was applied. Both ends of the cylindrical shell were essentially rigid (no ovalization at ends). The finite difference grid point spacing was varied in both the axial and circumferential directions to allow for a finer mesh concentration at the expected maximum ovalization region (midspan compression). The STAGS code used a linear flexure theory coupled with a nonlinear geometric "fudge factor" to allow for the expected nonlinear prebuckling state.

The deformation shape output by the above mentioned STAGS computer code was controlled to deform as shown in Fig. 11. Fig. 13 illustrates the ovalization dependence upon the $(\frac{l}{r})$ ratio. As shown in equation (42), the critical bending moment, M_{cr} , is solely dependent upon the cylindrical shell geometry and Young's Modulus of elasticity.

$$M_{cr} = 0.6E\pi r t^2 \quad (42)$$

M is the bending moment applied given in equations (39) and (40). Stephens et al., (1975) combined equations (40) and (42) to obtain the moment ratio for a Brazier infinite cylindrical shell for this particular shell model geometry;

$$\frac{\overline{M}}{M_{cr}} = \frac{2\sqrt{2}E\pi r t^2}{9(1 - \nu^2)^{\frac{1}{2}}} \times \frac{1}{0.6E\pi r t^2} \quad (43)$$

or for a poisson's ratio = 0.3, by substitution and algebra;

$$\frac{\overline{M}}{M_{cr}} = 0.55 \quad (44)$$

Also, by combining the model geometry of $\frac{t}{r} = .01$ and Brazier's equation (41),

$$\frac{\Delta w}{t} = \frac{2}{9} \times \frac{r}{t} = 22.22 \quad (45)$$

It is important to note in Fig. 13 that the envelope curve for the model approaches the predicted value of Brazier's equation for an infinite cylindrical shell. It is also important to note that for all $(\frac{l}{r})$ ratios, ovalization does occur but is negligible for small $(\frac{l}{r})$ ratios. Circumferential flattening or ovalizing of the cross section is more and more nonlinear for higher and higher $(\frac{l}{r})$ ratios. The major percentage of ovalization (when large ovalization does occur) takes place at or near the buckling load. Refer to Table 1 for calculations of actual change in diameter over thickness, $(\frac{\Delta w}{t})$ ratios, for the models represented in Fig. 13. It is very important to note from Table 1 that for small bending moments and neutral axis displacements, ovalization becomes very small.

Additional computational analysis was performed for cylindrical and conical sections using ANSYS. The results confirm negligible ovalization for geometries and loadings of practical interest. (See the numerical results and discussion of section 5.)

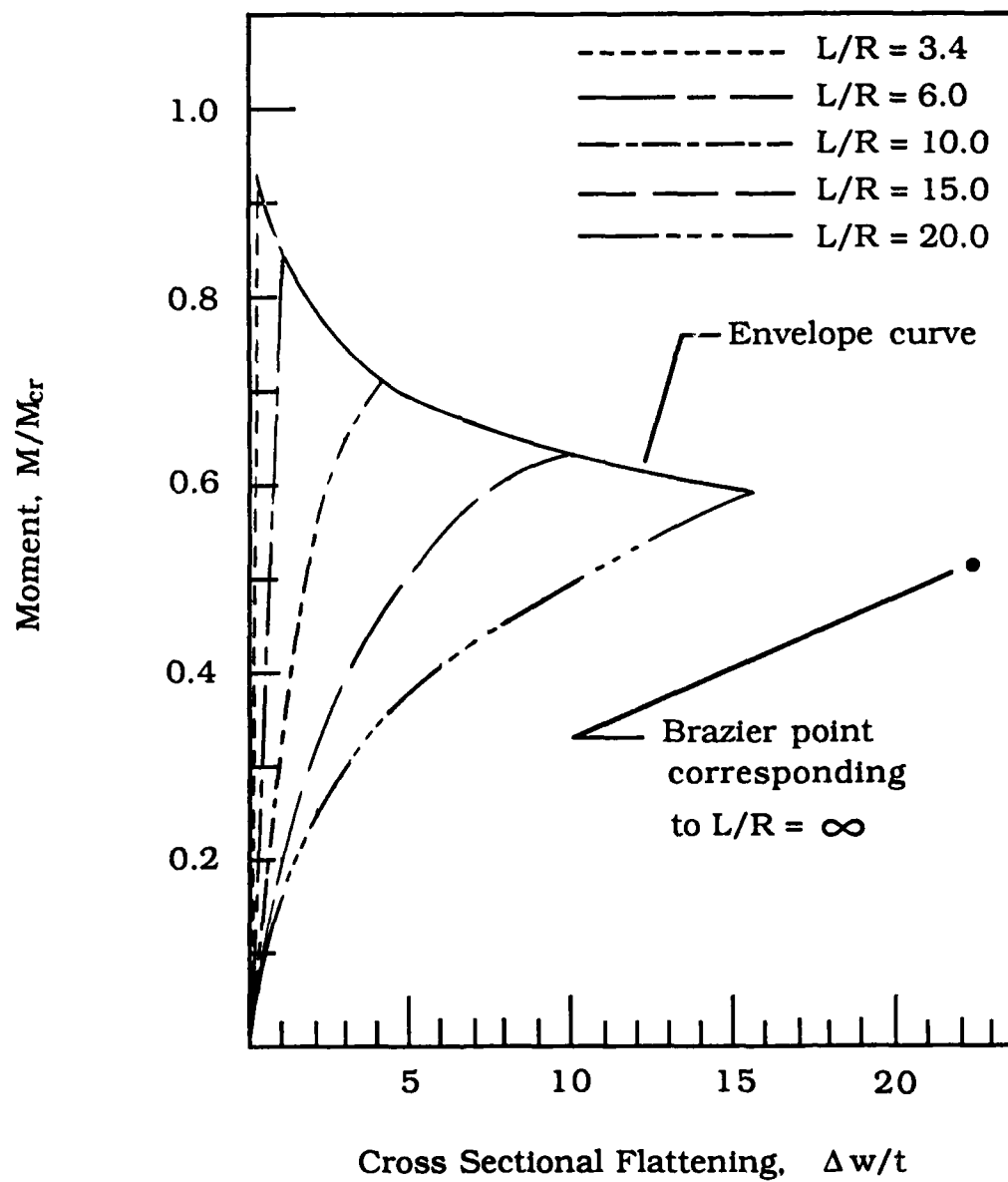


Fig. 13. STAGS computer code envelope curve for Brazier flattening.

Table 1. Nondimensional Ovalization ($\frac{\Delta w}{t}$) for Thin Cylindrical Shells Under Varying Bending Load with $(\frac{t}{r}) = .01$, Varying $(\frac{l}{r})$ ratio.

$\frac{l}{r}$	@ Buckling Load	@ $\frac{1}{2}$ Buckling Load	@ $\frac{1}{4}$ Buckling Load	@ $\frac{1}{8}$ Buckling Load
3.4	0.2	0.09	0.03	0.01
6	1.0	0.4	0.15	0.03
10	4.1	0.8	0.20	0.05
15	9.7	1.5	0.40	0.08
20	15.7	2.0	0.45	0.10

3.3 Experimental Verification

Experiments were carried out by Brazier (1927) with long ($\frac{l}{r} = 45$) thin tubular beams made of celluloid and loaded in pure bending. All specimens deformed into the quasi-oval form of Fig. 11 at high loads near buckling. The nature of the force verse neutral axis curvature is shown in Fig. 14. It is very important to note that deviation from the linear St. Venant's solution is negligible until near buckling loads are applied. Notice as stated earlier, that the experimental tubes do behave in between the two limiting cases of St. Venant linear theory and Brazier's (1927) geometric nonlinearity theory. These experiments by Brazier (1927) also agree with the computational results of Stephens et al., (1975).

Experiments by Lundquist (1933 and 1935) show that for hundreds of metal tubes ranging with ($\frac{l}{r}$) ratios up to 5 and very thin-walled ratios ($\frac{t}{r}$) down to .0015, there was no measured ovalization. St. Venant's linear theory of flexure was perfectly suitable for these specimens. Osgood's (1938) experiments record no ovalization for metal specimens with ($\frac{l}{r}$) ratios up to 10, but for ($\frac{l}{r}$) ratios greater than 10 ovalization was observed however small. Roark's (1941) experiments record no ovalization for metal specimens with ($\frac{l}{r}$) ratios ranging up to 2. Wilson's et al., (1941) experiments record no ovalization for shells with ($\frac{l}{r}$) ratios ranging up to 2.4. Gerard et al., (1968) concluded on these experiments that the Brazier effect is only seen in cylindrical shells with high ($\frac{l}{r}$) ratios, thin-walled, and even then only at high loads near buckling.

According to Bushnell (1981), the nonlinear prebuckling effects of Brazier flattening have a significant impact upon the buckling load. However, at loads well below the buckling load, the effects are insignificant. The nonlinear pre-

buckling effects of Brazier flattening do cause a drop off in cylindrical shell stiffness. However, this nonlinear stiffness effect is only significant at high Brazier flattening.

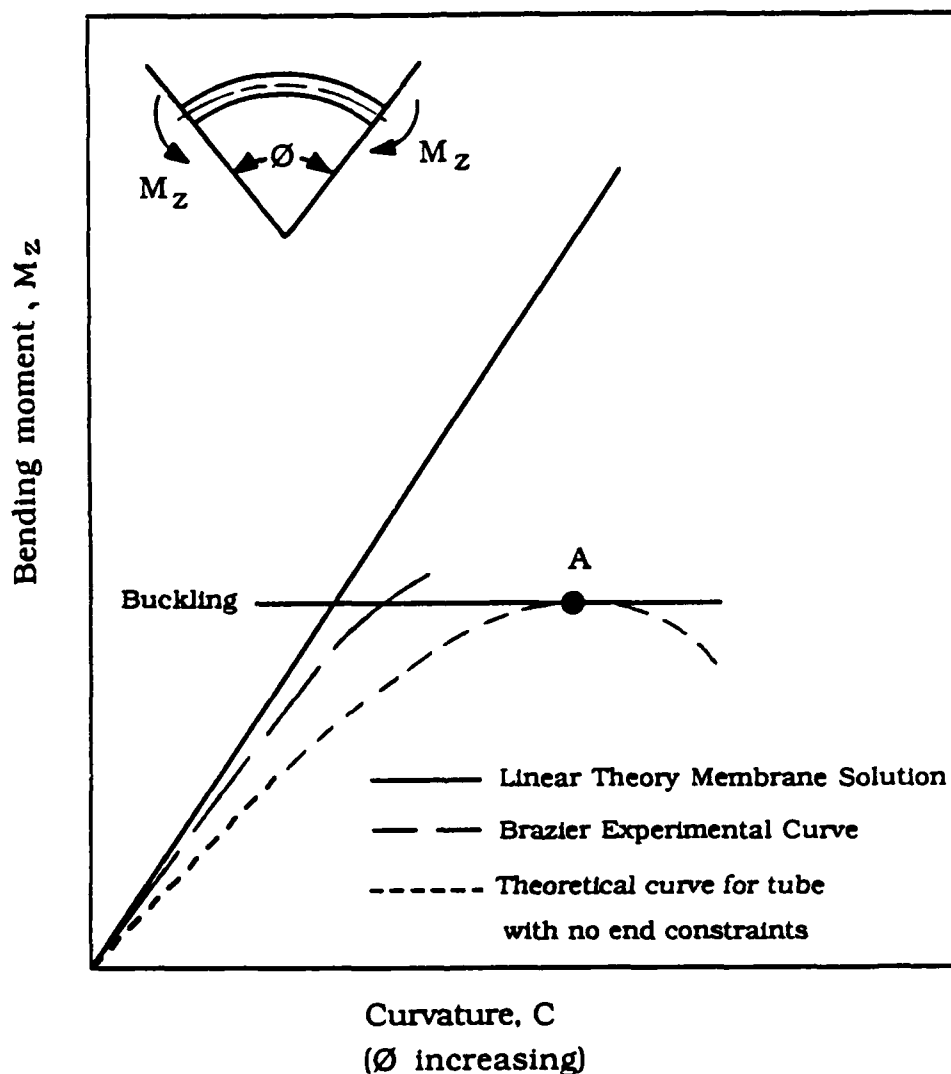


Fig. 14. Brazier's experimental plot compared with Brazier's theoretical plot compared with St. Venant's linear plot.

3.4 Ovalization Conclusions

The following conclusions are emphasized as the important ideas which should be understood from this ovalization study.

A closed form linear solution relating bending moment to curvature of neutral axis does exist for cylindrical shells in pure bending. This is called St. Venant's theory of flexure. This linear solution assumes no change in cross section throughout deflection.

A closed form nonlinear solution relating bending moment to curvature of neutral axis does exist for cylindrical shells in pure bending. This is called Brazier's theory of flexure which accounts for second order terms introduced by "Brazier flattening" or ovalization.

The Brazier flattening is more pronounced on the compression side of the cylindrical shell.

Thin-walled cylindrical shells with low ($\frac{l}{r}$) ratios bend according to the linear solution on which the flexibility calculations of this work is based.

In applications such as gas turbine engine casings, and rotor shaft sections, stiff boundary conditions usually restrict cross section ovalization thus making the contribution of the Brazier flattening even more negligible.

It is very important to note that deviation from the linear St. Venant's solution is negligible until near buckling loads are applied. This is true for even the large ($\frac{l}{r}$) ratios and small ($\frac{t}{r}$) ratios of less than .01.

Because of this Brazier flattening deformation behavior, for small loads and consequently small neutral axis displacements, ovalization of the cylindrical shell cross section has almost no effect upon the linearity of the load-displacement (stiffness) curves for even large ($\frac{l}{r}$) ratios in transverse bending.

3.5 Additional Comments

It should also be noted that from the Stephens et al., (1975) computational solutions, ambient pressure has an effect on the Brazier flattening. External pressures applied to a cylindrical shell accentuate or increase the Brazier flattening while internal pressures lessen the Brazier flattening. Thus for turbomachinery with high internal pressure such as in a gas turbine engine, even less Brazier flattening will occur. Brazier flattening is also affected by the Young's modulus of the material. In the limiting case, a completely strain hardened material will have a much smaller neutral-axis deflection with load and thus a much smaller Brazier flattening.

The Brazier flattening phenomenon will have an effect on the dynamical behavior of cylindrical shells. However, this effect will be negligible in cylindrical shells with boundary conditions limiting the Brazier flattening. Because the Brazier flattening deformation is opposite in direction to the dynamic response deflection, a small reduction (if any) in the first bending natural frequency of the cylindrical shell would be expected. With the cyclic deformation shapes expected similar to Fig. 11, the small fluctuations in the effective inertia should occur but are expected to be negligible. Also, with Brazier flattening, this increase in deflection of the shell should increase the differential element velocities and thus increase the internal material damping, an effect expected to be negligible.

4. FINITE ELEMENT COMPUTATIONAL ANALYSIS

The finite element method was used to solve for the flexibility coefficients of the conical structures of interest. The ANSYS engineering analysis computer code was used to generate the shell models, boundary conditions, meshes and solutions for these conical structures. The models and boundary conditions are defined. The meshes for these models are discussed and sample illustrations given.

4.1 Models Defined

Two hundred and seventy five finite element models were generated. These included all combinations of the parameters;

$$\frac{l}{r} = .25, .5, 1, 2, 4$$

$$\frac{t}{r} = .0125, .025, .05, .1, .2$$

$$\theta = -75^\circ, -60^\circ, -45^\circ, -30^\circ, -15^\circ, 0^\circ, 15^\circ, 30^\circ, 45^\circ, 60^\circ, 75^\circ$$

Each of the two hundred seventy five had to be tip loaded, first with a unit shear load and solved, and then with a unit pure bending moment and solved. Five hundred and fifty solutions were generated. (See the sample schematic of varying $(\frac{l}{r})$ ratio and varying cone angle θ in Fig. 15.)

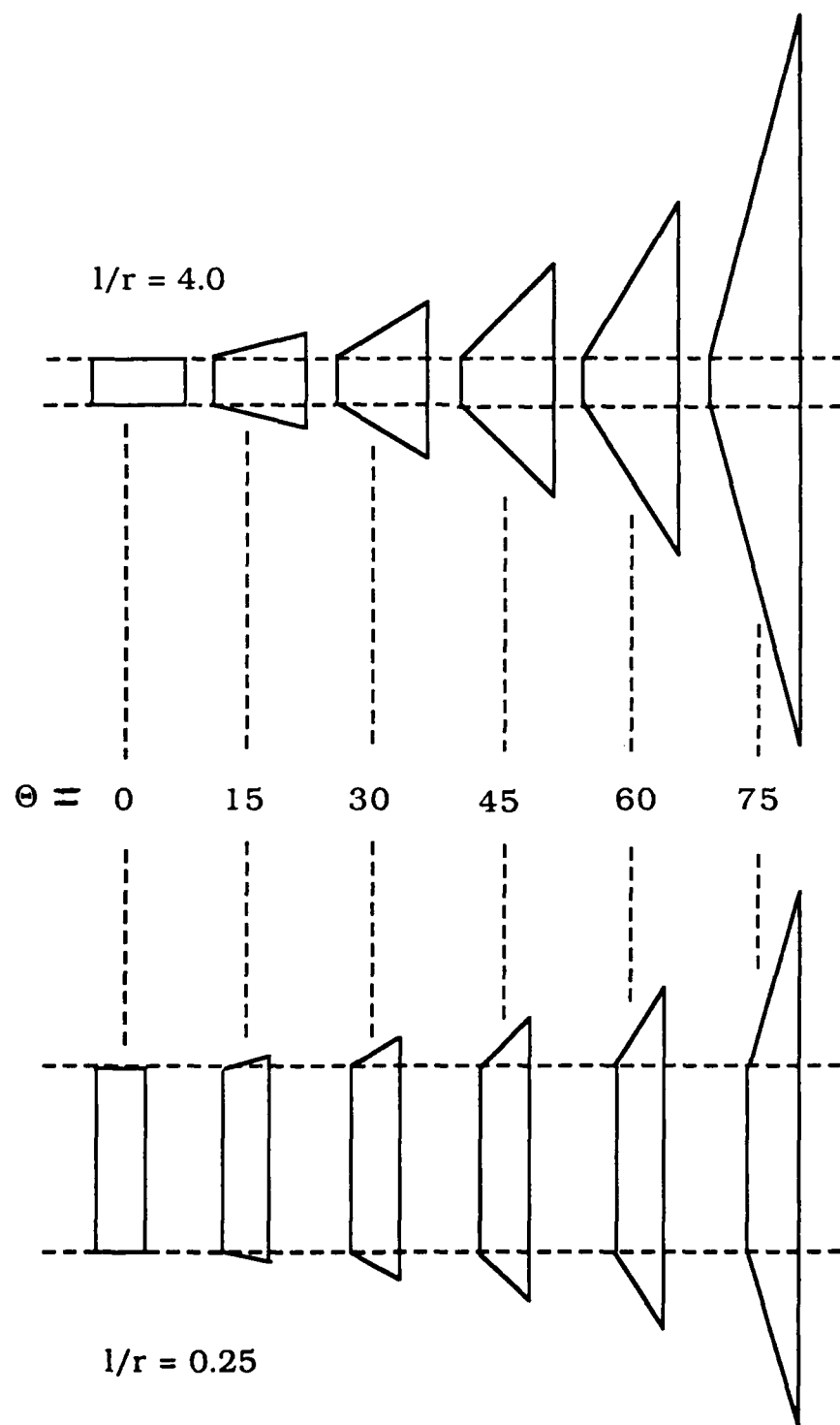


Fig. 15. Varying conical sections schematic.

4.2 Boundary Conditions

For an illustration of the cantilevered conical section with loading applied, see Fig. 16. It is important to note that all models were fixed at the left end. The right end was constrained to remain infinitely rigid by restricting the degrees of freedom for these end nodes. Because the free end was constrained rigid, the load acted as if it was uniformly distributed to each node thus ensuring no distorted loading or local deformations. This is essential in order to obtain the proper displacements and thus flexibility coefficients. (See APPENDIX D for sample input data for ANSYS displacement constraints and rigid region constraints.)

4.3 Mesh Analysis

All models were generated using the ANSYS mesh generation procedure. In general, it is important to keep the individual elements of the mesh within certain dimensional constraints. We can define these constraints as the aspect ratio, $(\frac{l_e}{C_e})$ and the arc angle, θ_c . (Refer to Fig. 17 for an illustration of these parameters.) These constraints are important for any finite element simply because of the limitations on the finite element shape functions derived from the particular structural theory. In order to determine the specific limitations on the aspect ratio and arc angle, meshes of the extreme geometry models ($(\frac{l}{r}) = 4$ with cone angle = 0°) and ($(\frac{l}{r}) = 0.25$ with cone angle = 75°) were meshed first varying only arc angle from 30° to 15° and then varying only the aspect ratio from 15 to 1. The solutions converged to within 0.1% of the coarser mesh solution. The limits on the mesh aspect ratios were thus established at $\theta_c = 15^\circ_{max}$ and $(\frac{l_e}{C_e}) = 6_{max}$. (See Fig. 18 through Fig. 27 for samples of meshes used for the solution generation. See APPENDIX D for sample ANSYS input for model geometry and mesh generation.)

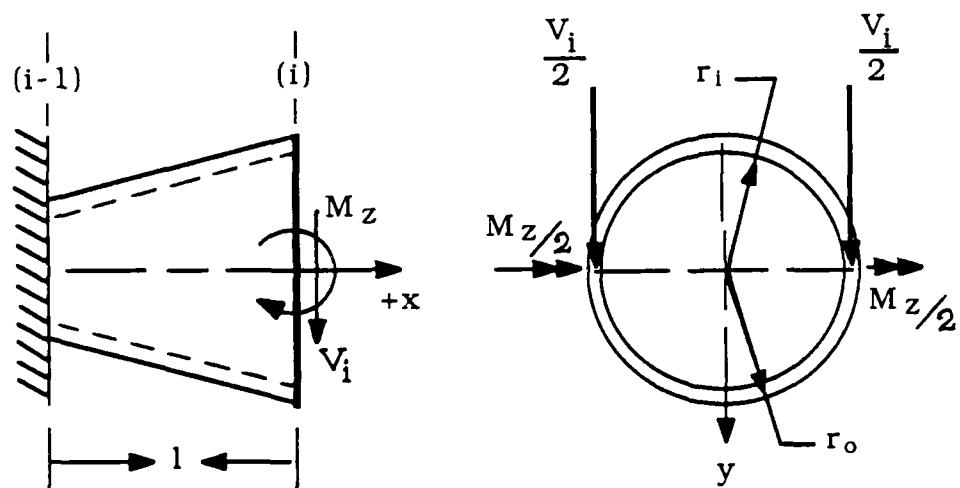


Fig. 16. Cantilevered conical section with tip loading.

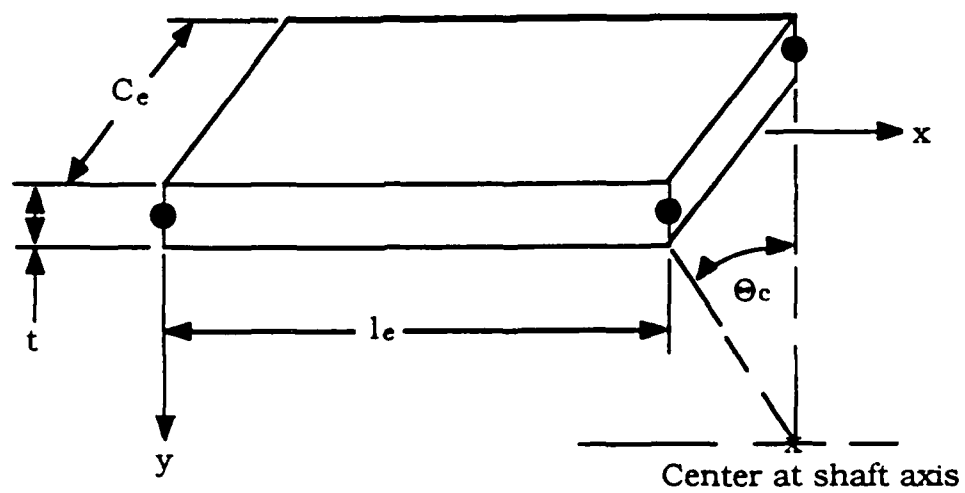


Fig. 17. Flat plate element geometrical constraints.

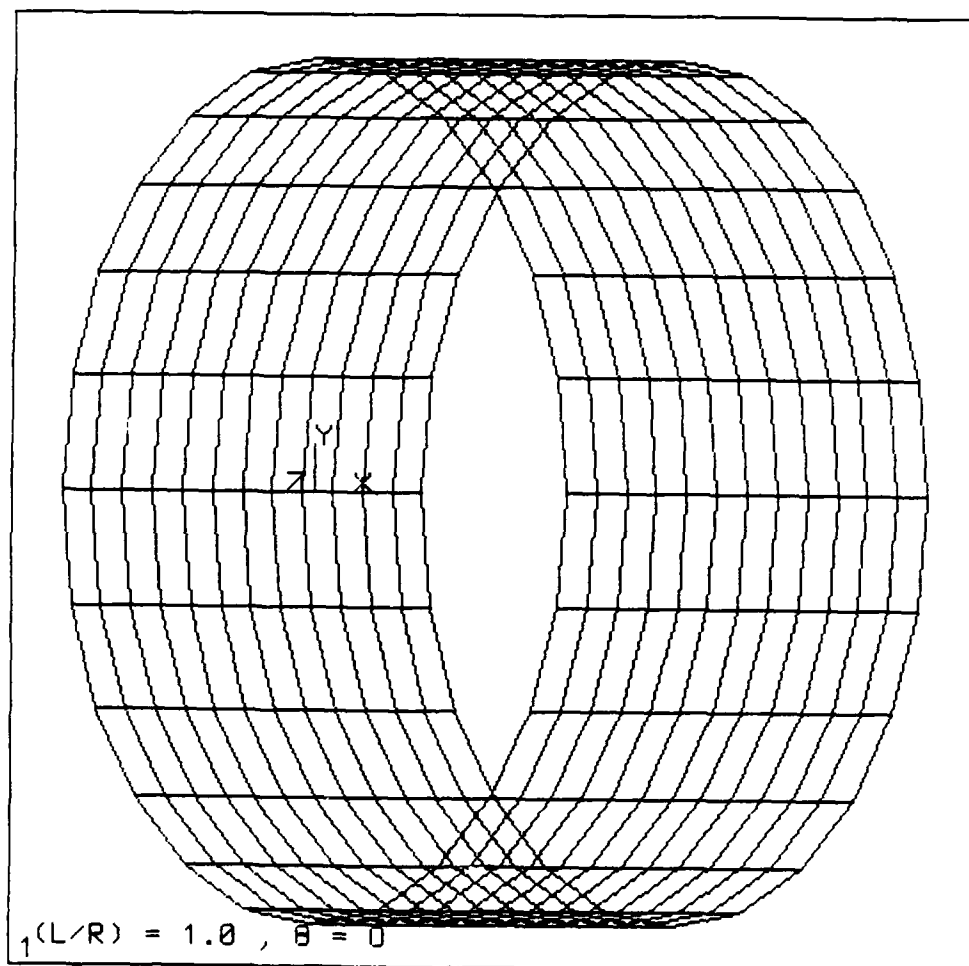


Fig. 18. ANSYS mesh with $(\frac{r_1}{r}) = 1$ and $\theta = 0^\circ$.

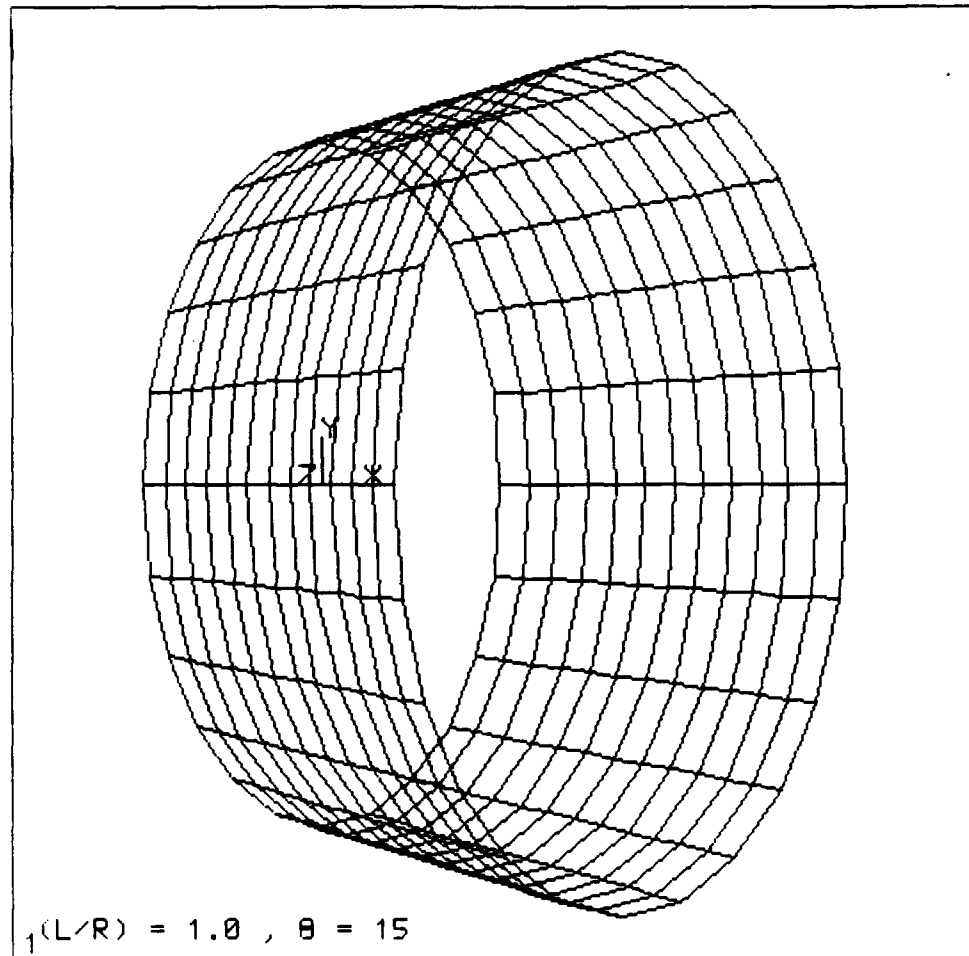


Fig. 19. ANSYS mesh with $(\frac{L}{R}) = 1$ and $\theta = 15^\circ$.

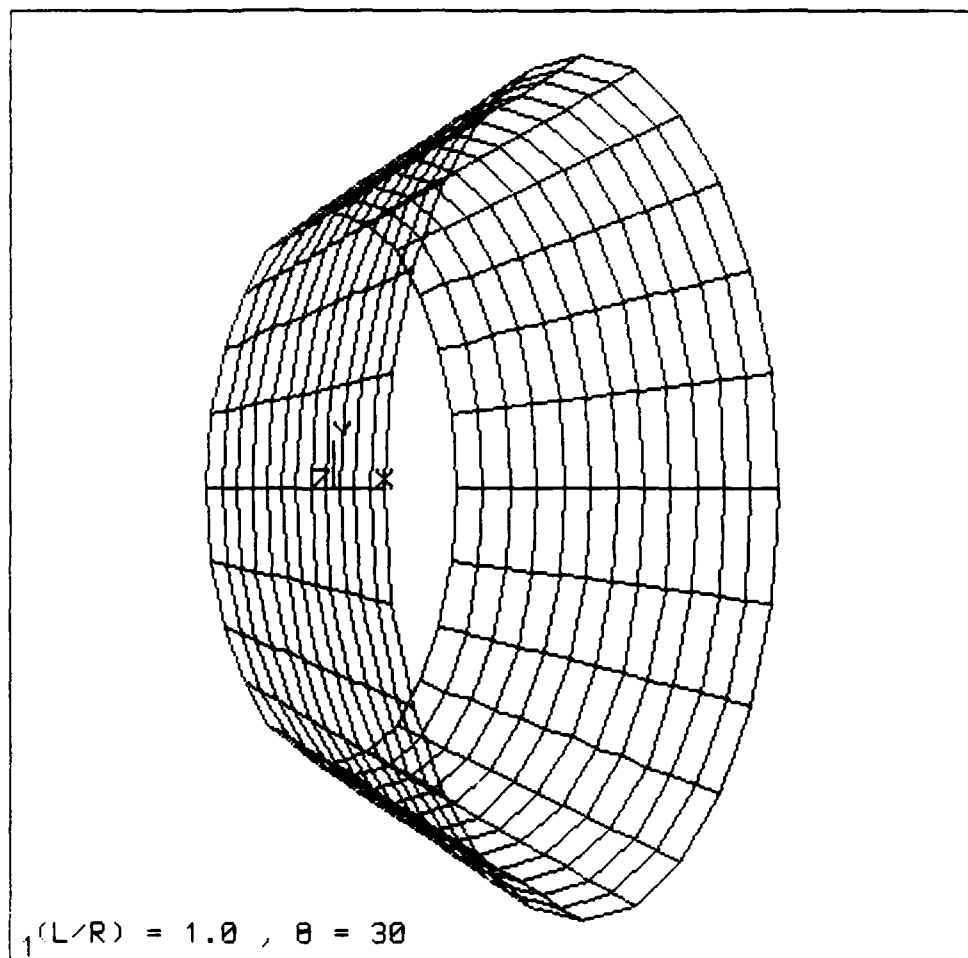


Fig. 20. ANSYS mesh with $(\frac{L}{r}) = 1$ and $\theta = 30^\circ$.

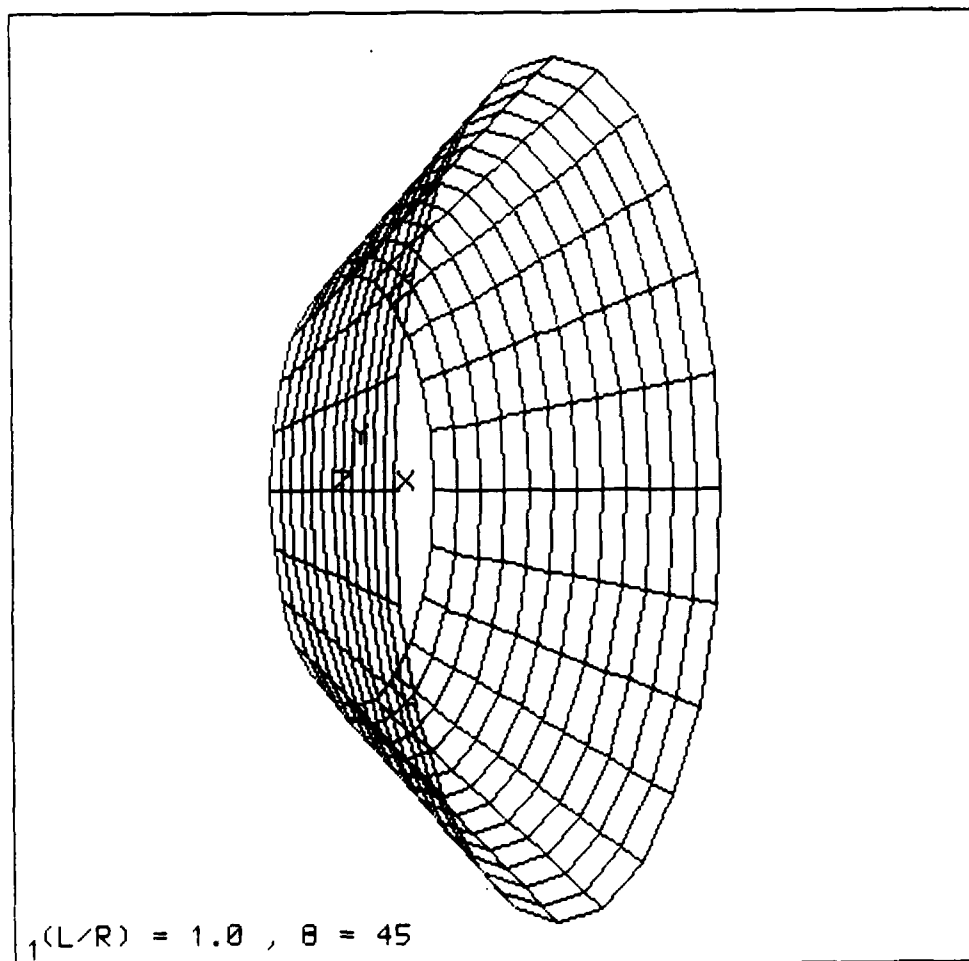


Fig. 21. ANSYS mesh with $(\frac{L}{r}) = 1$ and $\theta = 45^\circ$.

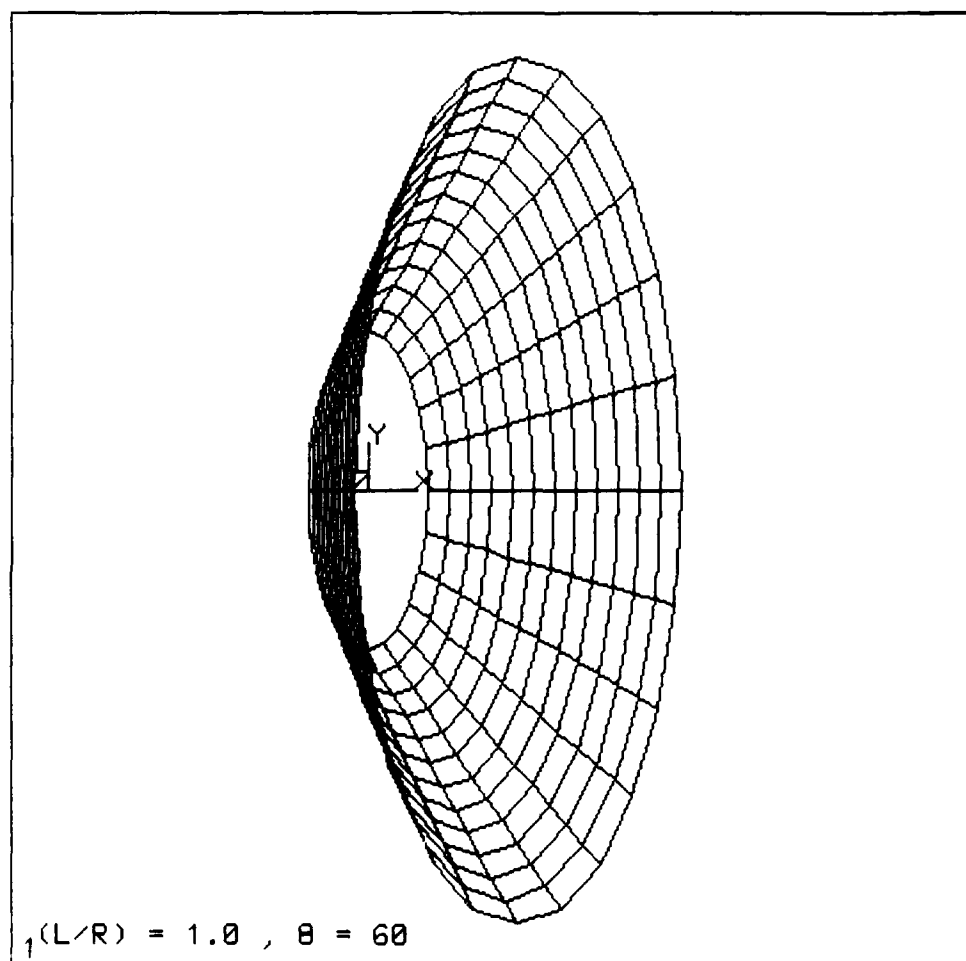


Fig. 22. ANSYS mesh with $(\frac{L}{R}) = 1$ and $\theta = 60^\circ$.

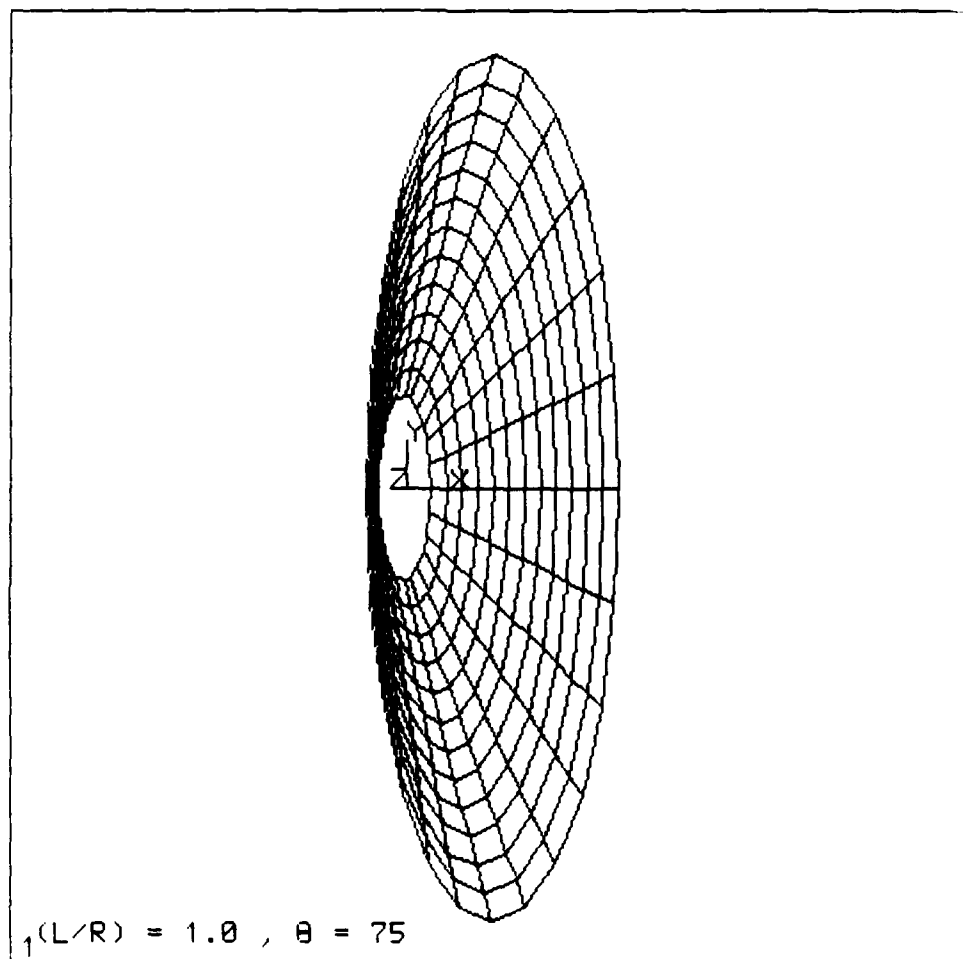


Fig. 23. ANSYS mesh with $(\frac{L}{R}) = 1$ and $\theta = 75^\circ$.

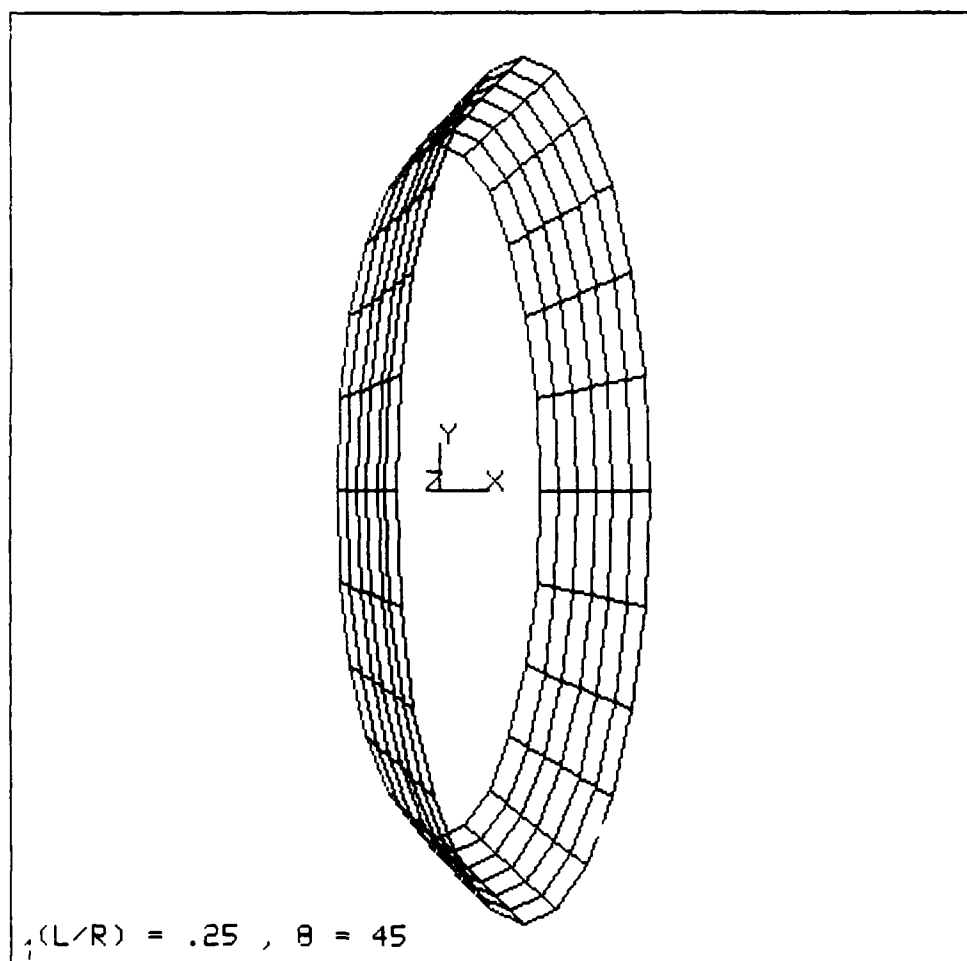


Fig. 24. ANSYS mesh with $(\frac{L}{R}) = .25$ and $\theta = 45^\circ$.

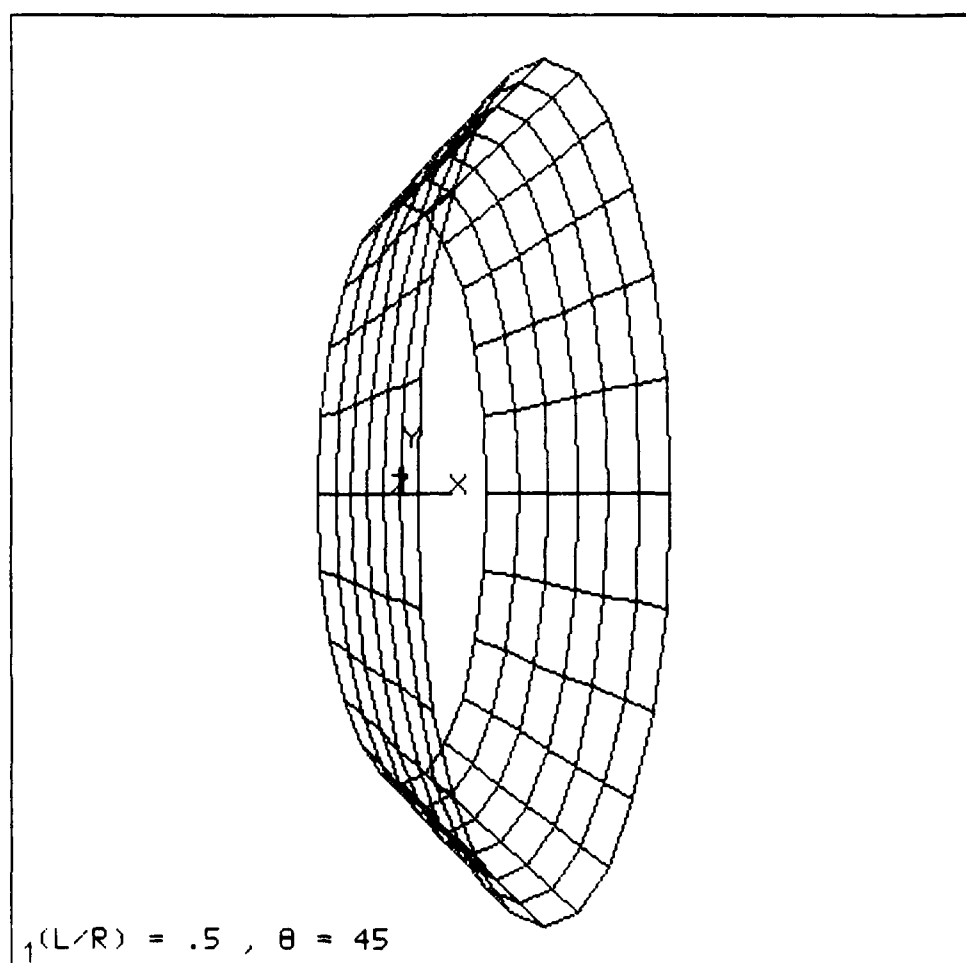


Fig. 25. ANSYS mesh with $(\frac{L}{r}) = .5$ and $\theta = 45^\circ$.

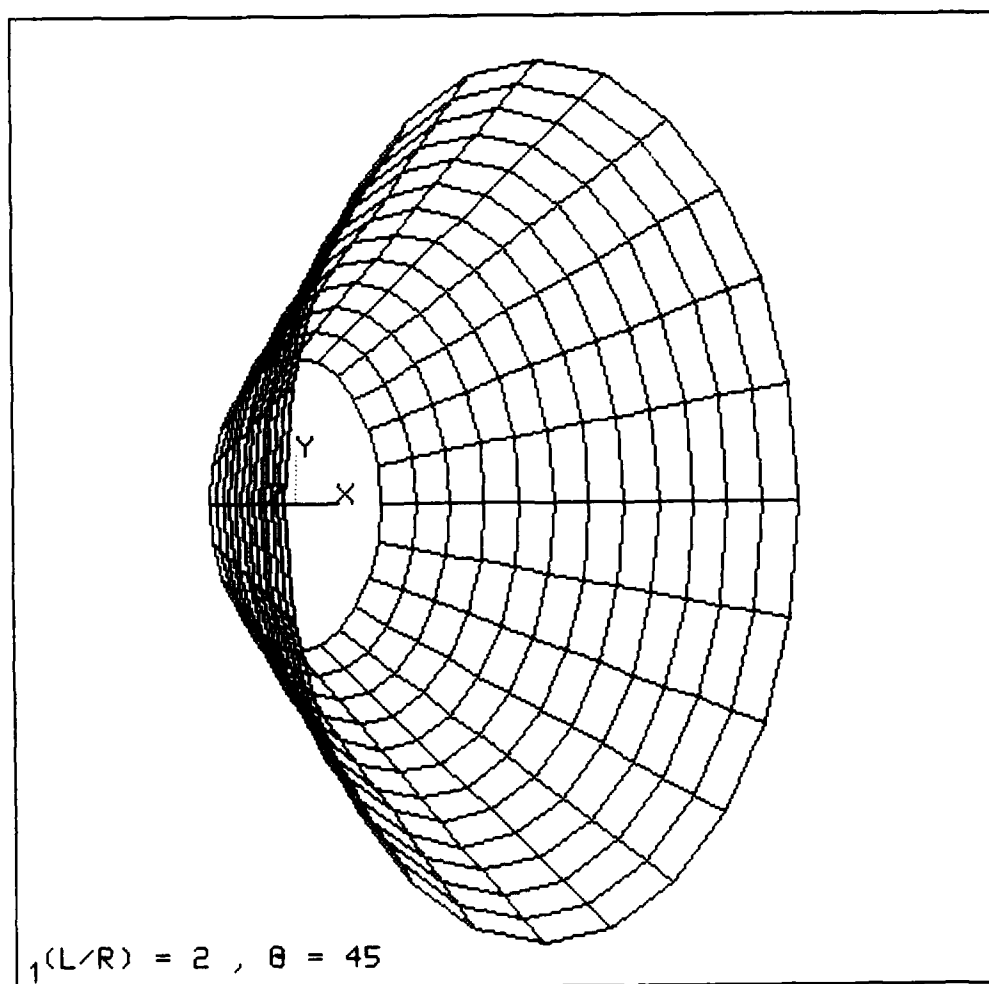


Fig. 26. ANSYS mesh with $(\frac{L}{r}) = 2$ and $\theta = 45^\circ$.

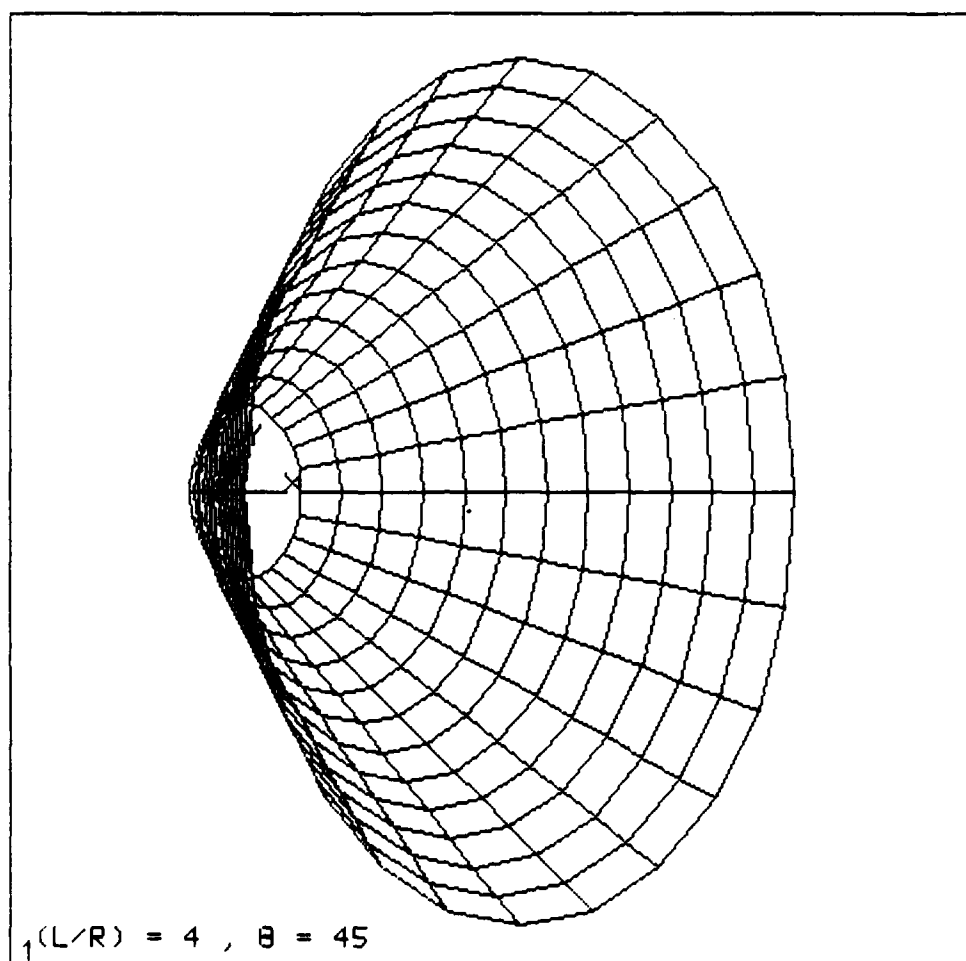


Fig. 27. ANSYS mesh with $(\frac{L}{r}) = 4$ and $\theta = 45^\circ$.

5. NUMERICAL RESULTS AND DISCUSSION

Ovalization has been demonstrated to be negligible using ANSYS for transverse loading conditions found in turbomachinery. A discussion of these ovalization tests is presented. The flexibility coefficients are presented in nondimensionalized tabular and plot form for ease in turbomachinery design and analysis application. The shell finite element models have been verified by comparison with solutions from advanced strength of materials. The satisfaction of the mathematical flexibility transformation identities is also presented as verification of the model boundary conditions. A discussion of current methods of including shear in the closed form beam theory solutions is presented.

Rotor transfer matrix demonstrations were performed on the 60° cone test piece presented by Beamish et al., (1988) and the Space Shuttle Main Engine High Pressure Oxidizer Turbopump (SSME HPOTP) as presented by Li (1979).

5.1 Negligible Ovalization

Based on the ovalization study, three models most likely to ovalize were modeled and analyzed. The parameters chosen for study were $(\frac{l}{r}) = 4$, $(\frac{t}{r}) = 0.0125$, and cone angles 0° , 75° , and -75° . A maximum load based on the worst case vibrational displacement of 200 mils (.2 inches) was used. A load vector based on a linear extrapolation was used to check if the nonlinear analysis would give the same results as the linear analysis. The load vector was obtained from multiplying the unit load vector by 200 mils and dividing by the tip displacement at unit load. The large displacement nonlinear solution option within ANSYS was selected and each solution converged within three iterations. The tip and midlength ($\frac{l}{2}$) nodal displacements were output. For all three models, there were no changes in midlength diameters and the tip deflections were 200 mils indicating a linear flexibility throughout this loading range. Because no ovalization was measured, all 275 models were solved with a linear analysis with one load step

5.2 Design Data Generation

The data generated for the models described in the previous section were nondimensionalized for ease in turbomachinery design and analysis application. Tables 2 through 4 list the nondimensional flexibility coefficients for cylindrical sections. The values are listed for varying $(\frac{t}{r})$ and $(\frac{l}{r})$ ratios. Tables 5 through 24 also list the nondimensional flexibility coefficients for conical sections. The values are listed for varying cone angle θ , and varying $(\frac{t}{r})$ and $(\frac{l}{r})$ ratios. Figures 28 through 47 are plots of the nondimensional flexibilities listed in Tables 5 through 24 respectively. The plots may be used for quick interpolation of nondimensional flexibilities. Note for the $(aEr_{-\theta} = aEr_{-\theta})$ and $(\alpha Er_{-\theta}^2 = bEr_{-\theta}^2)$ tables and plots, that there are negative values. The curves represent the flexibility characteristics dominated by the shear loading. However, for each curve, the slope is changing and eventually as $(\frac{l}{r})$ increases the flexibility coefficients will be dominated by the bending moment loading and thus become positive. Likewise, the flexibility coefficients $(bEr_{-\theta}^2 = \alpha Er_{-\theta}^2)$ and $(\beta Er_{-\theta}^3 = \beta Er_{-\theta}^3)$ will always be positive because each is uncoupled and represents the flexibility characteristics of the structure solely due to pure bending. In pure bending, there is no shear taken into account. It is important to note for all these nondimensional flexibility plots, that the curves only represent a best fit between the computational data points. The data points were marked on the plots with symbols which represent the only true computational data, the curves between are not computational data. The Tables of the nondimensional flexibilities are contained herein to give the designer or analyst the option of using a numerical interpolation scheme of his choice.

Table 2. Nondimensional Flexibilities (aEr) for Cylindrical Sections ($\Theta = 0$) with Varying ($\frac{l}{r}$) and ($\frac{t}{r}$) Ratios.

$\frac{t}{r}$	$\frac{l}{r}$	aEr
0.0125	0.25	-16.3875
	0.5	-32.5050
	1.0	-61.8909
	2.0	-98.0523
	4.0	10.8891
0.025	0.25	-8.01212
	0.5	-16.1382
	1.0	-30.7997
	2.0	-48.8386
	4.0	5.64177
0.05	0.25	-3.68059
	0.5	-7.88378
	1.0	-15.2192
	2.0	-24.1826
	4.0	3.12114
0.1	0.25	-1.39222
	0.5	-3.61497
	1.0	-7.38548
	2.0	-11.8026
	4.0	1.94488
0.2	0.25	-0.354660
	0.5	-1.35794
	1.0	-3.35416
	2.0	-5.55745
	4.0	1.41685

Table 3. Nondimensional Flexibilities ($bEr^2 = \alpha Er^2$) for Cylindrical Sections ($\Theta = 0$) with Varying $\frac{l}{r}$ and $\frac{t}{r}$ Ratios.

$\frac{t}{r}$	$\frac{l}{r}$	$bEr^2 = \alpha Er^2$
0.0125	0.25	0.753797
	0.5	3.13300
	1.0	12.7363
	2.0	51.3101
	4.0	205.622
0.025	0.25	0.370897
	0.5	1.54250
	1.0	6.32531
	2.0	25.5801
	4.0	102.742
0.05	0.25	0.184290
	0.5	0.754806
	1.0	3.13337
	2.0	12.7302
	4.0	51.2805
0.1	0.25	0.0919208
	0.5	0.371620
	1.0	1.54363
	2.0	6.32142
	4.0	25.5507
0.2	0.25	0.0458154
	0.5	0.184268
	1.0	0.756213
	2.0	3.12746
	4.0	12.6917

Table 4. Nondimensional Flexibilities (βEr^3) for Cylindrical Sections ($\Theta = 0$) with Varying $\frac{l}{r}$ and $\frac{t}{r}$ Ratios.

$\frac{t}{r}$	$\frac{l}{r}$	βEr^3
0.0125	0.25	6.03040
	0.5	12.5320
	1.0	25.4725
	2.0	51.3100
	4.0	102.811
0.025	0.25	2.96719
	0.5	6.16999
	1.0	12.6506
	2.0	25.5801
	4.0	51.3709
0.05	0.25	1.47433
	0.5	3.01922
	1.0	6.26673
	2.0	12.7301
	4.0	25.6404
0.1	0.25	0.735368
	0.5	1.48648
	1.0	3.08726
	2.0	6.32142
	4.0	12.7754
0.2	0.25	0.366524
	0.5	0.737069
	1.0	1.51242
	2.0	3.12745
	4.0	6.34587

Table 5. Nondimensional Flexibilities (aEr) for Conical Sections with $((\frac{l}{r}) = .0125)$, Varying Θ , and Varying $(\frac{l}{r})$ Ratio.

Θ	$\frac{l}{r}$	$aEr_{+\Theta} = aEr_{-\Theta}$
15	0.25	-16.4088
	0.5	-31.6478
	1.0	-57.8755
	2.0	-93.3205
	4.0	-104.709
30	0.25	-17.6177
	0.5	-33.1231
	1.0	-58.8090
	2.0	-95.4185
	4.0	-135.138
45	0.25	-20.5644
	0.5	-37.6571
	1.0	-65.2536
	2.0	-106.495
	4.0	-165.270
60	0.25	-27.1032
	0.5	-48.1376
	1.0	-81.7094
	2.0	-134.742
	4.0	-221.627
75	0.25	-45.4020
	0.5	-77.6723
	1.0	-130.452
	2.0	-221.181
	4.0	-385.649

Table 6. Nondimensional Flexibilities (aEr) for Conical Sections with $((\frac{t}{r}) = .025)$, Varying Θ , and Varying $(\frac{l}{r})$ Ratio.

Θ	$\frac{l}{r}$	$aEr_{+\Theta} = aEr_{-\Theta}$
15	0.25	-8.02446
	0.5	-15.7143
	1.0	-28.8052
	2.0	-46.4997
	4.0	-52.1826
30	0.25	-8.62022
	0.5	-16.4428
	1.0	-29.2559
	2.0	-47.5162
	4.0	-67.3361
45	0.25	-10.0659
	0.5	-18.6749
	1.0	-32.4185
	2.0	-52.9506
	4.0	-82.2487
60	0.25	-13.2575
	0.5	-23.7970
	1.0	-40.4472
	2.0	-66.7359
	4.0	-109.971
75	0.25	-22.0413
	0.5	-37.8917
	1.0	-63.6207
	2.0	-107.963
	4.0	-189.506

Table 7. Nondimensional Flexibilities (aEr) for Conical Sections with $((\frac{t}{r}) = .05)$, Varying Θ , and Varying $(\frac{l}{r})$ Ratio.

Θ	$\frac{l}{r}$	$aEr_{+\Theta} = aEr_{-\Theta}$
15	0.25	-3.68986
	0.5	-7.67802
	1.0	-14.2391
	2.0	-23.0452
	4.0	-25.8297
30	0.25	-3.97299
	0.5	-8.03363
	1.0	-14.4451
	2.0	-23.5077
	4.0	-33.3074
45	0.25	-4.64925
	0.5	-9.11334
	1.0	-15.9531
	2.0	-26.0858
	4.0	-40.5182
60	0.25	-6.12105
	0.5	-11.5506
	1.0	-19.7273
	2.0	-32.5355
	4.0	-53.6437
75	0.25	-10.0532
	0.5	-17.9039
	1.0	-29.9758
	2.0	-50.6176
	4.0	-89.4359

Table 8. Nondimensional Flexibilities (aEr) for Conical Sections with $((\frac{t}{r}) = .1)$, Varying Θ , and Varying $(\frac{l}{r})$ Ratio.

Θ	$\frac{l}{r}$	$aEr_{+\Theta} = aEr_{-\Theta}$
15	0.25	-1.40197
	0.5	-3.52347
	1.0	-6.91415
	2.0	-11.2706
	4.0	-12.5724
30	0.25	-1.52682
	0.5	-3.69121
	1.0	-6.99747
	2.0	-11.4472
	4.0	-16.1763
45	0.25	-1.81070
	0.5	-4.18548
	1.0	-7.67514
	2.0	-12.5752
	4.0	-19.4612
60	0.25	-2.40248
	0.5	-5.26514
	1.0	-9.31562
	2.0	-15.3136
	4.0	-25.0916
75	0.25	-3.89256
	0.5	-7.83074
	1.0	-13.2275
	2.0	-21.9353
	4.0	-38.3099

Table 9. Nondimensional Flexibilities (aEr) for Conical Sections with $((\frac{l}{r}) = .2)$, Varying Θ , and Varying $(\frac{l}{r})$ Ratio.

Θ	$\frac{l}{r}$	$aEr_{+\Theta} = aEr_{-\Theta}$
15	0.25	-0.365955
	0.5	-1.32964
	1.0	-3.14373
	2.0	-5.33993
	4.0	-5.87906
30	0.25	-0.422952
	0.5	-1.40656
	1.0	-3.17270
	2.0	-5.37712
	4.0	-7.53184
45	0.25	-0.537534
	0.5	-1.60990
	1.0	-3.44683
	2.0	-5.78792
	4.0	-8.84485
60	0.25	-0.755183
	0.5	-2.02251
	1.0	-4.06754
	2.0	-6.73290
	4.0	-10.7921
75	0.25	-1.26172
	0.5	-2.89676
	1.0	-5.25712
	2.0	-8.43630
	4.0	-13.9820

Table 10. Nondimensional Flexibilities ($bEr_{+\Theta}^2 = \alpha Er_{-\Theta}^2$) for Conical Sections with $(\frac{t}{r}) = .0125$, Varying Θ , and Varying $(\frac{l}{r})$ Ratio.

Θ	$\frac{l}{r}$	$bEr_{+\Theta}^2 = \alpha Er_{-\Theta}^2$
15	0.25	5.14583
	0.5	11.5685
	1.0	27.3150
	2.0	66.8893
	4.0	163.402
30	0.25	11.1020
	0.5	22.9152
	1.0	47.6992
	2.0	99.7620
	4.0	207.418
45	0.25	22.1019
	0.5	43.7465
	1.0	86.0667
	2.0	169.148
	4.0	332.995
60	0.25	50.8352
	0.5	97.8549
	1.0	187.314
	2.0	360.488
	4.0	700.807
75	0.25	192.320
	0.5	364.804
	1.0	697.226
	2.0	1353.41
	4.0	2658.37

Table 11. Nondimensional Flexibilities ($bEr_{+\Theta}^2 = \alpha Er_{-\Theta}^2$) for Conical Sections with $((\frac{t}{r}) = .025$, Varying Θ , and Varying $(\frac{l}{r})$ Ratio.

Θ	$\frac{l}{r}$	$bEr_{+\Theta}^2 = \alpha Er_{-\Theta}^2$
15	0.25	2.50129
	0.5	5.70966
	1.0	13.5461
	2.0	33.2760
	4.0	81.5277
30	0.25	5.39105
	0.5	11.3066
	1.0	23.6282
	2.0	49.5516
	4.0	103.339
45	0.25	10.7217
	0.5	21.5463
	1.0	42.5389
	2.0	83.8238
	4.0	165.600
60	0.25	24.5792
	0.5	47.9520
	1.0	92.0964
	2.0	177.794
	4.0	347.376
75	0.25	91.5806
	0.5	175.474
	1.0	336.552
	2.0	657.308
	4.0	1305.33

Table 12. Nondimensional Flexibilities ($bEr_{+\Theta}^2 = \alpha Er_{-\Theta}^2$) for Conical Sections with $((\frac{l}{r}) = .05$, Varying Θ , and Varying $(\frac{l}{r})$ Ratio.

Θ	$\frac{l}{r}$	$bEr_{+\Theta}^2 = \alpha Er_{-\Theta}^2$
15	0.25	1.13353
	0.5	2.76602
	1.0	6.66355
	2.0	16.4650
	4.0	40.5201
30	0.25	2.42769
	0.5	5.46264
	1.0	11.5807
	2.0	24.4094
	4.0	51.1296
45	0.25	4.81959
	0.5	10.3677
	1.0	20.7318
	2.0	41.0336
	4.0	81.4468
60	0.25	10.9988
	0.5	22.8371
	1.0	44.3273
	2.0	85.9235
	4.0	168.983
75	0.25	39.9720
	0.5	80.3875
	1.0	155.317
	2.0	304.678
	4.0	614.785

Table 13. Nondimensional Flexibilities ($bEr_{+\Theta}^2 = \alpha Er_{-\Theta}^2$) for Conical Sections with $((\frac{l}{r}) = .1$, Varying Θ , and Varying $(\frac{l}{r})$ Ratio.

Θ	$\frac{l}{r}$	$bEr_{+\Theta}^2 = \alpha Er_{-\Theta}^2$
15	0.25	0.407040
	0.5	1.26040
	1.0	3.21266
	2.0	8.05920
	4.0	19.9812
30	0.25	0.851053
	0.5	2.45556
	1.0	5.52912
	2.0	11.8138
	4.0	24.9129
45	0.25	1.69223
	0.5	4.61720
	1.0	9.77256
	2.0	19.5604
	4.0	39.0475
60	0.25	3.86121
	0.5	9.98283
	1.0	20.3417
	2.0	39.7651
	4.0	78.6287
75	0.25	13.5442
	0.5	32.7980
	1.0	65.4812
	2.0	128.894
	4.0	262.191

Table 14. Nondimensional Flexibilities ($bEr_{+\Theta}^2 = \alpha Er_{-\Theta}^2$) for Conical Sections with $(\frac{t}{r}) = .2$, Varying Θ , and Varying $(\frac{l}{r})$ Ratio.

Θ	$\frac{l}{r}$	$bEr_{+\Theta}^2 = \alpha Er_{-\Theta}^2$
15	0.25	0.0820812
	0.5	0.471078
	1.0	1.46323
	2.0	3.85164
	4.0	9.7002
30	0.25	0.156430
	0.5	0.871381
	1.0	2.44760
	2.0	5.49738
	4.0	11.7580
45	0.25	0.333677
	0.5	1.60694
	1.0	4.20855
	2.0	8.80371
	4.0	17.7554
60	0.25	0.824413
	0.5	3.38390
	1.0	8.33288
	2.0	16.8576
	4.0	33.5125
75	0.25	2.92445
	0.5	10.1182
	1.0	23.3119
	2.0	46.7298
	4.0	94.4523

Table 15. Nondimensional Flexibilities ($\alpha E r_{+\Theta}^2 = b E r_{-\Theta}^2$) for Conical Sections with $((\frac{l}{r}) = .0125$, Varying Θ , and Varying $(\frac{l}{r})$ Ratio.

Θ	$\frac{l}{r}$	$\alpha E r_{+\Theta}^2 = b E r_{-\Theta}^2$
15	0.25	-3.35914
	0.5	-4.81764
	1.0	-4.03825
	2.0	4.52193
	4.0	26.9966
30	0.25	-7.95148
	0.5	-12.0540
	1.0	-14.7028
	2.0	-12.7436
	4.0	-5.68461
45	0.25	-15.0169
	0.5	-21.5003
	1.0	-25.5206
	2.0	-25.0119
	4.0	-21.3568
60	0.25	-29.8036
	0.5	-38.6405
	1.0	-42.4161
	2.0	-41.2734
	4.0	-38.2425
75	0.25	-77.3563
	0.5	-85.9213
	1.0	-85.6796
	2.0	-82.0337
	4.0	-78.6086

Table 16. Nondimensional Flexibilities ($\alpha E r_{+\Theta}^2 = b E r_{-\Theta}^2$) for Conical Sections with $((\frac{l}{r}) = .025$, Varying Θ , and Varying $(\frac{l}{r})$ Ratio.

Θ	$\frac{l}{r}$	$\alpha E r_{+\Theta}^2 = b E r_{-\Theta}^2$
15	0.25	-1.62549
	0.5	-2.38807
	1.0	-1.99987
	2.0	2.27569
	4.0	13.5125
30	0.25	-3.85713
	0.5	-5.96493
	1.0	-7.29022
	2.0	-6.31742
	4.0	-2.80081
45	0.25	-7.29076
	0.5	-10.6205
	1.0	-12.6356
	2.0	-12.3952
	4.0	-10.5965
60	0.25	-14.4526
	0.5	-19.0011
	1.0	-20.9050
	2.0	-20.3661
	4.0	-18.9281
75	0.25	-37.0794
	0.5	-41.5127
	1.0	-41.4442
	2.0	-39.7961
	4.0	-38.5058

Table 17. Nondimensional Flexibilities ($\alpha E r_{+\Theta}^2 = b E r_{-\Theta}^2$) for Conical Sections with $((\frac{l}{r}) = .05$, Varying Θ , and Varying $(\frac{l}{r})$ Ratio.

Θ	$\frac{l}{r}$	$\alpha E r_{+\Theta}^2 = b E r_{-\Theta}^2$
15	0.25	-0.707560
	0.5	-1.14735
	1.0	-0.963623
	2.0	1.17096
	4.0	6.78615
30	0.25	-1.70794
	0.5	-2.87817
	1.0	-3.56147
	2.0	-3.08032
	4.0	-1.33143
45	0.25	-3.25015
	0.5	-5.11992
	1.0	-6.15827
	2.0	-6.04743
	4.0	-5.16653
60	0.25	-6.44910
	0.5	-9.09183
	1.0	-10.0791
	2.0	-9.82485
	4.0	-9.15410
75	0.25	-16.2538
	0.5	-19.1525
	1.0	-19.1269
	2.0	-18.3326
	4.0	-17.9714

Table 18. Nondimensional Flexibilities ($\alpha E r_{+\Theta}^2 = b E r_{-\Theta}^2$) for Conical Sections with $((\frac{t}{r}) = .1$, Varying Θ , and Varying $(\frac{l}{r})$ Ratio.

Θ	$\frac{l}{r}$	$\alpha E r_{+\Theta}^2 = b E r_{-\Theta}^2$
15	0.25	-0.207751
	0.5	-0.479667
	1.0	-0.430284
	2.0	0.635722
	4.0	3.44023
30	0.25	-0.551703
	0.5	-1.25374
	1.0	-1.67476
	2.0	-1.44016
	4.0	-0.571204
45	0.25	-1.09435
	0.5	-2.24837
	1.0	-2.88920
	2.0	-2.84164
	4.0	-2.40827
60	0.25	-2.21721
	0.5	-3.96207
	1.0	-4.62488
	2.0	-4.50137
	4.0	-4.17636
75	0.25	-5.47422
	0.5	-7.86734
	1.0	-8.03047
	2.0	-7.59648
	4.0	-7.44044

Table 19. Nondimensional Flexibilities ($\alpha Er_{+\Theta}^2 = bEr_{-\Theta}^2$) for Conical Sections with $((\frac{t}{r}) = .2$, Varying Θ , and Varying $(\frac{l}{r})$ Ratio.

Θ	$\frac{l}{r}$	$\alpha Er_{+\Theta}^2 = bEr_{-\Theta}^2$
15	0.25	0.0071072
	0.5	-0.107828
	1.0	-0.133075
	2.0	0.381569
	4.0	1.78054
30	0.25	-0.0517861
	0.5	-0.375835
	1.0	-0.687045
	2.0	-0.605333
	4.0	-0.174387
45	0.25	-0.168031
	0.5	-0.720708
	1.0	-1.20388
	2.0	-1.22537
	4.0	-1.00963
60	0.25	-0.426835
	0.5	-1.29113
	1.0	-1.87001
	2.0	-1.85203
	4.0	-1.68201
75	0.25	-1.13910
	0.5	-2.39961
	1.0	-2.83098
	2.0	-2.61920
	4.0	-2.47247

Table 20. Nondimensional Flexibilities ($\beta E r^3$) for Conical Sections with $((\frac{t}{r}) = .0125$, Varying Θ , and Varying $\frac{l}{r}$ Ratio.

Θ	$\frac{l}{r}$	$\beta E r^3_{+\Theta} = \beta E r^3_{-\Theta}$
15	0.25	7.14700
	0.5	13.5022
	1.0	23.2778
	2.0	35.7056
	4.0	47.5998
30	0.25	12.6024
	0.5	21.7229
	1.0	32.9972
	2.0	43.5092
	4.0	50.4334
45	0.25	28.3401
	0.5	44.4925
	1.0	60.5462
	2.0	72.0681
	4.0	77.9095
60	0.25	84.1246
	0.5	118.426
	1.0	144.894
	2.0	159.603
	4.0	165.637
75	0.25	459.849
	0.5	557.759
	1.0	611.539
	2.0	635.678
	4.0	644.932

Table 21. Nondimensional Flexibilities (βEr^3) for Conical Sections with $((\frac{l}{r}) = .025$, Varying Θ , and Varying $\frac{l}{r}$ Ratio.

Θ	$\frac{l}{r}$	$\beta Er^3_{+\Theta} = \beta Er^3_{-\Theta}$
15	0.25	3.50333
	0.5	6.64343
	1.0	11.5468
	2.0	17.7759
	4.0	23.7601
30	0.25	6.13577
	0.5	10.6836
	1.0	16.3384
	2.0	21.6171
	4.0	25.1346
45	0.25	13.7237
	0.5	21.8517
	1.0	29.9033
	2.0	35.7143
	4.0	38.7508
60	0.25	40.5056
	0.5	57.9004
	1.0	71.1896
	2.0	78.7122
	4.0	82.1097
75	0.25	218.002
	0.5	267.920
	1.0	295.104
	2.0	308.752
	4.0	316.701

Table 22. Nondimensional Flexibilities ($\beta E r^3$) for Conical Sections with $((\frac{t}{r}) = .05$, Varying Θ , and Varying $\frac{l}{r}$ Ratio.

Θ	$\frac{l}{r}$	$\beta E r_{+\Theta}^3 = \beta E r_{-\Theta}^3$
15	0.25	1.70392
	0.5	3.23745
	1.0	5.70020
	2.0	8.81801
	4.0	11.8266
30	0.25	2.87902
	0.5	5.16903
	1.0	8.01938
	2.0	10.6646
	4.0	12.4495
45	0.25	6.27776
	0.5	10.4957
	1.0	14.5735
	2.0	17.4931
	4.0	19.0701
60	0.25	18.1984
	0.5	27.4899
	1.0	34.2474
	2.0	38.0483
	4.0	39.9561
75	0.25	94.8717
	0.5	122.469
	1.0	136.188
	2.0	143.171
	4.0	149.201

Table 23. Nondimensional Flexibilities ($\beta E r^3$) for Conical Sections with $((\frac{t}{r}) = .1$, Varying Θ , and Varying $\frac{l}{r}$ Ratio.

Θ	$\frac{l}{r}$	$\beta E r^3_{+\Theta} = \beta E r^3_{-\Theta}$
15	0.25	0.797174
	0.5	1.56152
	1.0	2.78250
	2.0	4.34747
	4.0	5.85535
30	0.25	1.19742
	0.5	2.40369
	1.0	3.85445
	2.0	5.18680
	4.0	6.08543
45	0.25	2.39152
	0.5	4.73766
	1.0	6.88336
	2.0	8.35940
	4.0	9.15980
60	0.25	6.57586
	0.5	12.0412
	1.0	15.7164
	2.0	17.6314
	4.0	18.6126
75	0.25	32.2798
	0.5	49.8608
	1.0	57.4500
	2.0	60.6482
	4.0	63.6868

Table 24. Nondimensional Flexibilities ($\beta E r^3$) for Conical Sections with $((\frac{l}{r}) = .2$, Varying Θ , and Varying $\frac{l}{r}$ Ratio.

Θ	$\frac{l}{r}$	$\beta E r^3_{+\Theta} = \beta E r^3_{-\Theta}$
15	0.25	0.356757
	0.5	0.726522
	1.0	1.33021
	2.0	2.11661
	4.0	2.87020
30	0.25	0.418580
	0.5	0.991108
	1.0	1.76059
	2.0	2.44602
	4.0	2.89589
45	0.25	0.662584
	0.5	1.77247
	1.0	3.00468
	2.0	3.78917
	4.0	4.18643
60	0.25	1.59028
	0.5	4.18545
	1.0	6.46271
	2.0	7.50258
	4.0	7.95741
75	0.25	7.14131
	0.5	15.4369
	1.0	20.4806
	2.0	22.0550
	4.0	22.9947

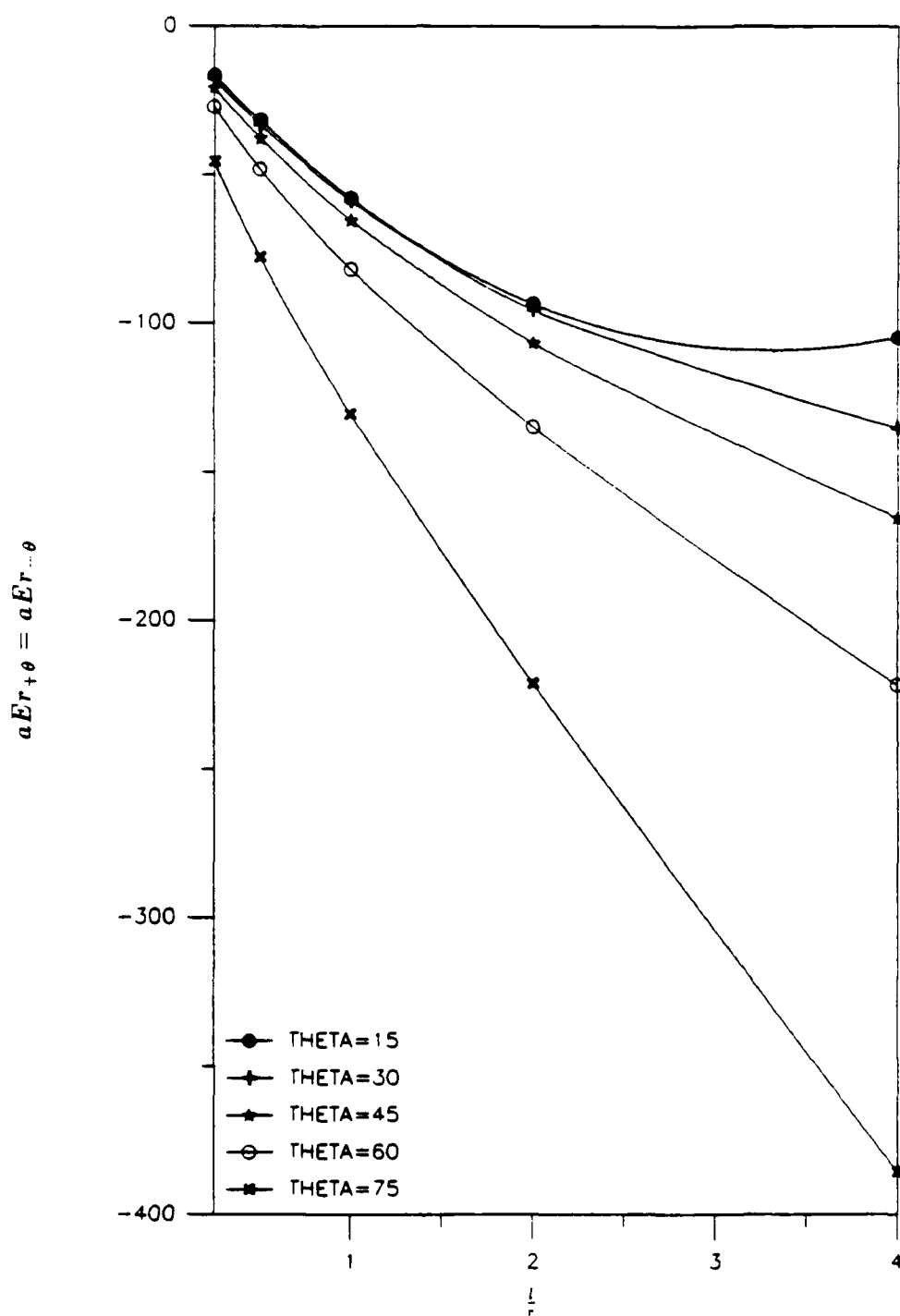


Fig. 28. Nondimensional flexibility plots (aEr) for conical sections with $(\frac{l}{r}) = 0.0125$, varying $θ$ and varying $(\frac{l}{r})$ ratio.

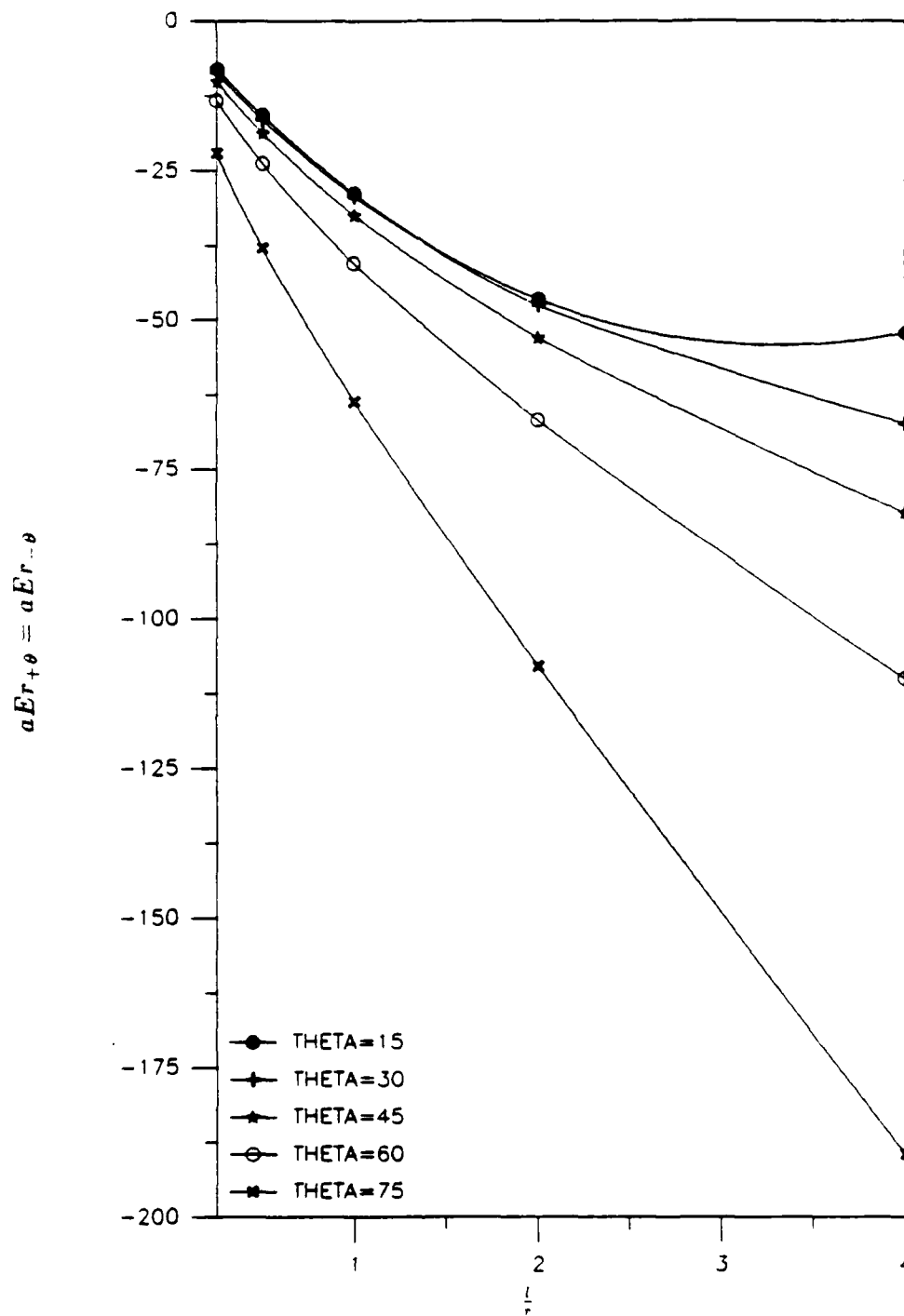


Fig. 29. Nondimensional flexibility plots (aEr) for conical sections with $(\frac{l}{r}) = 0.025$, varying θ and varying $(\frac{l}{r})$ ratio.

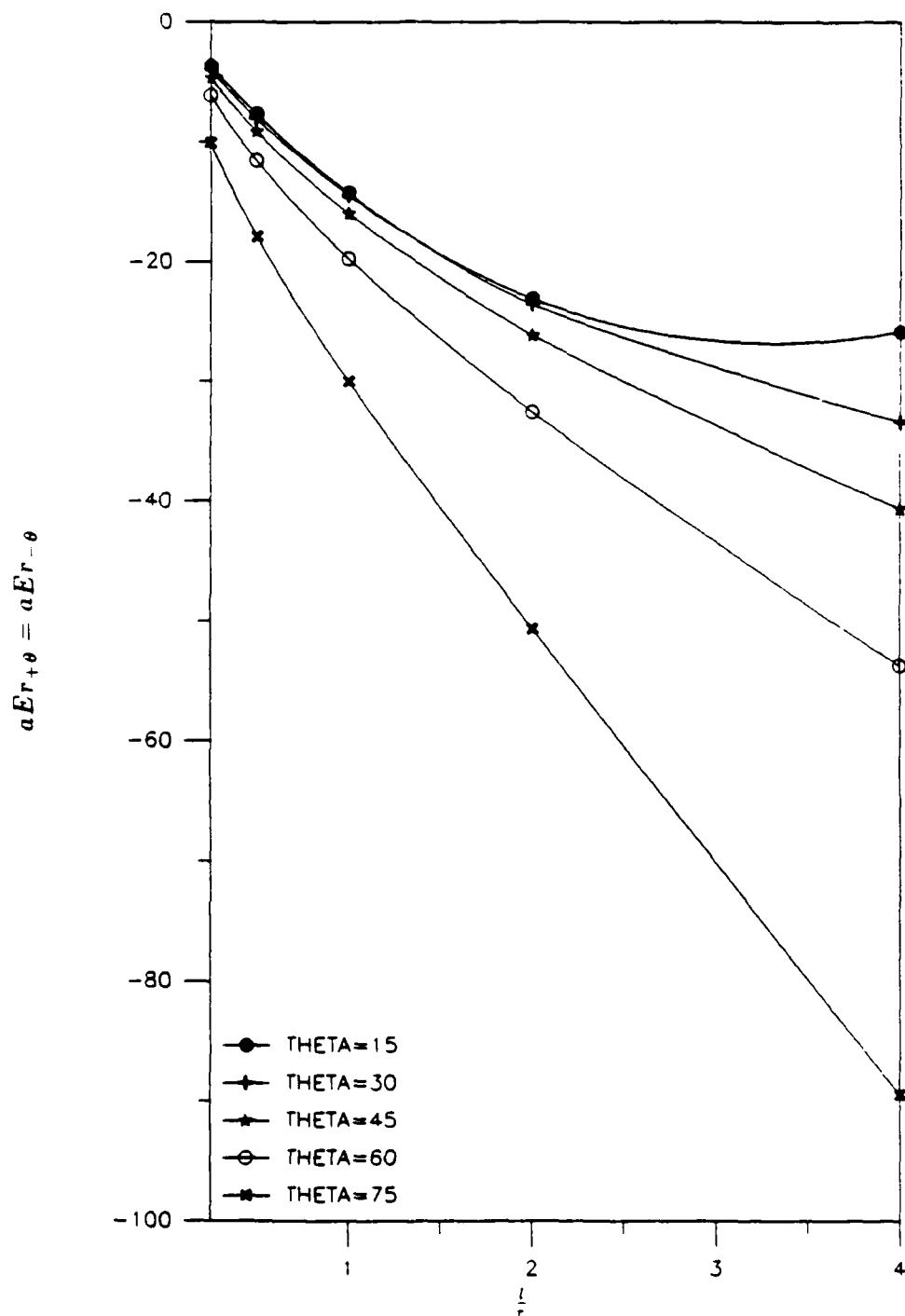


Fig. 30. Nondimensional flexibility plots (aEr) for conical sections with $(\frac{l}{r}) = 0.05$, varying θ and varying $(\frac{l}{r})$ ratio.

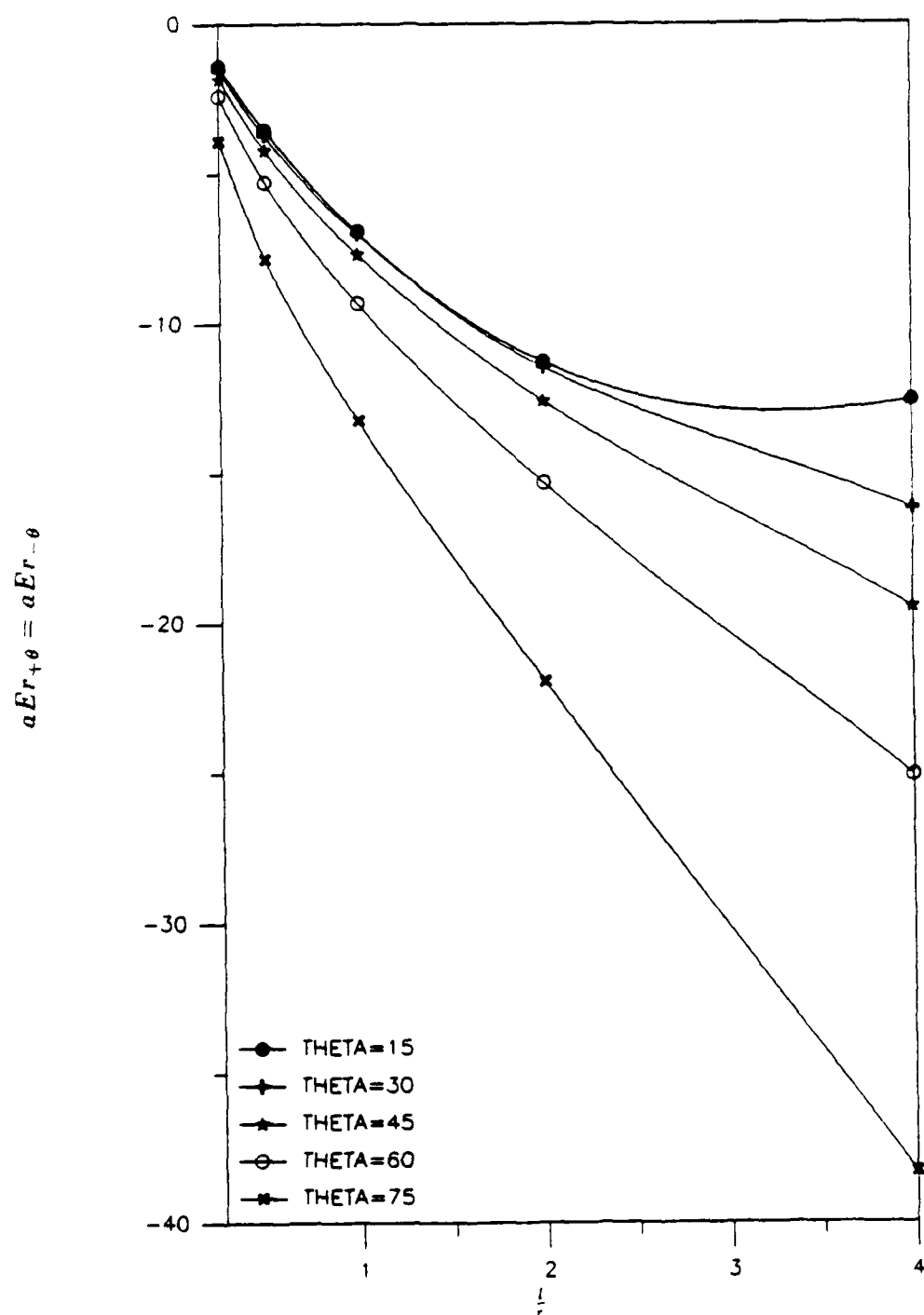


Fig. 31. Nondimensional flexibility plots (aEr) for conical sections with $(\frac{t}{r}) = 0.1$, varying θ and varying $(\frac{l}{r})$ ratio.

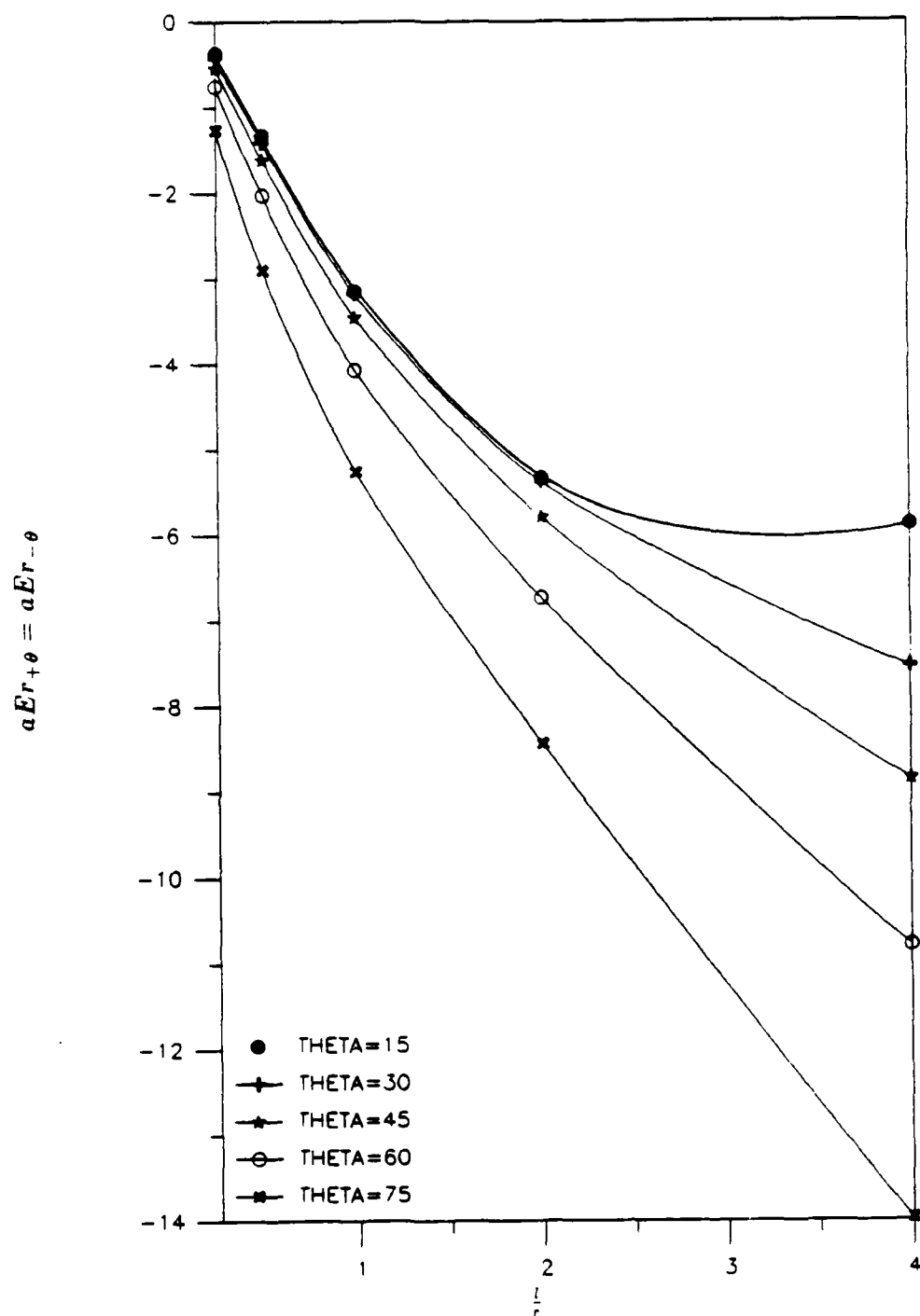


Fig. 32. Nondimensional flexibility plots (aEr) for conical sections with $(\frac{t}{r}) = 0.2$, varying θ and varying $(\frac{l}{r})$ ratio.

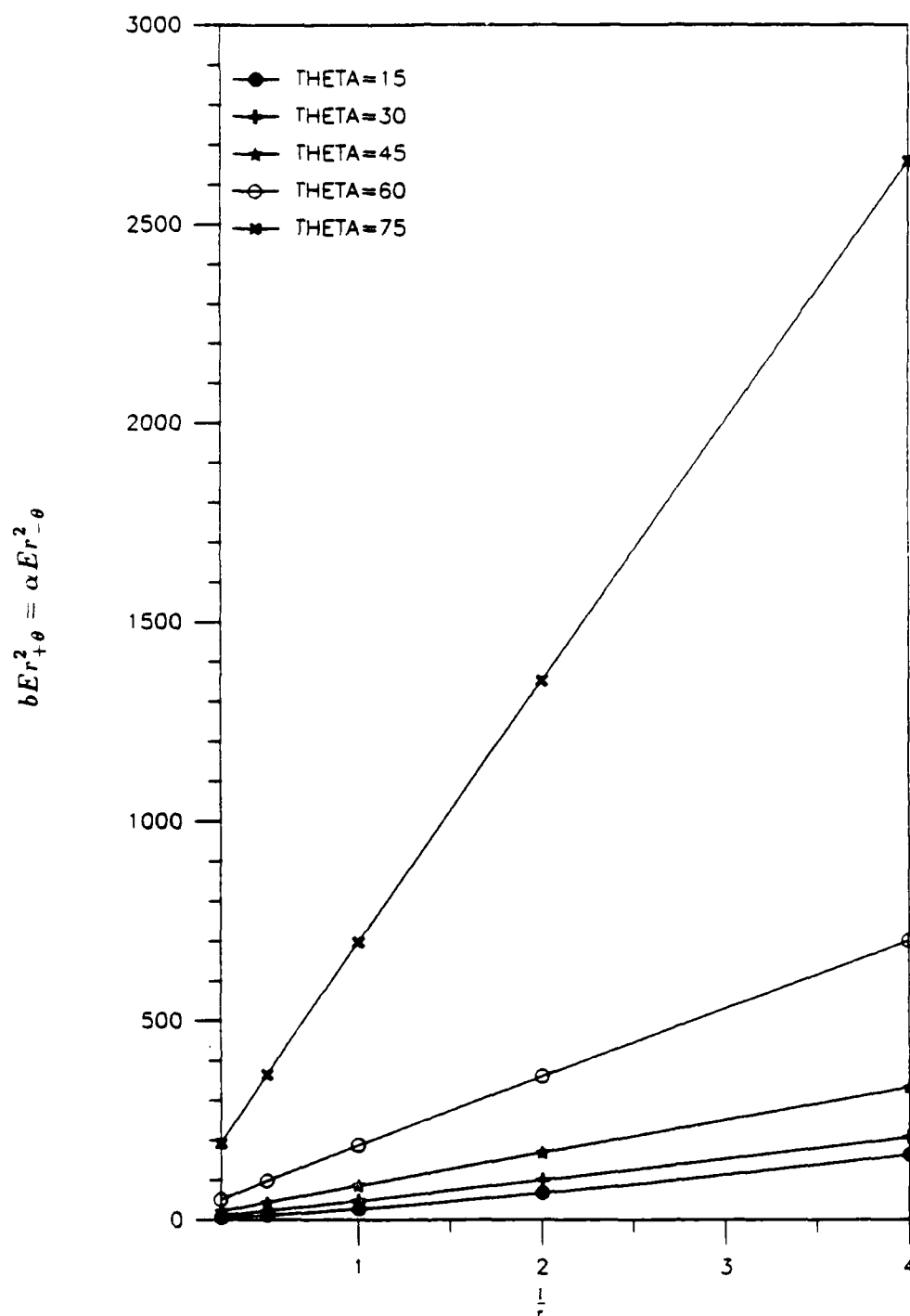


Fig. 33. Nondimensional flexibility plots ($bEr_{+θ}^2 = αEr_{-θ}^2$) for conical sections with $(\frac{t}{r}) = 0.0125$, varying $θ$ and varying $(\frac{1}{r})$ ratio.

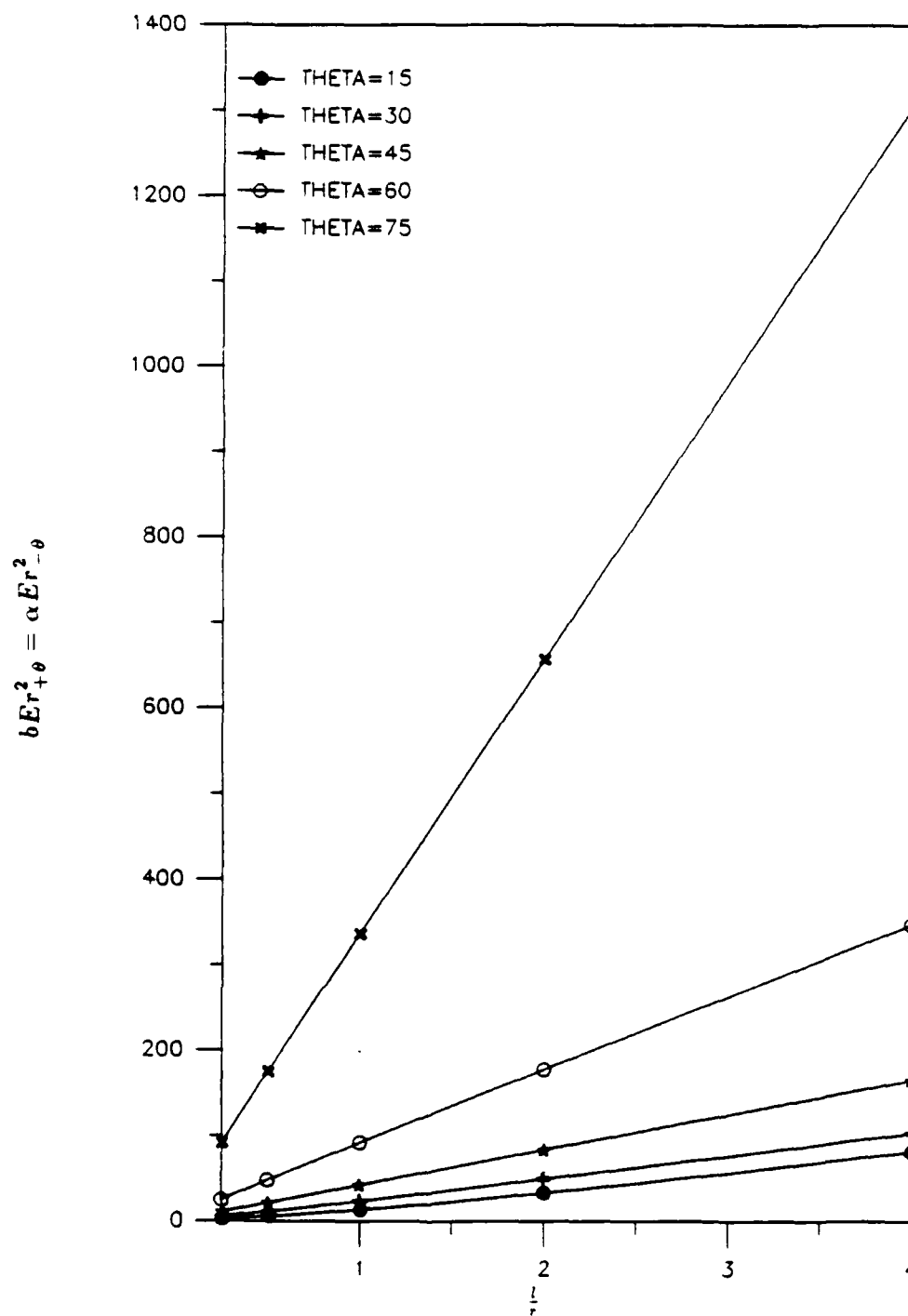


Fig. 34. Nondimensional flexibility plots ($bEr_{+θ}^2 = αEr_{-θ}^2$) for conical sections with $(t/r) = 0.025$, varying $θ$ and varying (l/r) ratio.

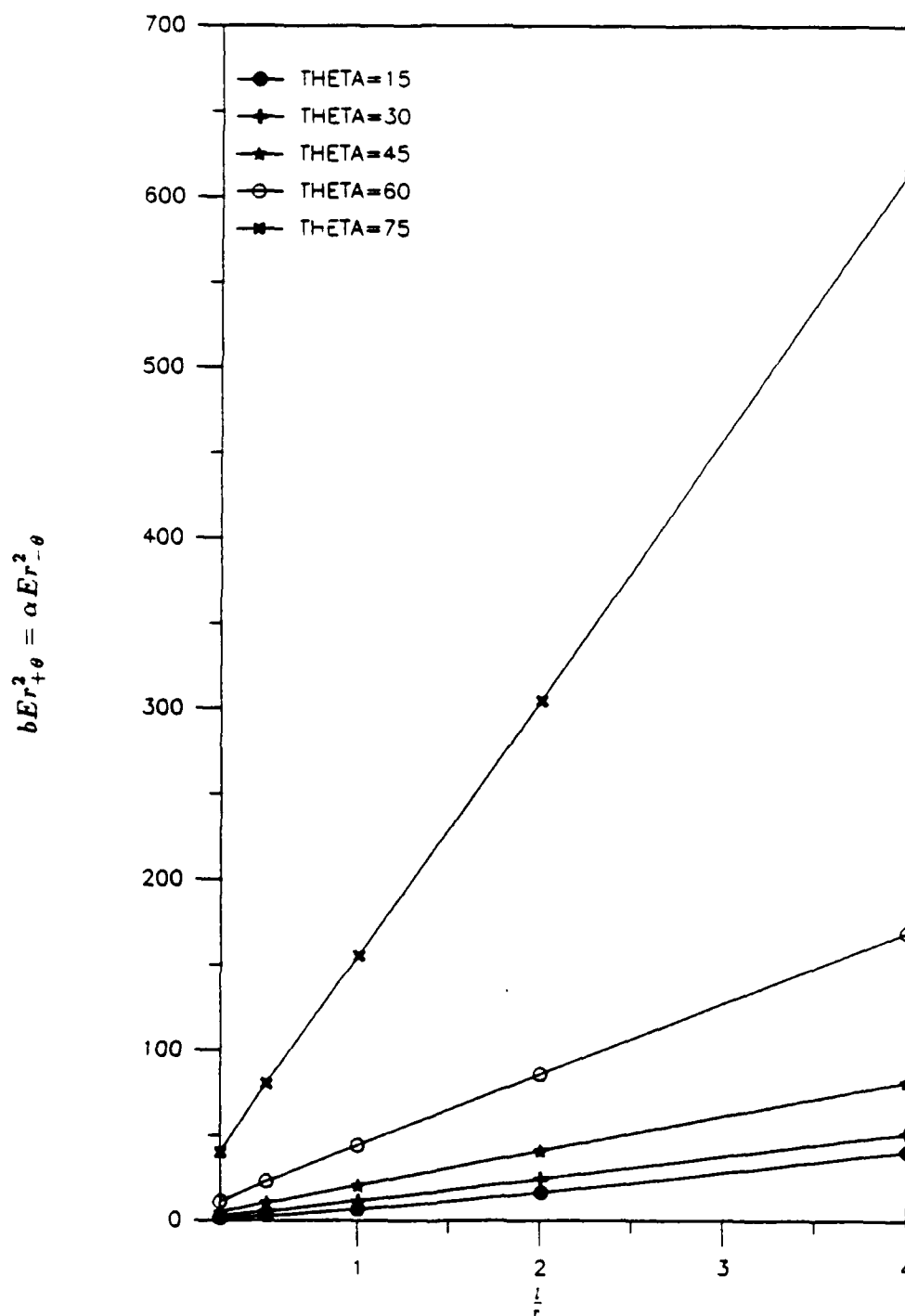


Fig. 35. Nondimensional flexibility plots ($bEr_{+θ}^2 = αEr_{-θ}^2$) for conical sections with $(\frac{l}{r}) = 0.05$, varying $θ$ and varying $(\frac{l}{r})$ ratio.

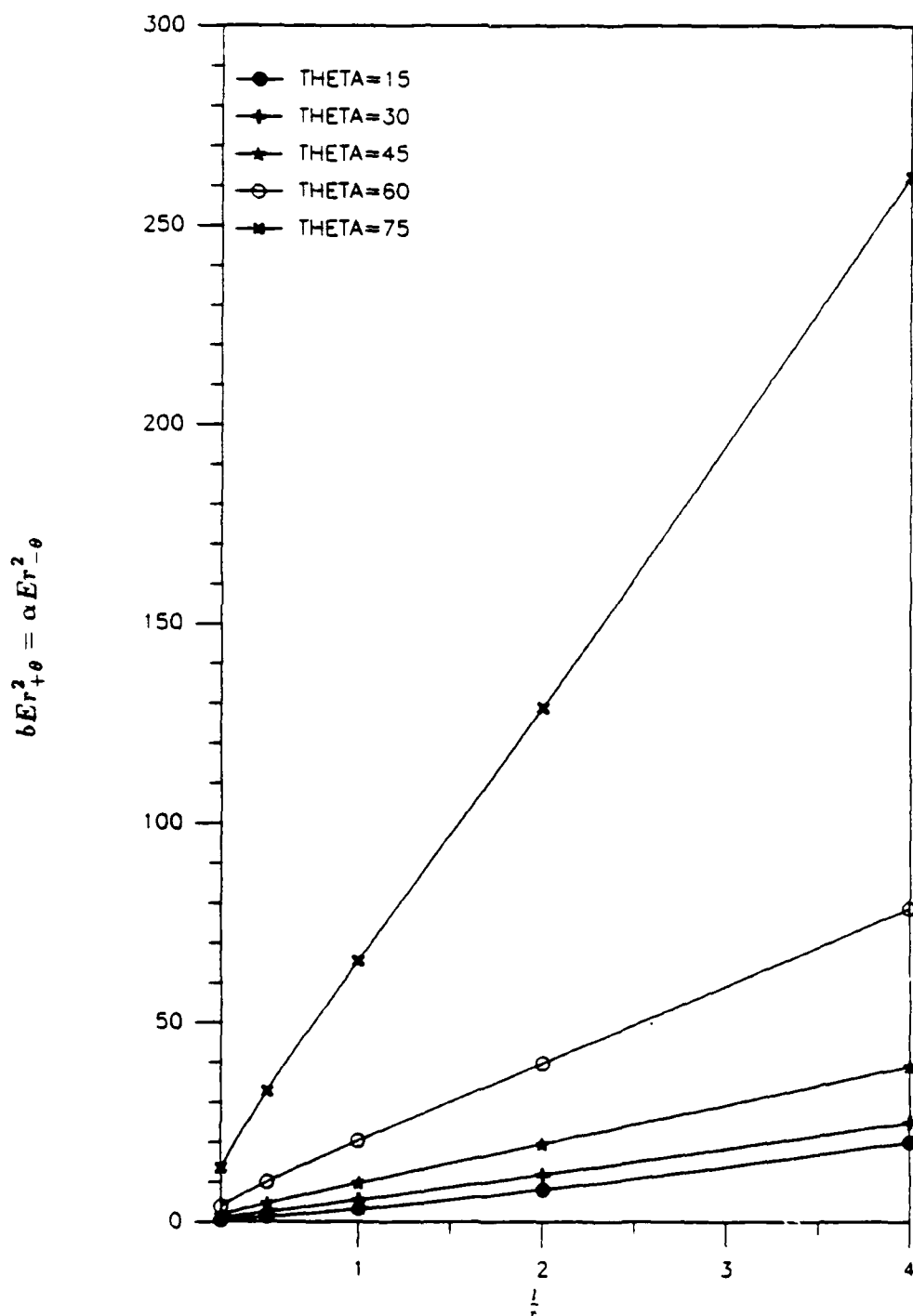


Fig. 36. Nondimensional flexibility plots ($bEr_{+θ}^2 = αEr_{-θ}^2$) for conical sections with $(\frac{l}{r}) = 0.1$, varying $θ$ and varying $(\frac{l}{r})$ ratio.

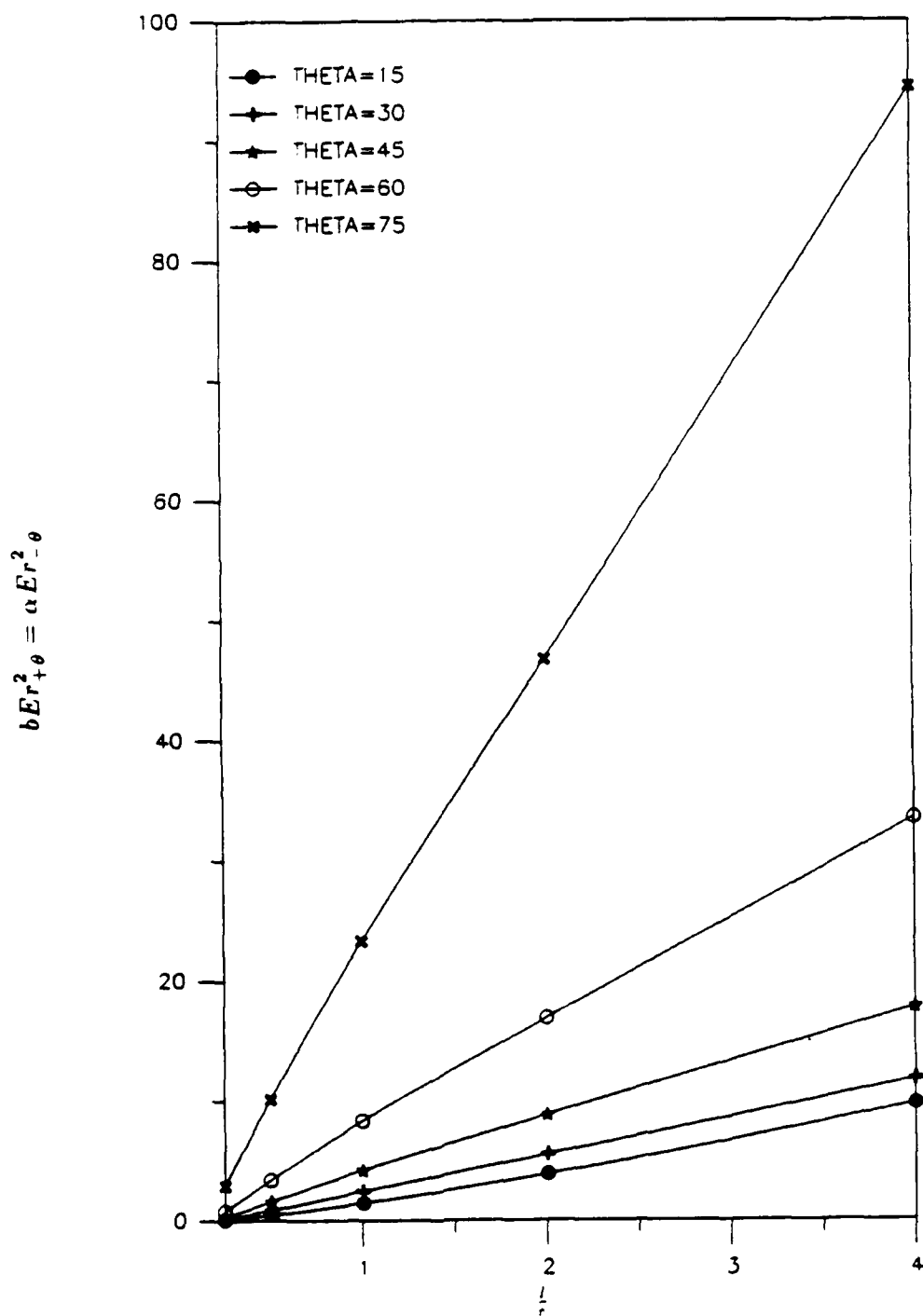


Fig. 37. Nondimensional flexibility plots ($bEr_{+θ}^2 = αEr_{-θ}^2$) for conical sections with $(\frac{l}{r}) = 0.2$, varying $θ$ and varying $(\frac{l}{r})$ ratio.

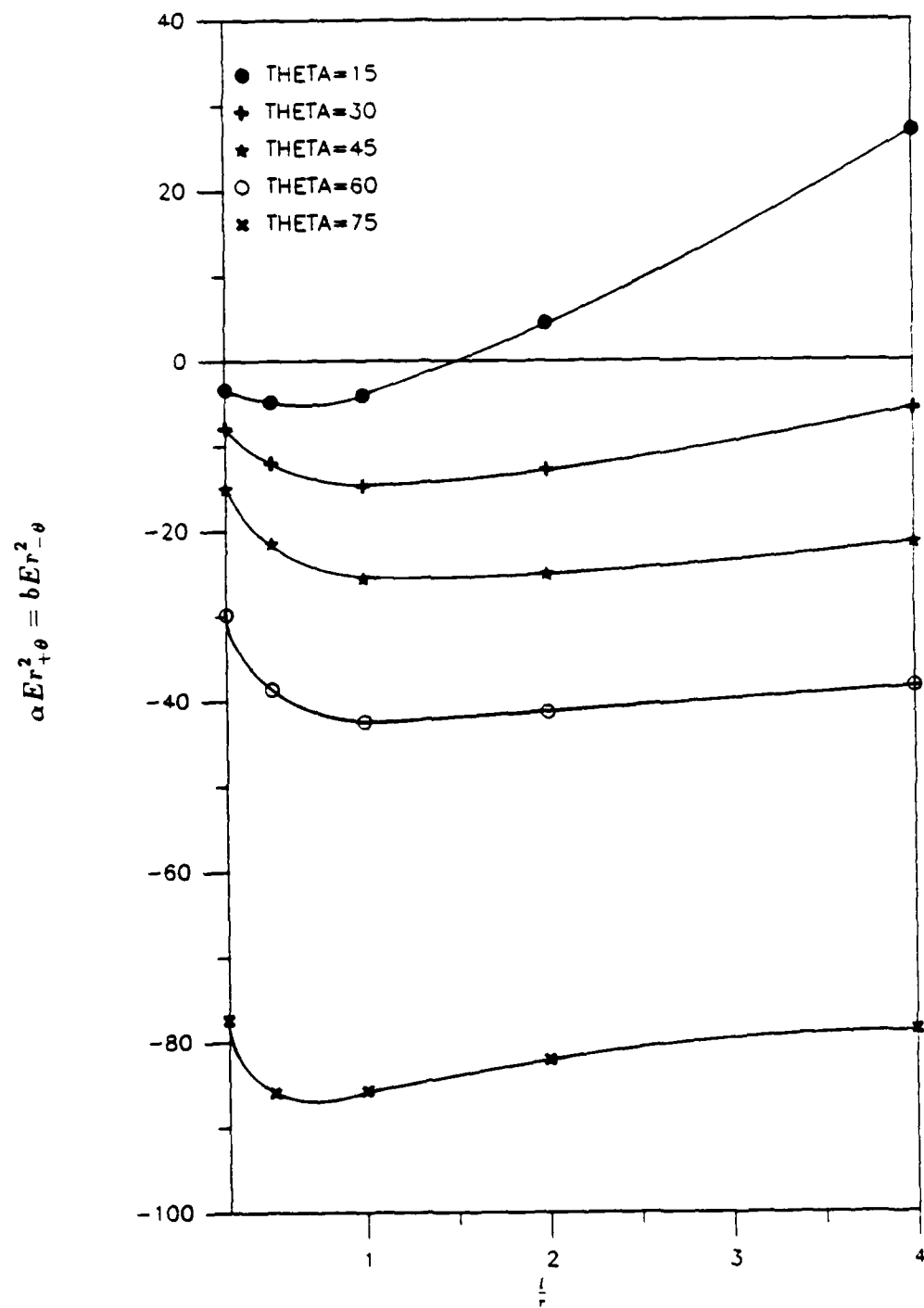


Fig. 38. Nondimensional flexibility plots ($\alpha Er_{+ \theta}^2 = b Er_{- \theta}^2$) for conical sections with $(\frac{l}{r}) = 0.0125$, varying θ and varying $(\frac{l}{r})$ ratio.

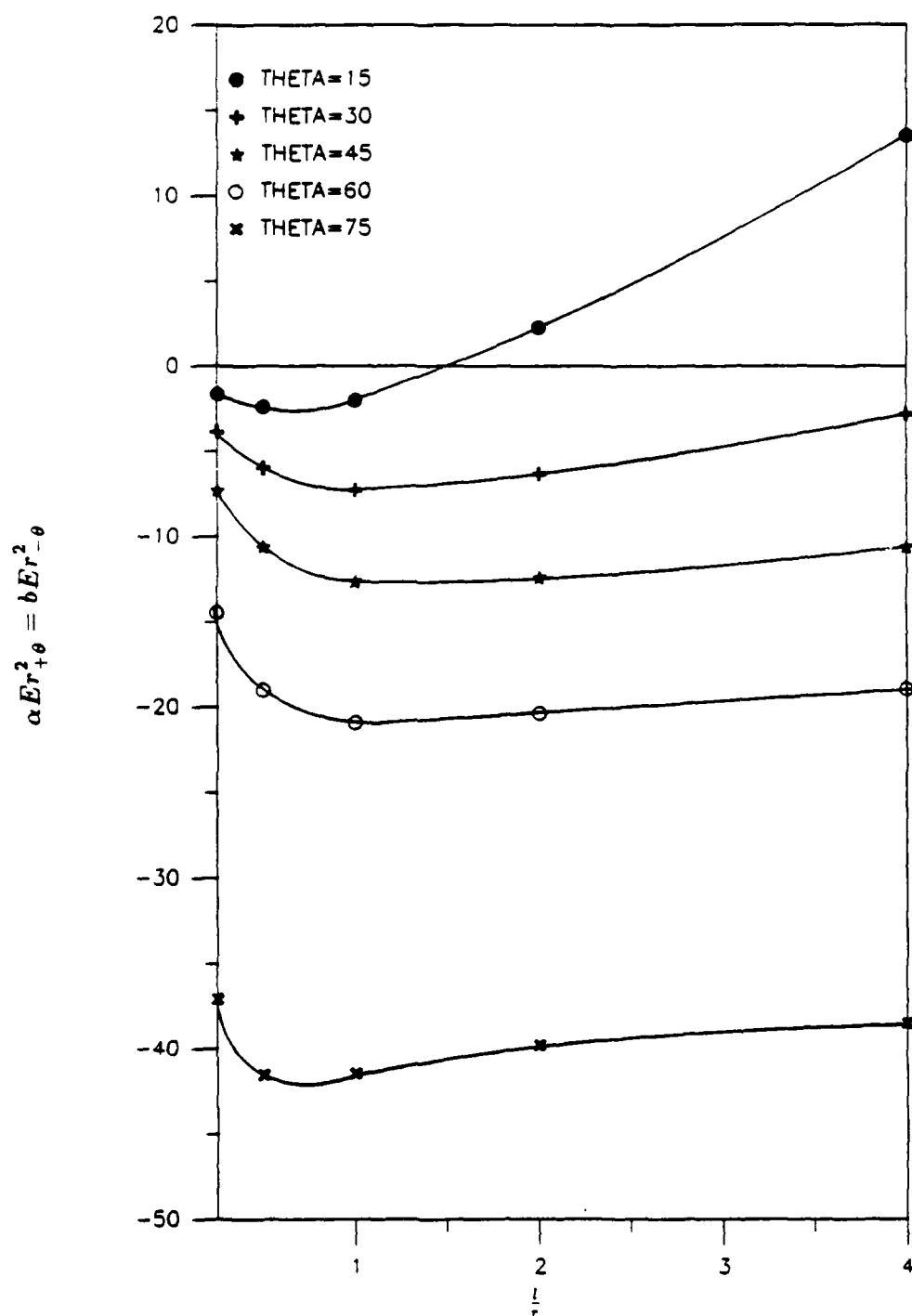


Fig. 39. Nondimensional flexibility plots ($\alpha Er_{+ \theta}^2 = b Er_{- \theta}^2$) for conical sections with $(\frac{l}{r}) = 0.025$, varying θ and varying $(\frac{l}{r})$ ratio.

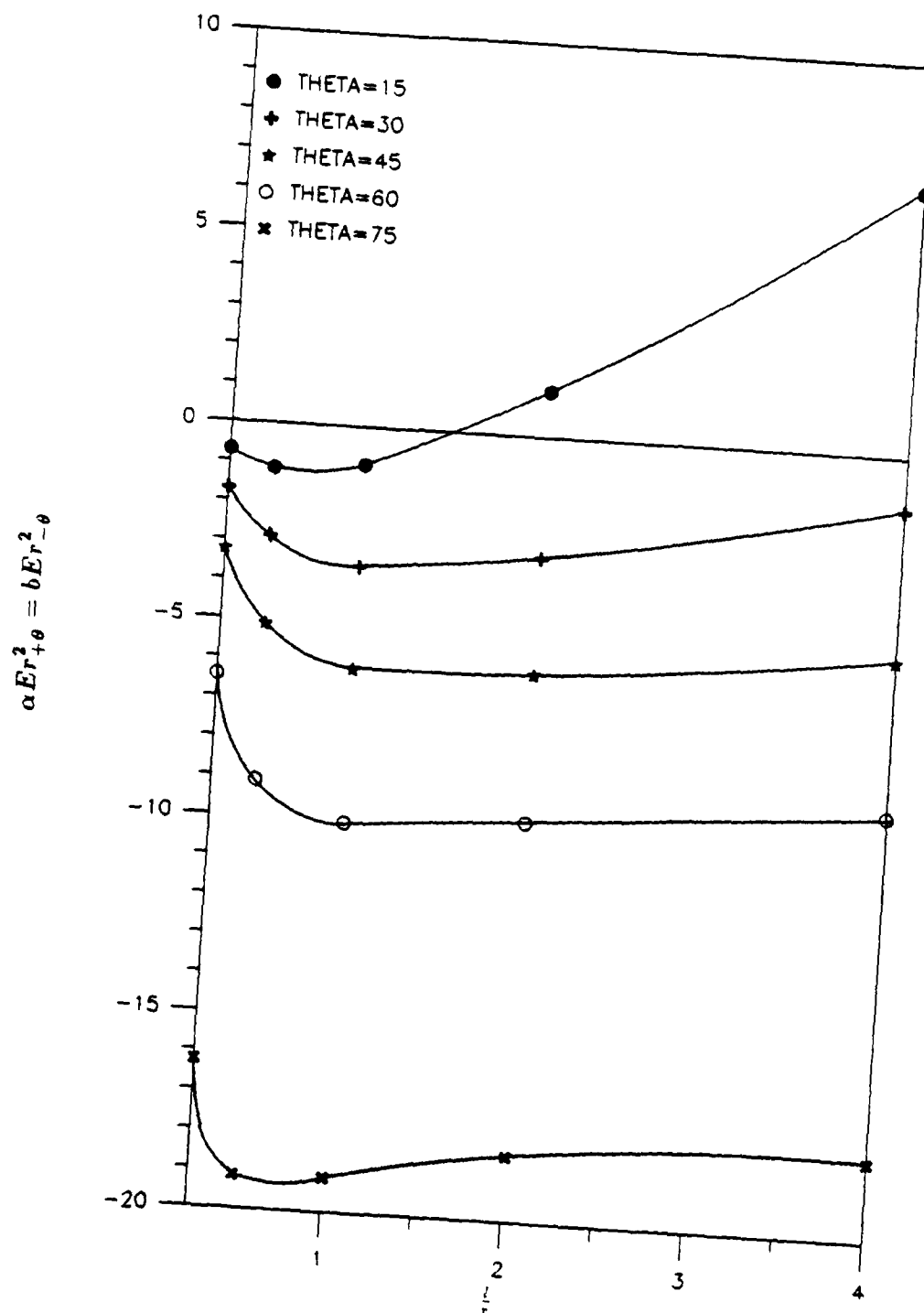


Fig. 40. Nondimensional flexibility plots ($\alpha Er_{+ \theta}^2 = b Er_{- \theta}^2$) for conical sections with $(\frac{l}{r}) = 0.05$, varying θ and varying $(\frac{l}{r})$ ratio.

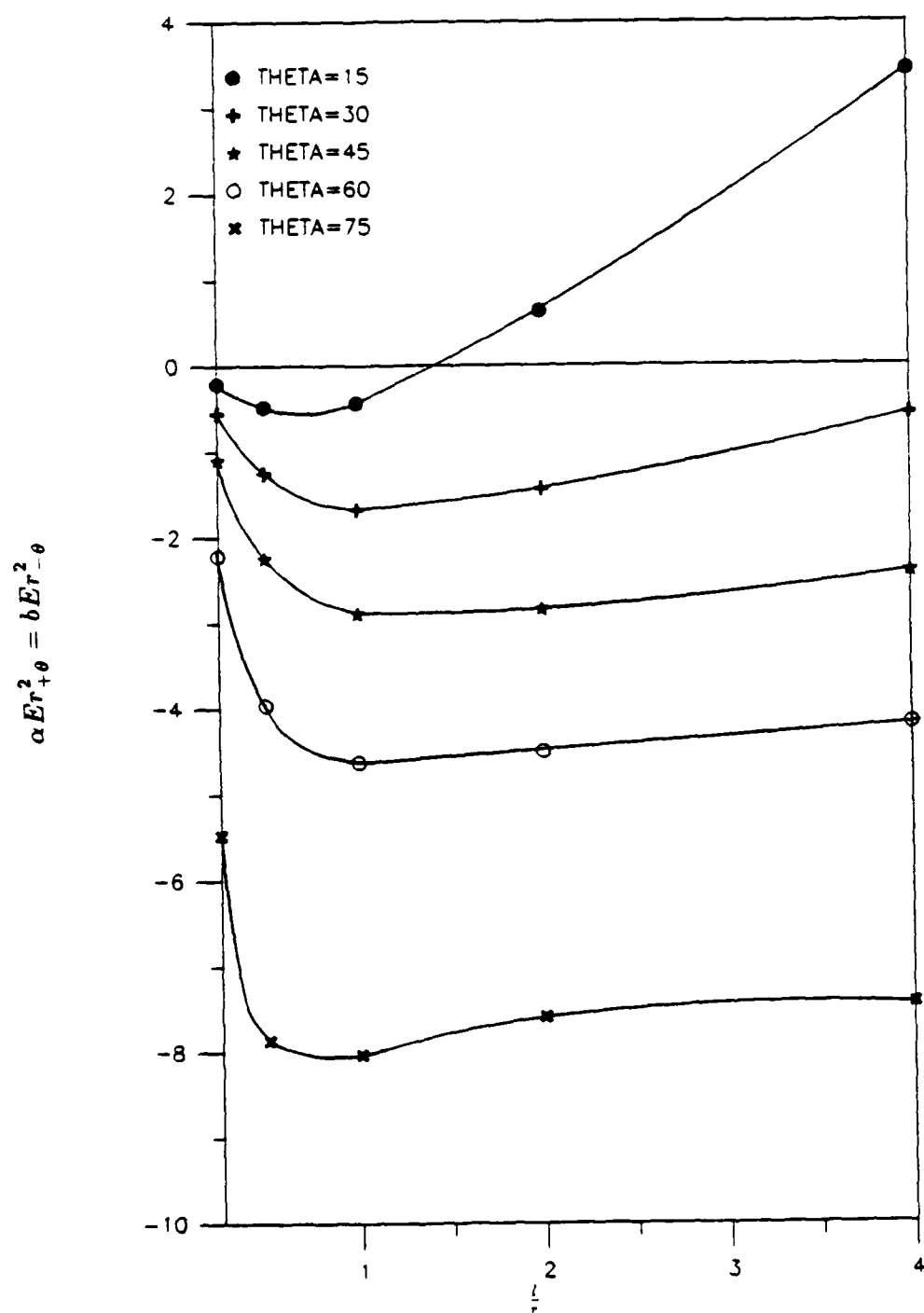


Fig. 41. Nondimensional flexibility plots ($\alpha Er_{+\theta}^2 = b Er_{-\theta}^2$) for conical sections with $(\frac{l}{r}) = 0.1$, varying θ and varying $(\frac{l}{r})$ ratio.

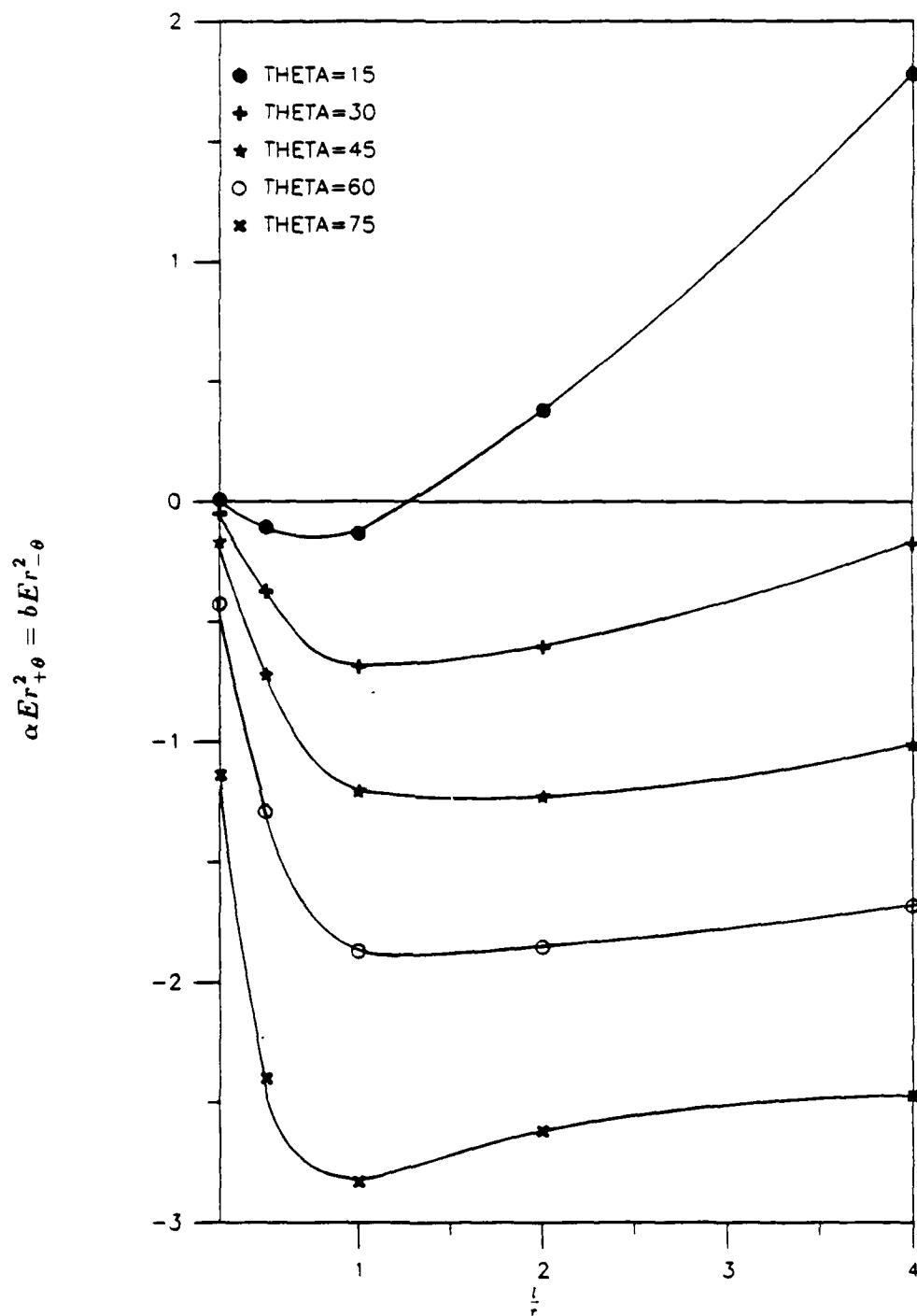


Fig. 42. Nondimensional flexibility plots ($\alpha Er_{+\theta}^2 = b Er_{-\theta}^2$) for conical sections with $(\frac{l}{r}) = 0.2$, varying θ and varying $(\frac{l}{r})$ ratio.

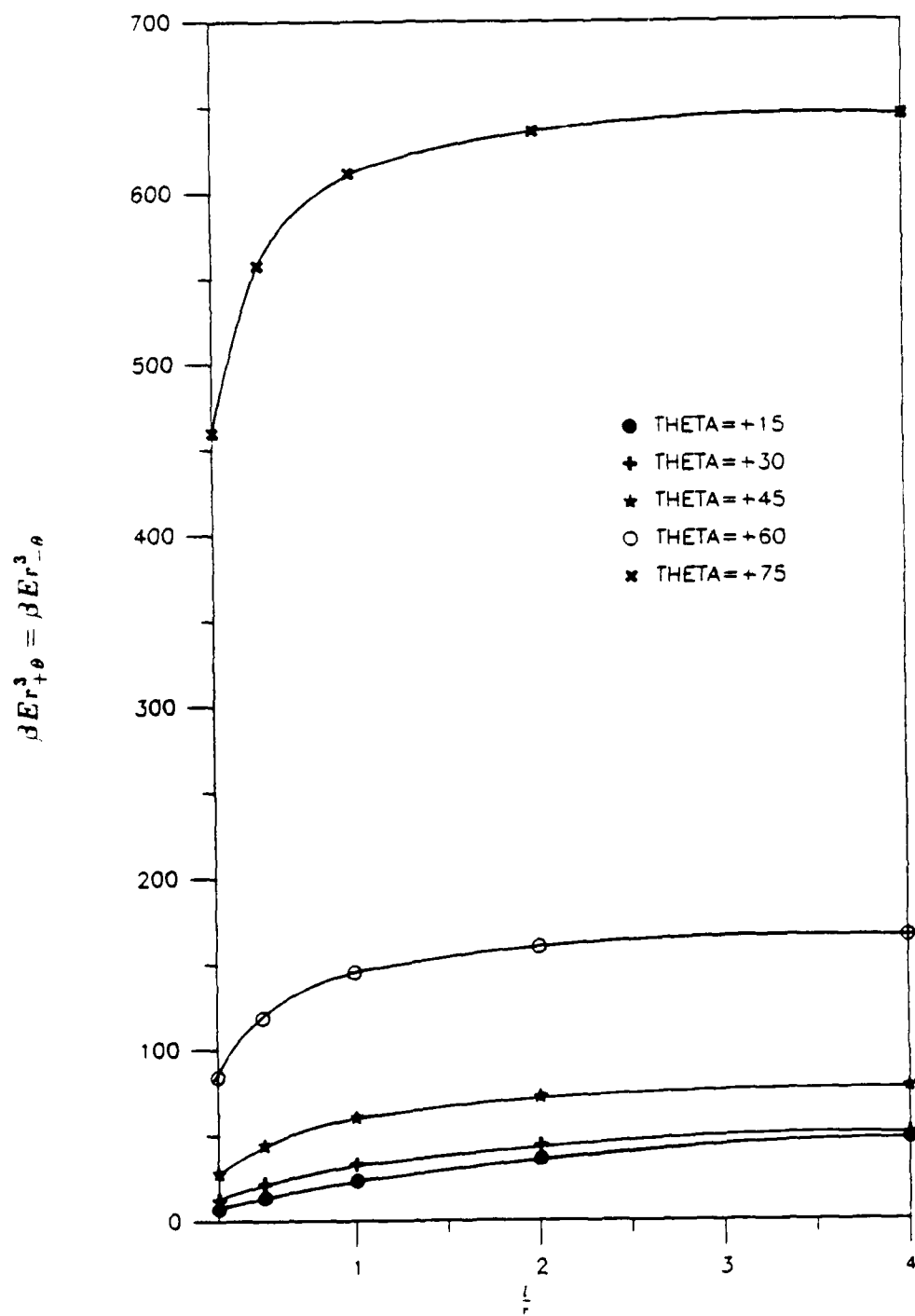


Fig. 43. Nondimensional flexibility plots ($\beta E r^3$) for conical sections with $(\frac{l}{r}) = 0.0125$, varying θ and varying $(\frac{l}{r})$ ratio.

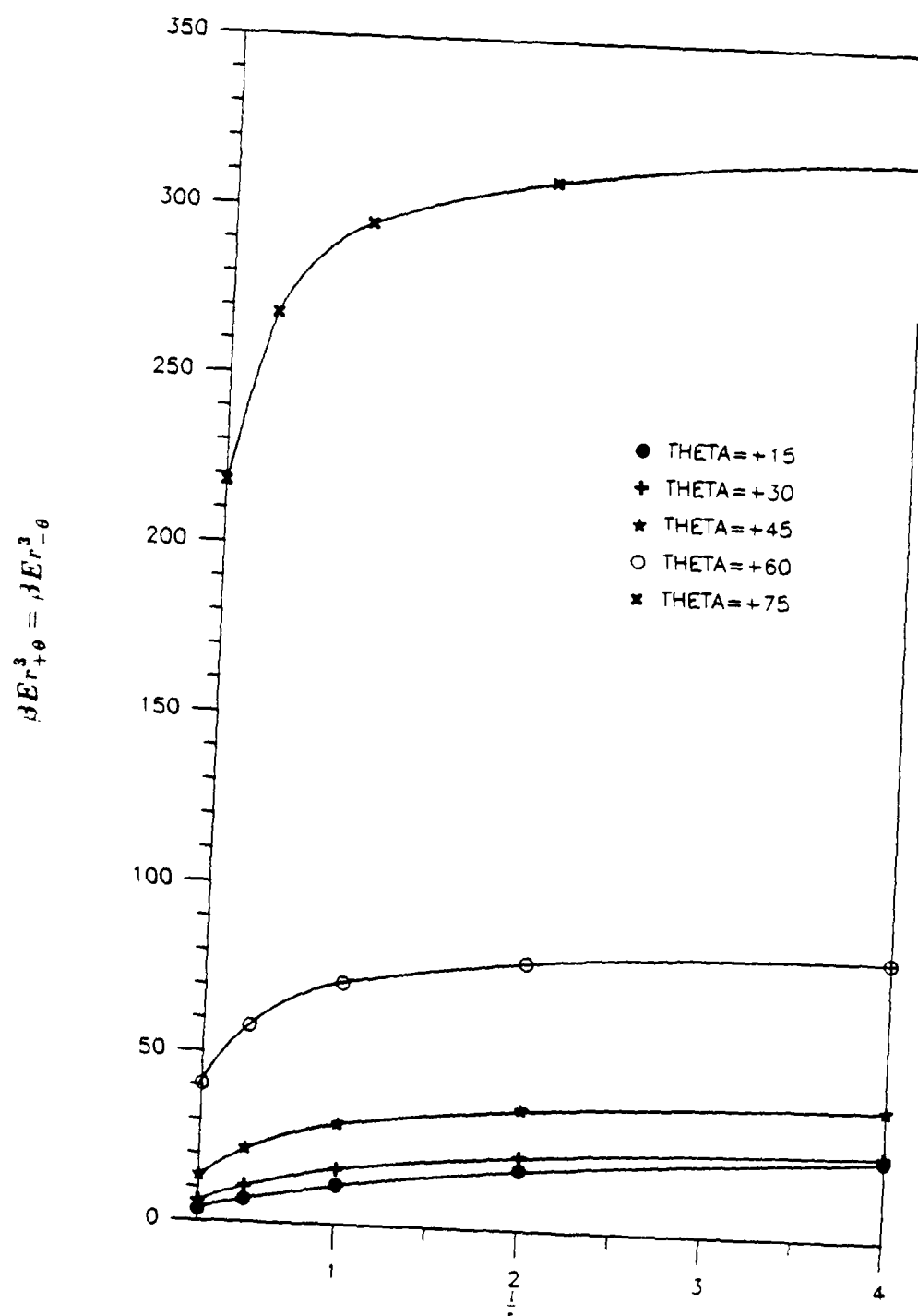


Fig. 44. Nondimensional flexibility plots ($\beta E r^3$) for conical sections with $(\frac{l}{r}) = 0.025$, varying θ and varying $(\frac{l}{r})$ ratio.

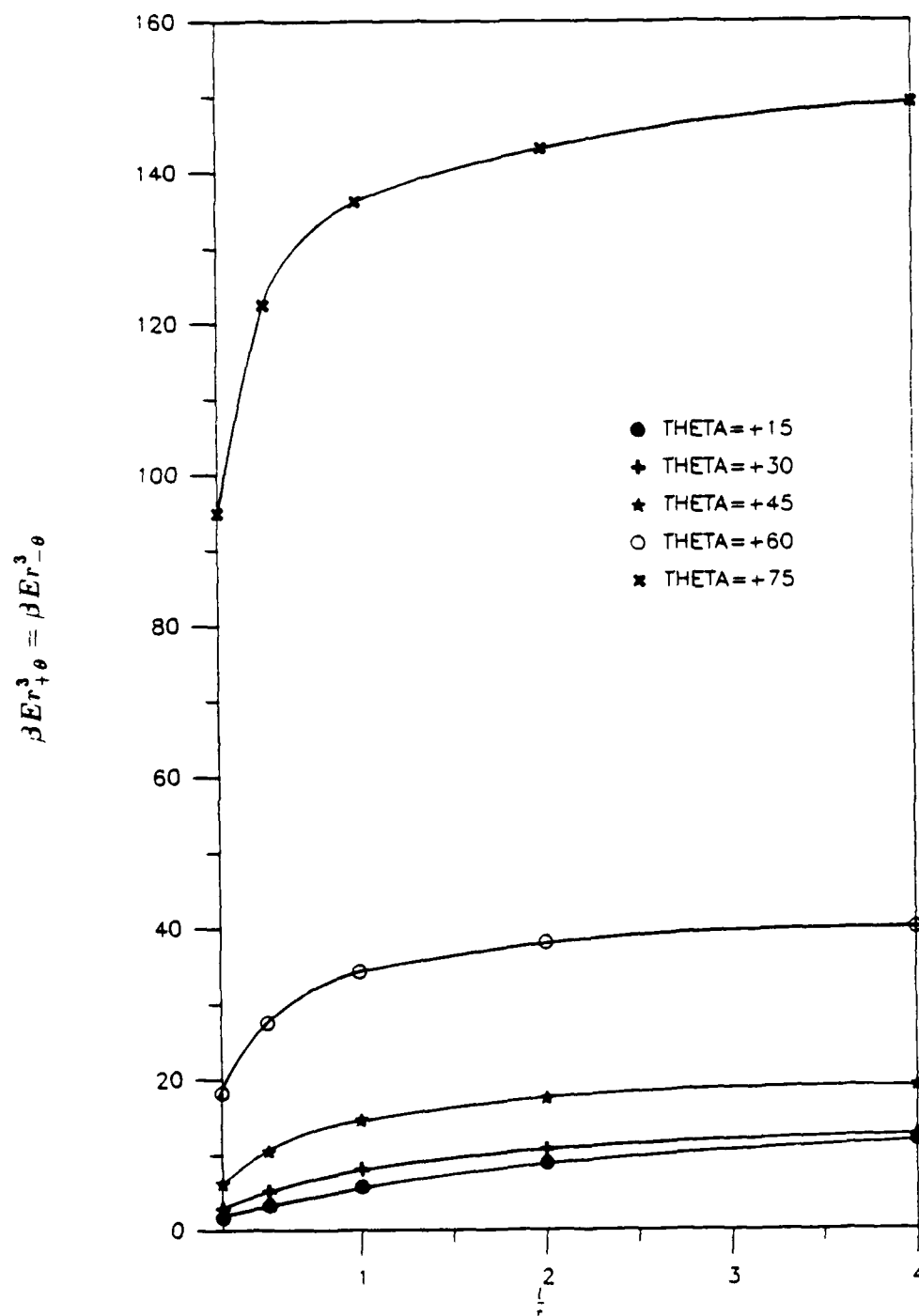


Fig. 45. Nondimensional flexibility plots ($\beta E r^3$) for conical sections with $(\frac{l}{r}) = 0.05$, varying θ and varying $(\frac{l}{r})$ ratio.

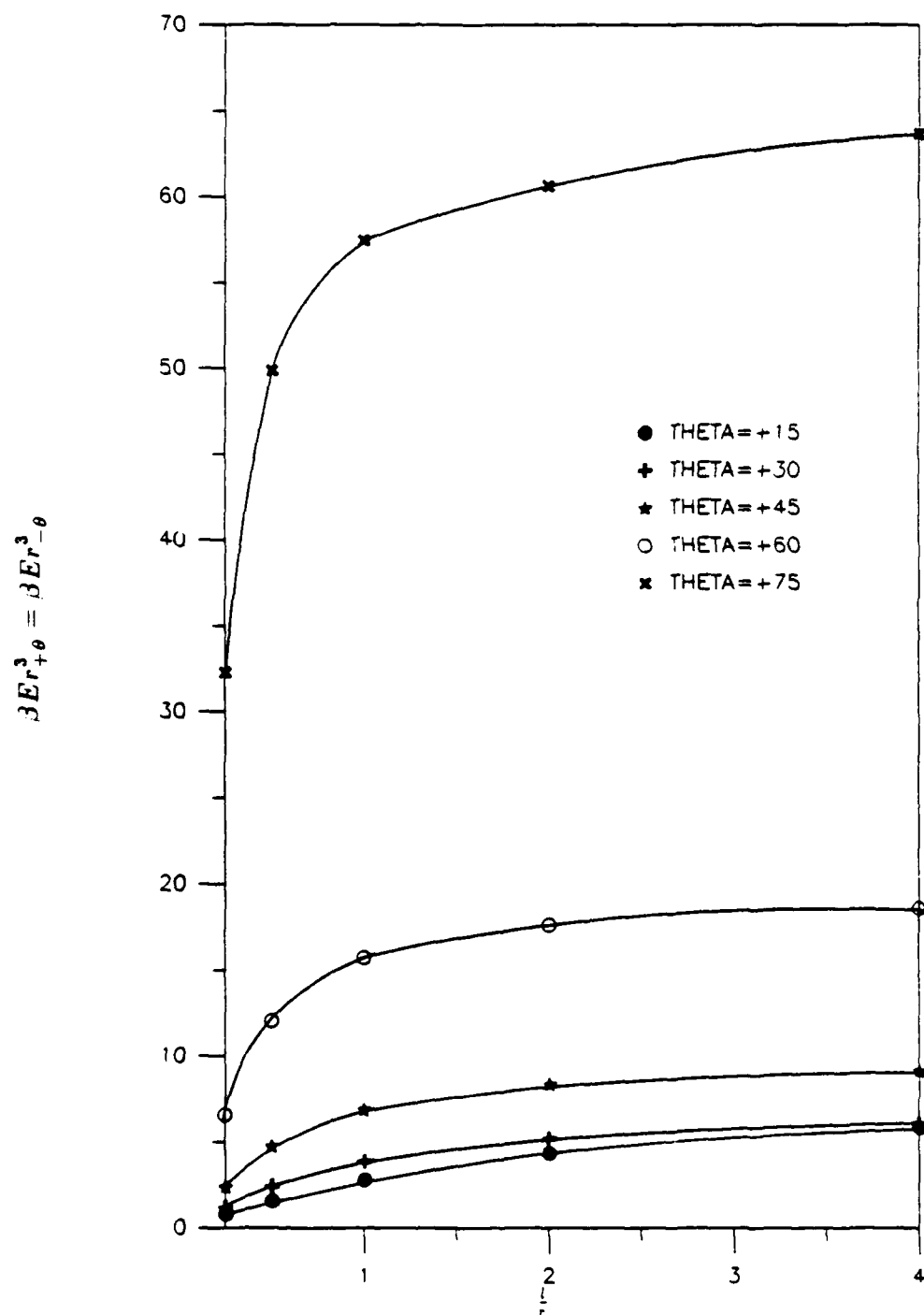


Fig. 46. Nondimensional flexibility plots ($\beta E r^3$) for conical sections with $(\frac{l}{r}) = 0.1$, varying θ and varying $(\frac{l}{r})$ ratio.

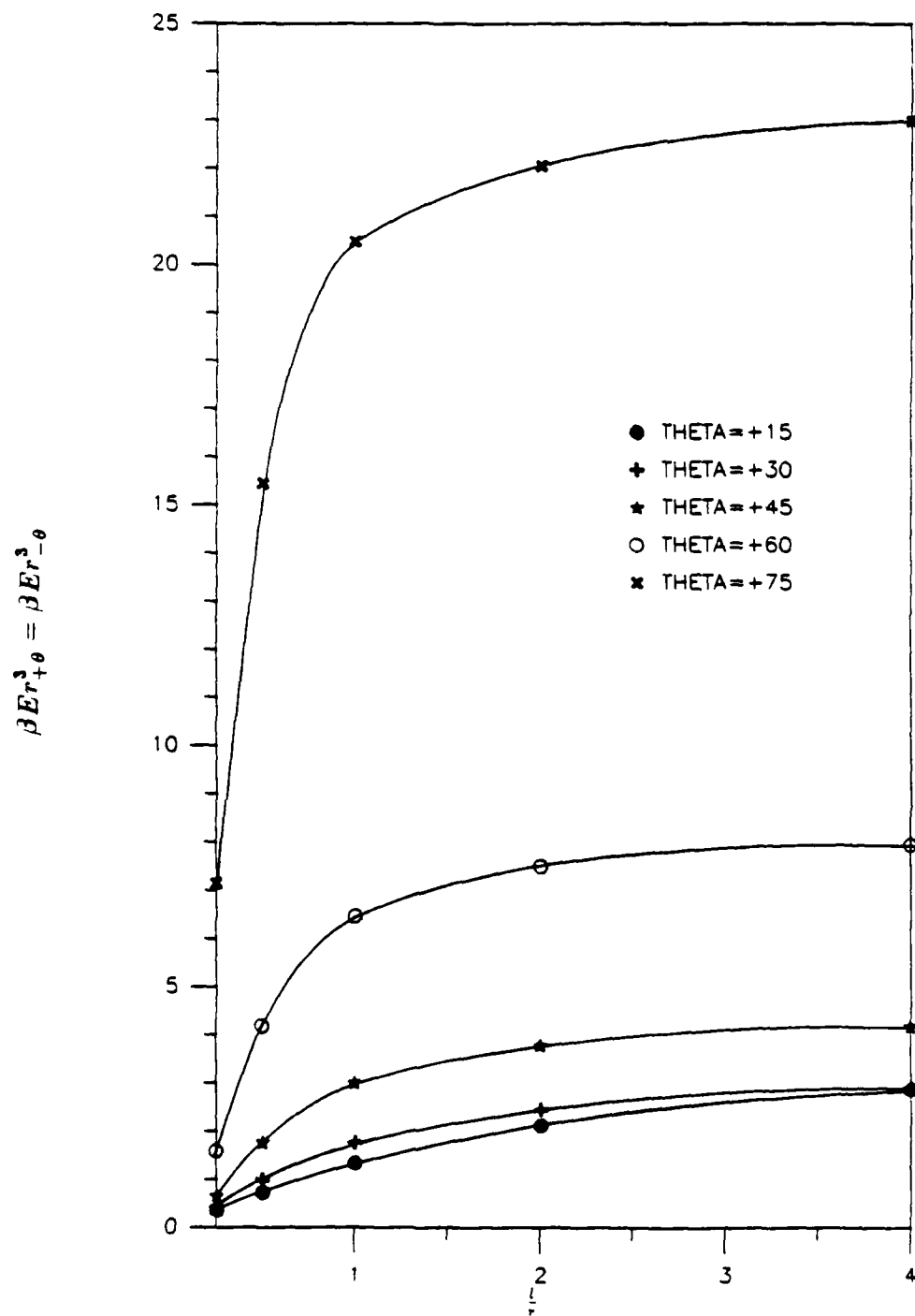


Fig. 47. Nondimensional flexibility plots ($\beta E r^3$) for conical sections with $(\frac{l}{r}) = 0.2$, varying θ and varying $(\frac{l}{r})$ ratio.

5.3 Model Verification

With any finite element computational analysis, the model must be verified in some manner to ensure acceptable computational results. The two most common methods are to try and reproduce experimental data or try and reproduce some theoretical closed form solution data. The finite element models used herein were first verified by comparison to results of theoretical closed form solutions. The models were then verified with experimental data on the 60° cone test piece described by Beamish et al., (1988). This is discussed in the rotor transfer matrix demonstration of section 5.5.1. For additional verification, the mathematical conical flexibility transformations of equations (11) through (14) were fully satisfied.

5.3.1 Cantilevered Cylinders

Six structures of cylindrical cross section, constant midwall radius ($r = 1.0$ inch), Young's Modulus of 30×10^6 psi, shear modulus of 11.54×10^6 psi, and with varying $(\frac{t}{r})$ and $(\frac{L}{r})$ ratios as listed in Table 25 were modeled with the previously described finite element procedure. The radial (Y_v) and rotational (θ_v) deflections for a unit shear load were calculated by the closed form advanced strength of materials beam theory equations found in APPENDIX A. These values were tabulated for comparison with ANSYS generated solutions in Table 25. One important preliminary concern was to observe how the ANSYS finite element models would behave for the relatively thick shells of $(\frac{t}{r}) = 0.2$. Normally, thin plates or shells based on Kirchhoff adhoc assumptions (described previously) have the limitation of $(\frac{t}{r}) > .05$. However, as listed in Table 25, for $(\frac{t}{r}) = 20$ the percentage differences for (Y_v) and (θ_v) are only 1.412 and 1.583 respectively. For these structures, the A.S.M. solutions are expected to be close

Table 25. Cantilevered Cylinder Displacements Comparison of A.S.M. method with F.E.M.

$\frac{l}{r}$	$\frac{t}{r}$	Beam Theory A.S.M. (Y_v)	Shell Theory S.F.E.M. (Y_v)	Difference (%)
20	.0125	2.3049 E-3	2.3209 E-3	.689
10	.0125	3.0363 E-4	3.0670 E-4	1.001
1	.0125	2.3530 E-6	2.4876 E-6	5.411
20	.2	1.4247 E-4	1.4451 E-4	1.412
10	.2	1.8710 E-5	1.9035 E-5	1.707
1	.2	1.3764 E-7	1.3701 E-7	-.460

$\frac{l}{r}$	$\frac{t}{r}$	Beam Theory A.S.M. (θ_v)	Shell Theory S.F.E.M. (θ_v)	Difference (%)
20	.0125	1.6976 E-4	1.7139 E-4	.951
10	.0125	4.2440 E-5	4.2848 E-5	.952
1	.0125	4.2440 E-7	4.2454 E-7	.033
20	.2	1.0505 E-5	1.0674 E-5	1.583
10	.2	2.6263 E-6	2.6651 E-6	1.456
1	.2	2.6263 E-8	2.5207 E-8	-4.189

to exact. Thus, the thick shell finite element model was accurate. However, it must be noted that the out-of-plane additional flexibilities admitted by these finite elements (discussed previously) allow even the thick shells to be modeled accurately. As expected, the thin shells for $(\frac{l}{r}) = 20$ had even better results of 0.689% and 0.951% differences of the (Y_v) and (θ_v) displacements respectively. It should also be noted at this time that for very small $(\frac{l}{r})$ ratios, neither A.S.M. closed form solutions nor shell finite elements will be accurate due to the theory geometrical limitations. For these geometries, three dimensional solid isoparametric brick elements based on elasticity theory should be used. The limits on the very small $(\frac{l}{r})$ ratios have not been established. However, for the $(\frac{l}{r})$ and $(\frac{t}{r})$ ratios used in this work with (l) always greater than (t) , the shell elements with in-plane and out-of-plane considerations are quite accurate.

Beam theory closed form solutions were generated for the complete set of model geometries for cylindrical sections. The nondimensional flexibilities $(bEr^2 = \alpha Er^2)$ are listed in Table 26. The nondimensional flexibilities (βEr^3) are listed in Table 27. The beam theory closed form solutions are plotted together with the S.F.E.M. solutions from tables 3 and 4 on figures 48 through 57. For pure bending, the beam theory closed form solutions are expected to be close to exact. It can be seen by the comparison of these plots that the ANSYS models are very accurate.

Table 26. Beam Theory Closed Form Nondimensional Flexibilities ($bEr^2 = \alpha Er^2$) for Cylindrical Sections ($\Theta = 0$) with Varying ($\frac{l}{r}$) and ($\frac{t}{r}$) Ratios.

$\frac{t}{r}$	$\frac{l}{r}$	$bEr^2 = \alpha Er^2$
0.0125	0.25	0.795744
	0.5	3.18298
	1.0	12.7319
	2.0	50.9276
	4.0	203.711
0.025	0.25	0.397826
	0.5	1.59130
	1.0	6.36521
	2.0	25.4608
	4.0	101.843
0.05	0.25	0.198820
	0.5	0.795278
	1.0	3.18111
	2.0	12.7245
	4.0	50.8978
0.1	0.25	0.0992239
	0.5	0.396895
	1.0	1.58758
	2.0	6.35033
	4.0	25.4013
0.2	0.25	0.0492435
	0.5	0.196974
	1.0	0.787896
	2.0	3.15159
	4.0	12.6063

Table 27. Beam Theory Closed Form Nondimensional Flexibilities (βEr^3) for Cylindrical Sections ($\Theta = 0$) with Varying ($\frac{l}{r}$) and ($\frac{t}{r}$) Ratios.

$\frac{t}{r}$	$\frac{l}{r}$	βEr^3
0.0125	0.25	6.36595
	0.5	12.7319
	1.0	25.4638
	2.0	50.9276
	4.0	101.855
0.025	0.25	3.18260
	0.5	6.36521
	1.0	12.7304
	2.0	25.4608
	4.0	50.9217
0.05	0.25	1.59056
	0.5	3.18111
	1.0	6.36223
	2.0	12.7245
	4.0	25.4489
0.1	0.25	0.793791
	0.5	1.58758
	1.0	3.17516
	2.0	6.35033
	4.0	12.7007
0.2	0.25	0.393948
	0.5	0.787896
	1.0	1.57579
	2.0	3.15159
	4.0	6.30317

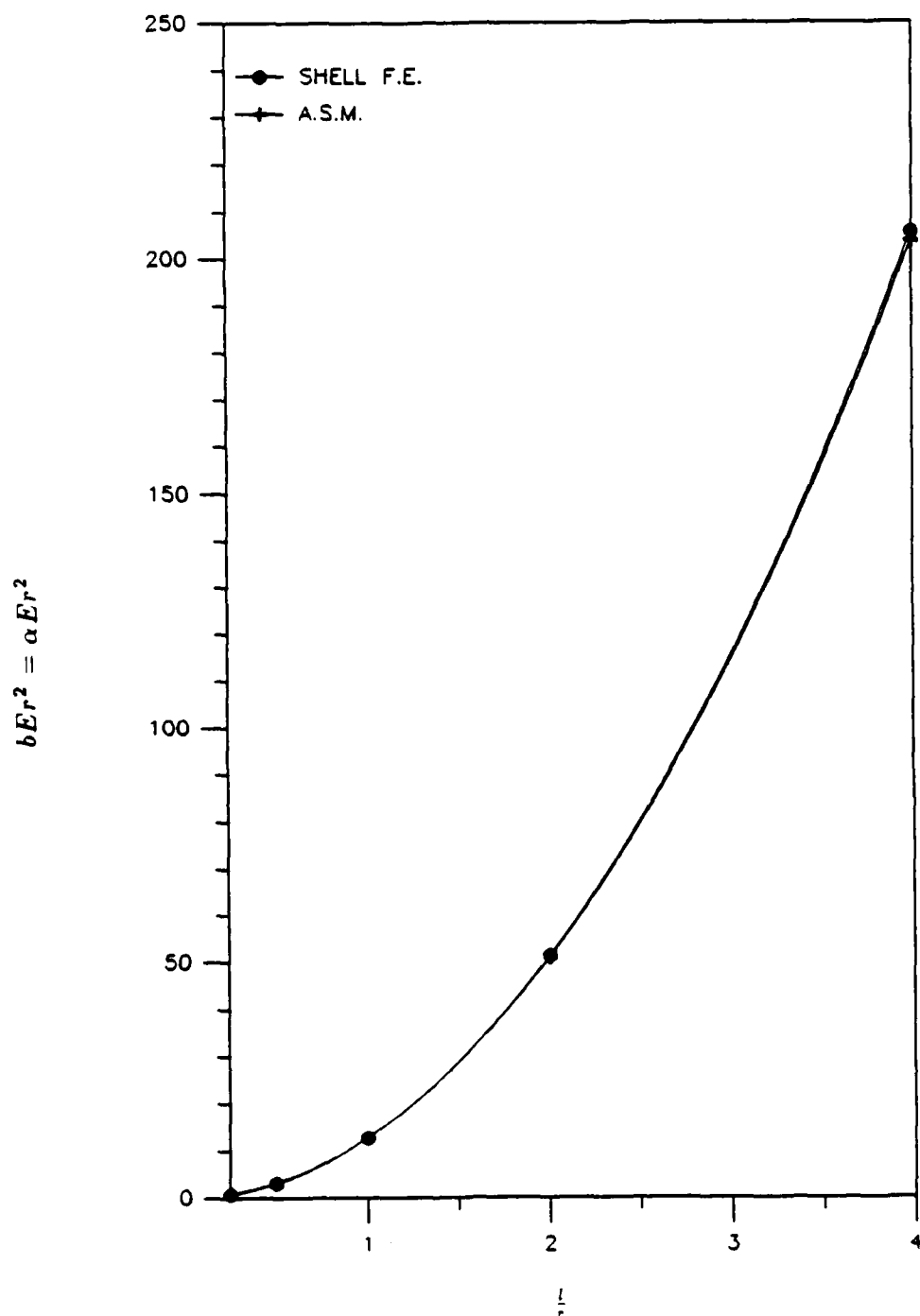


Fig. 48. Beam theory closed form nondimensional flexibility plots compared to finite element nondimensional flexibility plots ($bEr^2 = \alpha Er^2$) for cylindrical sections ($\theta = 0$) with varying (l/r) ratios and (t/r) = .0125.

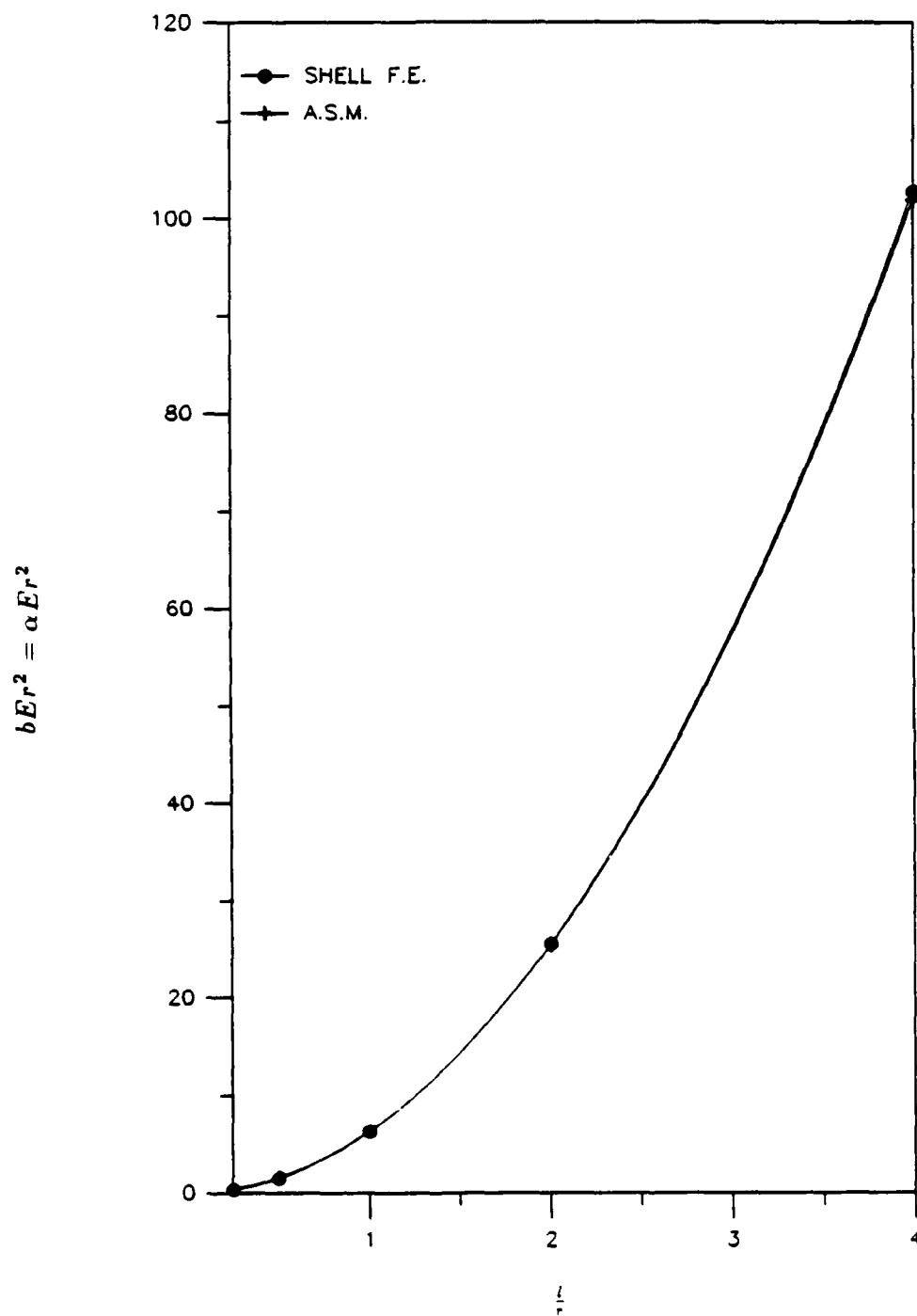


Fig. 49. Beam theory closed form nondimensional flexibility plots compared to finite element nondimensional flexibility plots ($bEr^2 = \alpha Er^2$) for cylindrical sections ($\theta = 0$) with varying ($\frac{l}{r}$) ratios and ($\frac{t}{r}$) = .025.

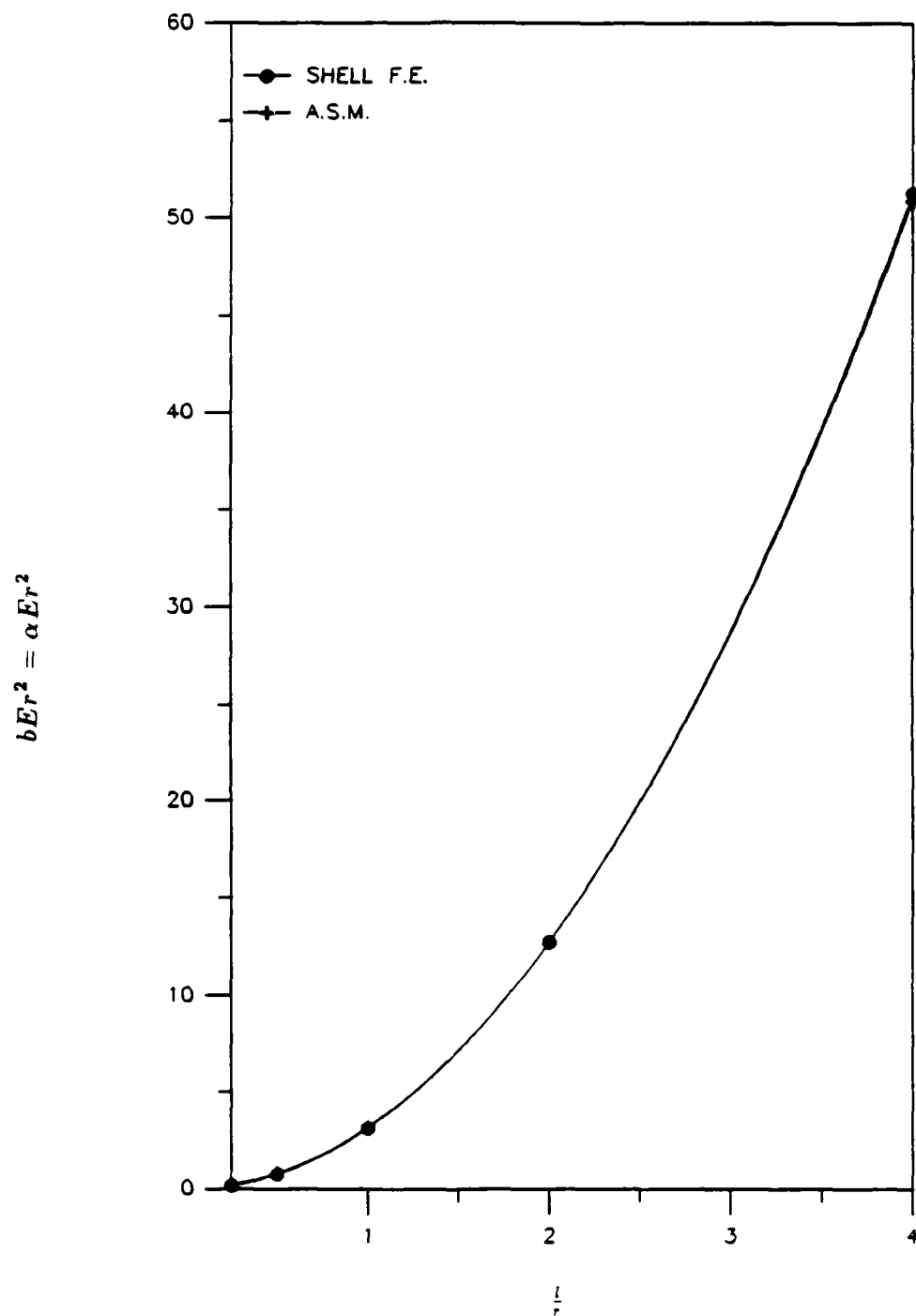


Fig. 50. Beam theory closed form nondimensional flexibility plots compared to finite element nondimensional flexibility plots ($bEr^2 = \alpha Er^2$) for cylindrical sections ($\theta = 0$) with varying ($\frac{l}{r}$) ratios and ($\frac{t}{r}$) = .05.

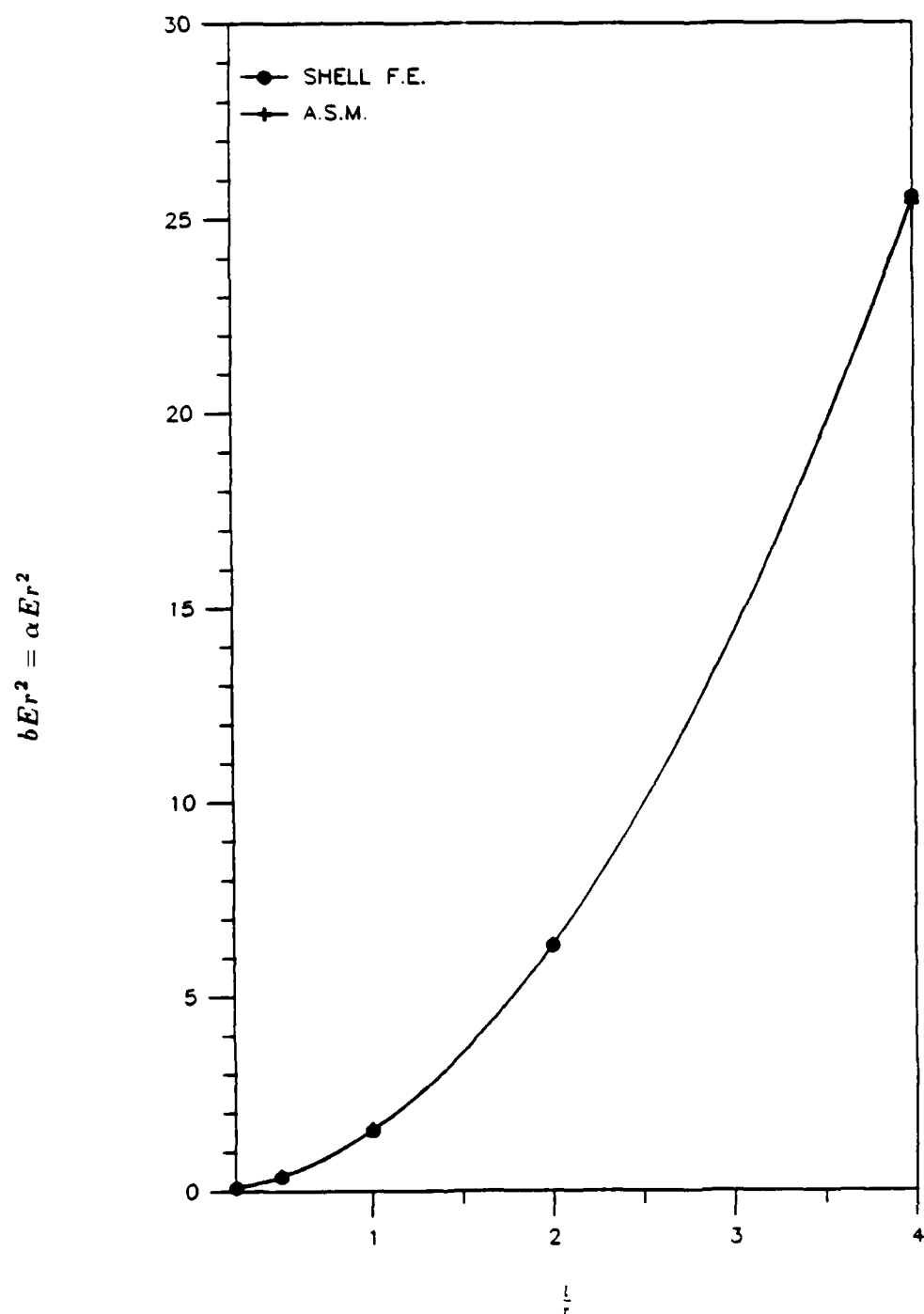


Fig. 51. Beam theory closed form nondimensional flexibility plots compared to finite element nondimensional flexibility plots ($bEr^2 = \alpha Er^2$) for cylindrical sections ($\theta = 0$) with varying $(\frac{l}{r})$ ratios and $(\frac{t}{r}) = .1$.

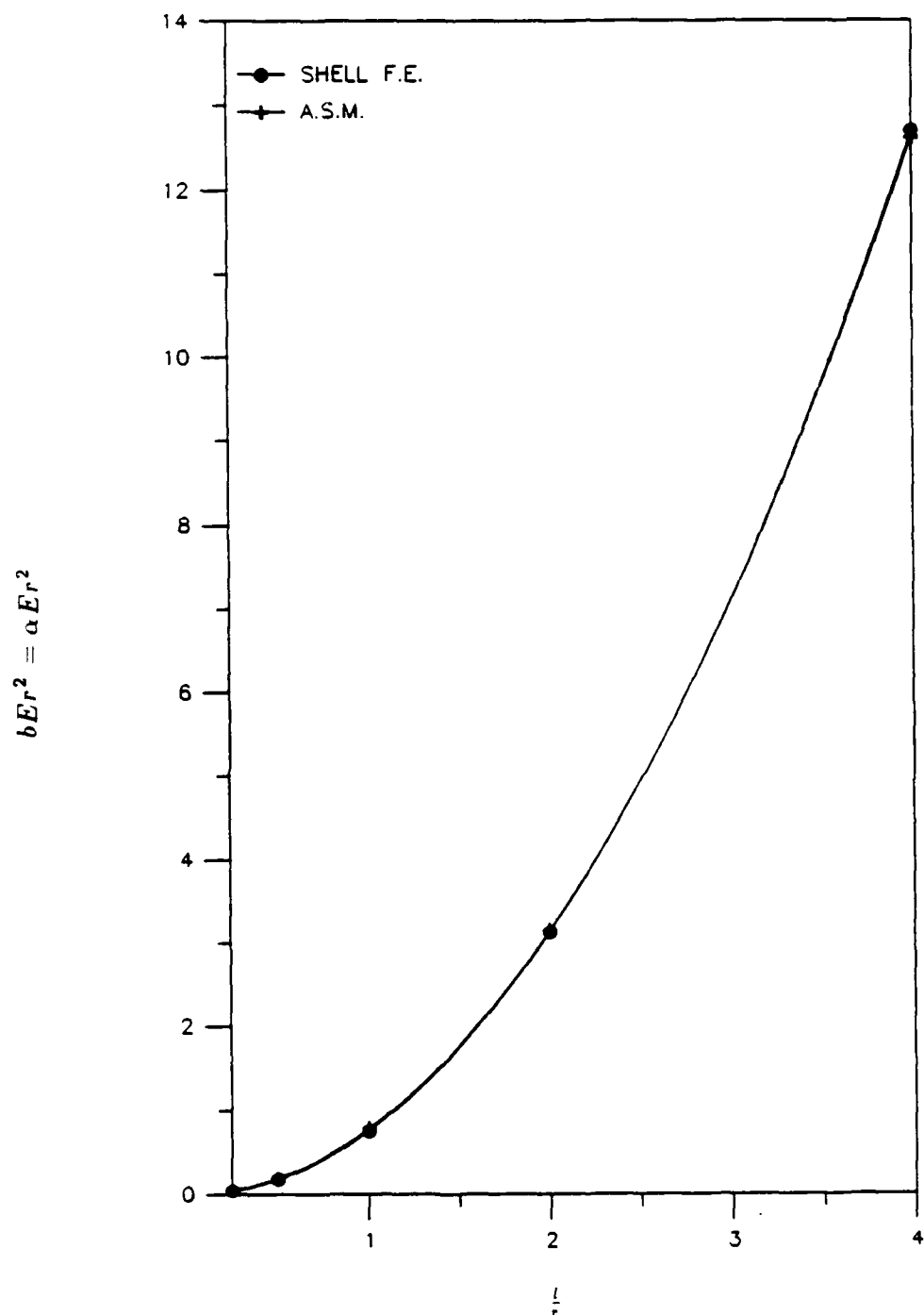


Fig. 52. Beam theory closed form nondimensional flexibility plots compared to finite element nondimensional flexibility plots ($bEr^2 = \alpha Er^2$) for cylindrical sections ($\theta = 0$) with varying (l/r) ratios and (t/r) = .2.

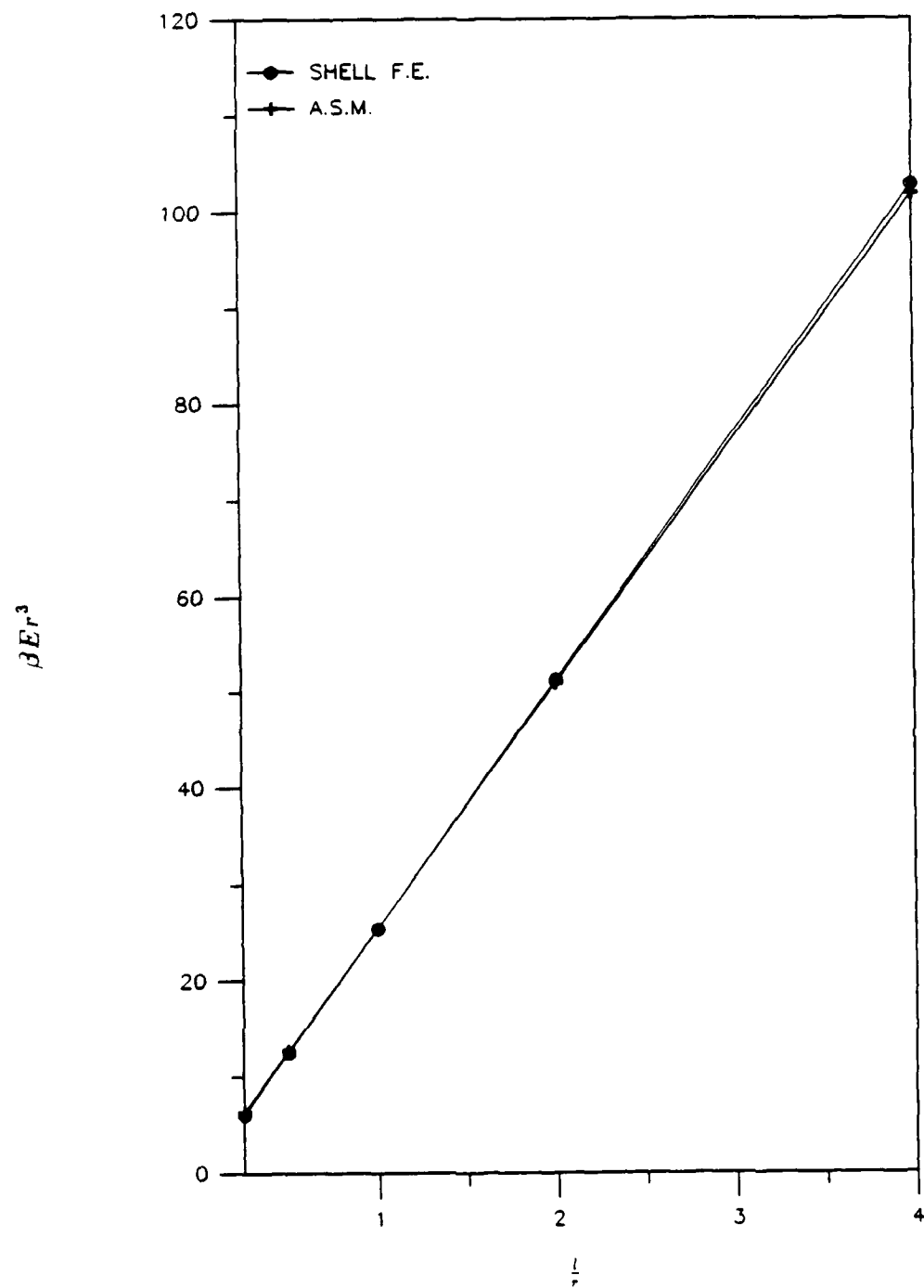


Fig. 53. Beam theory closed form nondimensional flexibility plots compared to finite element nondimensional flexibility plots ($\beta E r^3$) for cylindrical sections ($\theta = 0$) with varying (l/r) ratios and (t/r) = .0125.

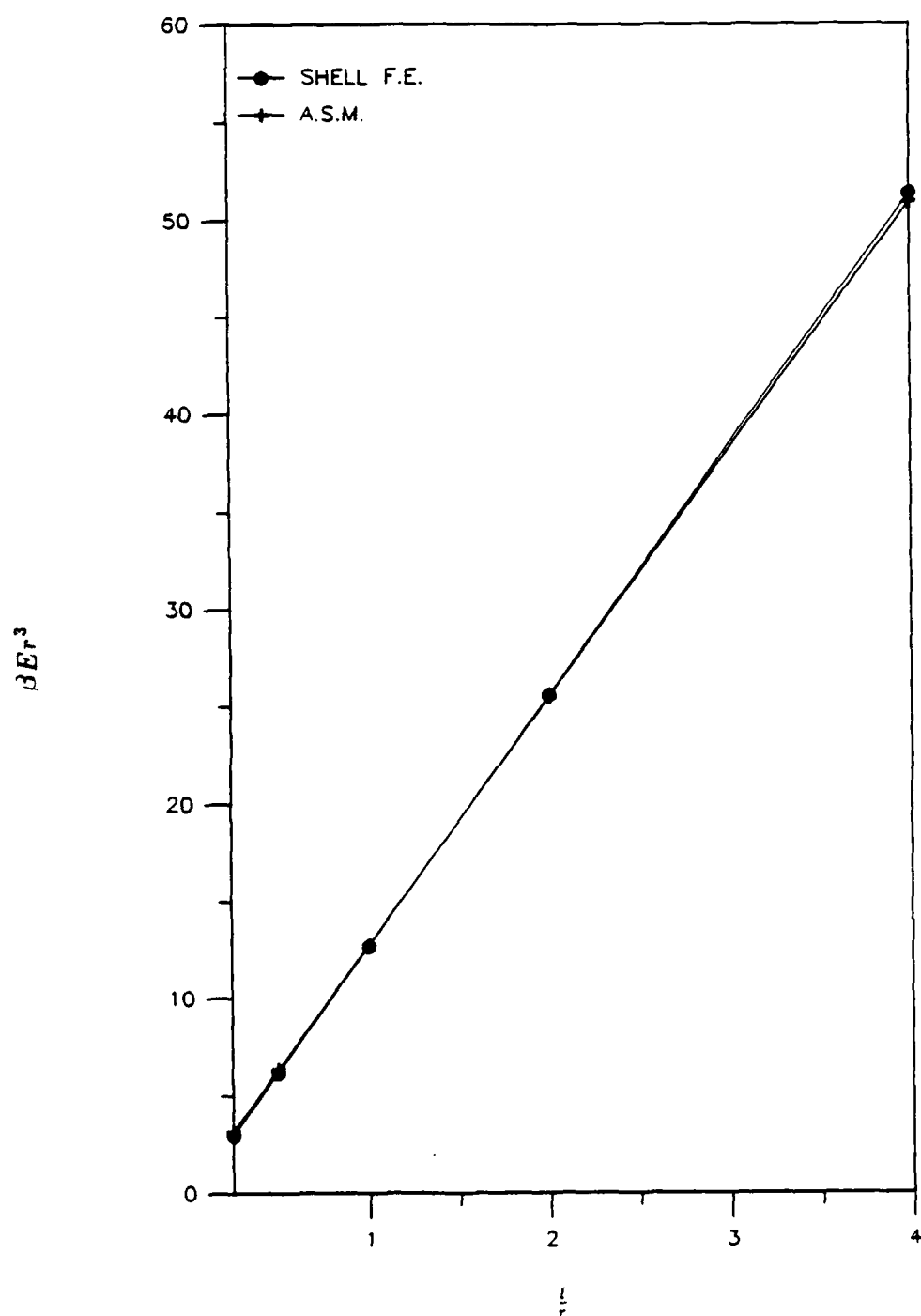


Fig. 54. Beam theory closed form nondimensional flexibility plots compared to finite element nondimensional flexibility plots ($\beta E r^3$) for cylindrical sections ($\theta = 0$) with varying (l/r) ratios and (t/r) = .025.

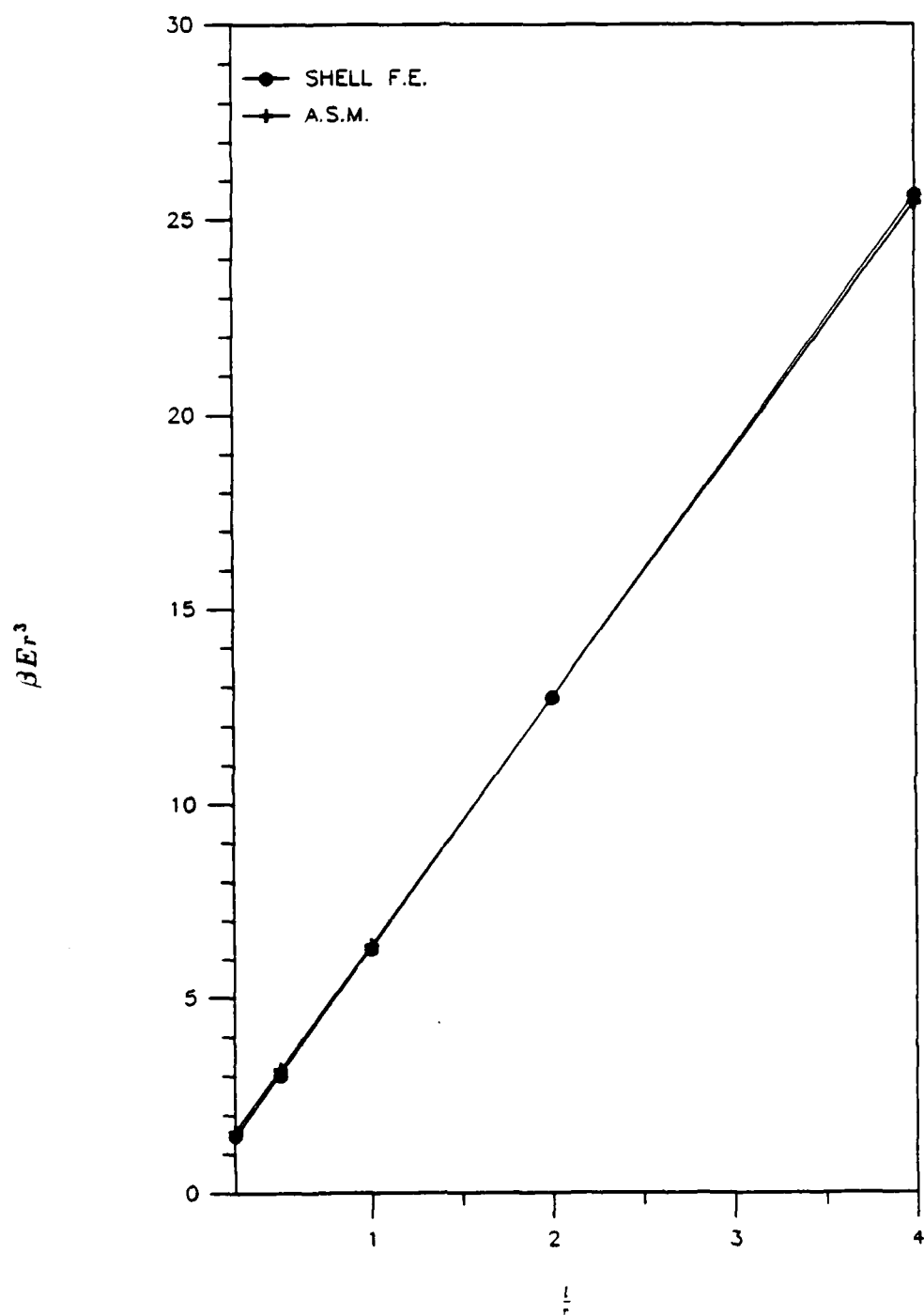


Fig. 55. Beam theory closed form nondimensional flexibility plots compared to finite element nondimensional flexibility plots ($\beta E r^3$) for cylindrical sections ($\theta = 0$) with varying ($\frac{l}{r}$) ratios and ($\frac{t}{r}$) = .05.

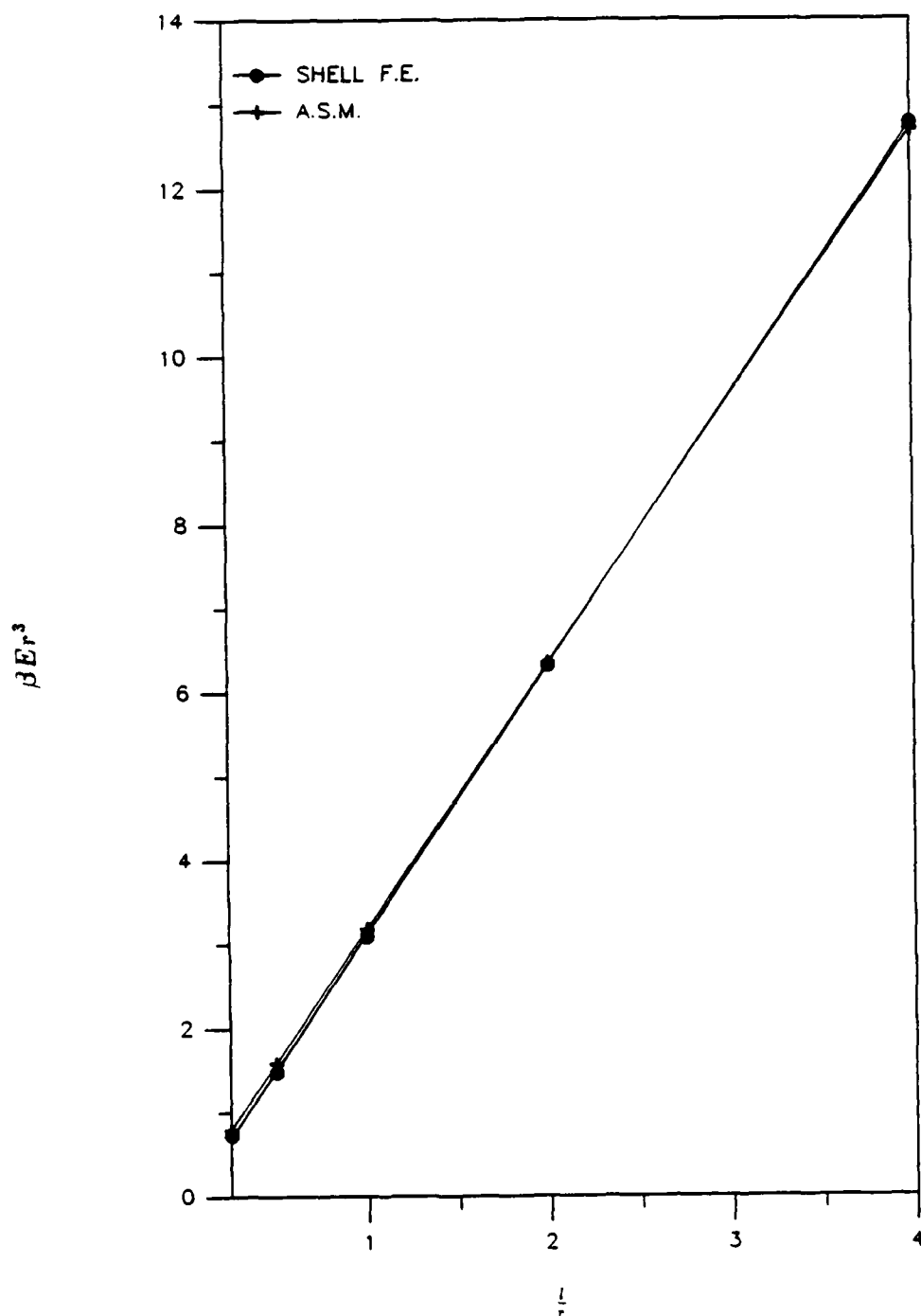


Fig. 56. Beam theory closed form nondimensional flexibility plots compared to finite element nondimensional flexibility plots ($\beta E r^3$) for cylindrical sections ($\theta = 0$) with varying (l/r) ratios and (t/r) = .1.

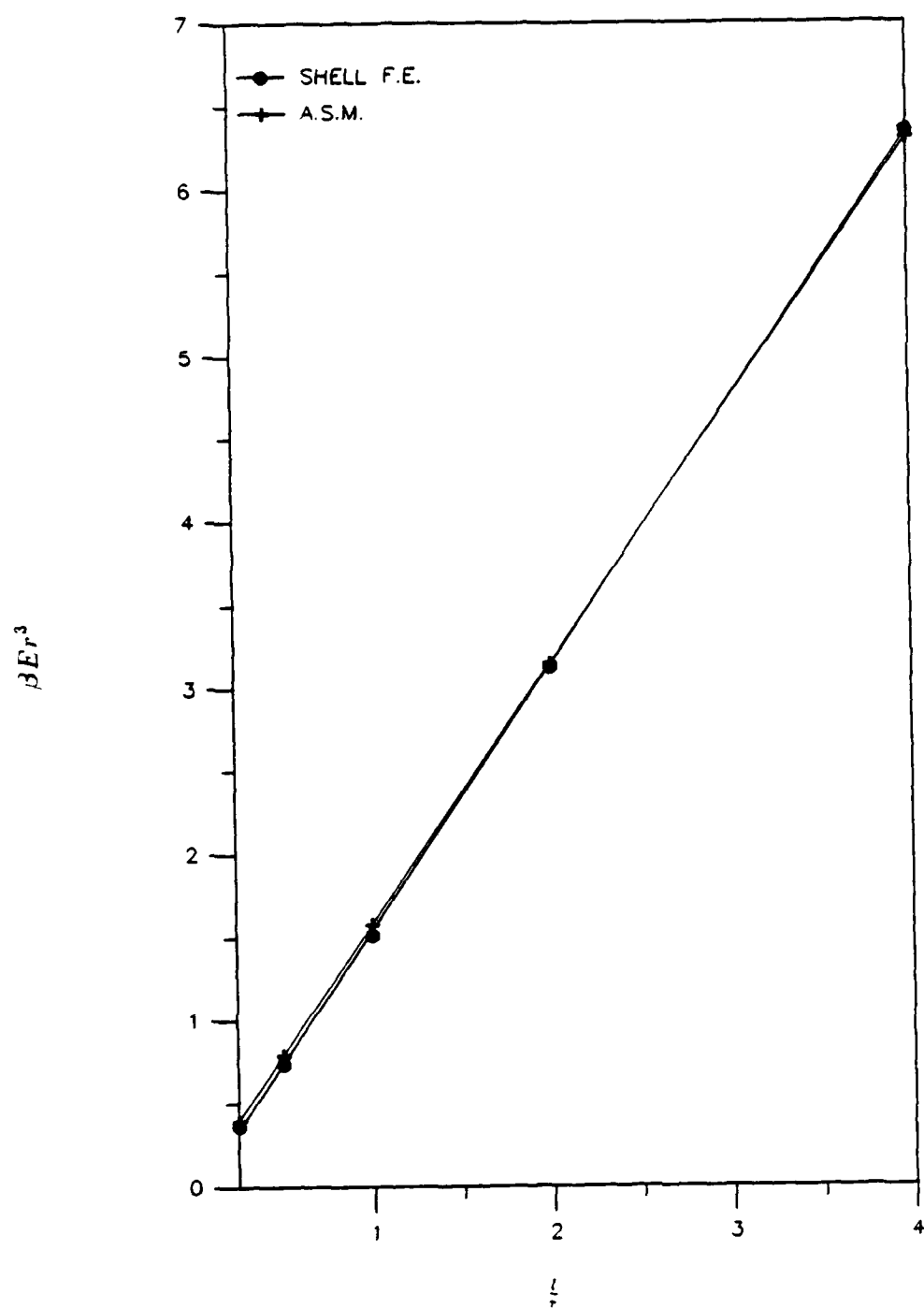


Fig. 57. Beam theory closed form nondimensional flexibility plots compared to finite element nondimensional flexibility plots ($\beta E r^3$) for cylindrical sections ($\theta = 0$) with varying ($\frac{l}{r}$) ratios and ($\frac{t}{r}$) = .2.

5.3.2 Conical Flexibility Transformations

An additional method of model verification is the satisfaction of the mathematical flexibility transformations of APPENDIX C,

$$\begin{aligned}
 a_n &= a_p - l(b_p) + l^2(\beta_p) - l(\alpha_p) \\
 b_n &= l(\beta_p) - b_p \\
 \alpha_n &= l(\beta_p) - \alpha_p \\
 \beta_n &= \beta_p
 \end{aligned}
 \tag{C10}$$

or more specifically for an axisymmetric conical structure,

$$a_n = a_p \tag{11}$$

$$b_n = \alpha_p \tag{12}$$

$$\alpha_n = b_p \tag{13}$$

$$\beta_n = \beta_p \tag{14}$$

These mathematical expressions would not be satisfied if there were any boundary condition errors in the models. This is explained by the energy theorems of Betti and Maxwell (Tuma (1969)). All of the flexibilities of the 275 models were input into the above equations of (C10) and (11) through (14). All mathematical identities were satisfied.

5.4 Including Shear in Beam Theory

Different practices accounting for shear are currently being used in rotor-dynamic transfer matrix programs. Some do not include any shear effects at all, and most use a constant shear form factor, $K_s = 0.75$. Neither of these practices is adequate over the full range of section geometries and can result in large percentage errors in the flexibility coefficient (aEr). Table 28 lists the nondimensional flexibilities (aEr) of cylindrical sections for the closed form beam theory solutions using the constant shear form factor. Table 29 lists the nondimensional flexibilities (aEr) of cylindrical sections for the closed form solutions with the improvements of advanced strength of materials (A.S.M.). (K_s is determined by equation (A9)). Table 2 (discussed previously) lists the nondimensional flexibilities (aEr) of cylindrical sections determined by the shell finite element analysis. Figures 58 through 62 illustrate the large percentage errors of assuming a constant $K_s = 0.75$. It can be seen from these plots that the assumption of a constant shear form factor can cause very significant errors in flexibilities. When modelling cylindrical beam sections for rotor dynamics analysis. The A.S.M. closed form solution should always be used. However, the closed form solution using A.S.M. is also not exact. Whether the shell flexibilities are closer to the real values than the A.S.M. method is unproven for these cylindrical sections. However, it is assumed that the shell flexibilities for the thin sections are more accurate than the A.S.M. flexibilities. Because the nature of the curves don't change appreciably with thickness, it is further assumed that the shells are more accurate over the entire range of section geometries contained in this work.

Table 28. Beam Theory Closed Form Nondimensional Flexibilities (aEr) with ($K_s = .75$) for Cylindrical Sections ($\theta = 0$) with Varying ($\frac{l}{r}$) and ($\frac{t}{r}$) Ratios.

$\frac{t}{r}$	$\frac{l}{r}$	aEr
.0125	0.25	-10.9689
	0.5	-21.5399
	1.0	-39.8968
	2.0	-54.3298
	4.0	95.0510
.025	0.25	-5.48444
	0.5	-10.7700
	1.0	-19.9486
	2.0	-27.1669
	4.0	47.5096
.05	0.25	-2.74220
	0.5	-5.38505
	1.0	-9.97482
	2.0	-13.5874
	4.0	23.7230
.1	0.25	-1.37113
	0.5	-2.69265
	1.0	-4.98840
	2.0	-6.80164
	4.0	11.79803
.2	0.25	-.685596
	0.5	-1.34657
	1.0	-2.49617
	2.0	-3.41654
	4.0	5.77326

Table 29. Beam Theory Closed Form Nondimensional Flexibilities (aEr) for Cylindrical Sections ($\Theta = 0$) with Varying ($\frac{t}{r}$) and ($\frac{l}{r}$) Ratios.

$\frac{t}{r}$	$\frac{l}{r}$	aEr
0.0125	0.25	-15.4535
	0.5	-30.5091
	1.0	-57.8353
	2.0	-90.2067
	4.0	23.2971
0.025	0.25	-7.68799
	0.5	-15.1771
	1.0	-28.7628
	2.0	-44.7953
	4.0	12.2528
0.05	0.25	-3.80561
	0.5	-7.51181
	1.0	-14.2283
	2.0	-22.0945
	4.0	6.70889
0.1	0.25	-1.86516
	0.5	-3.68071
	1.0	-6.96452
	2.0	-10.7539
	4.0	3.89354
0.2	0.25	-0.896419
	0.5	-1.76822
	1.0	-3.33946
	2.0	-5.10312
	4.0	2.40010

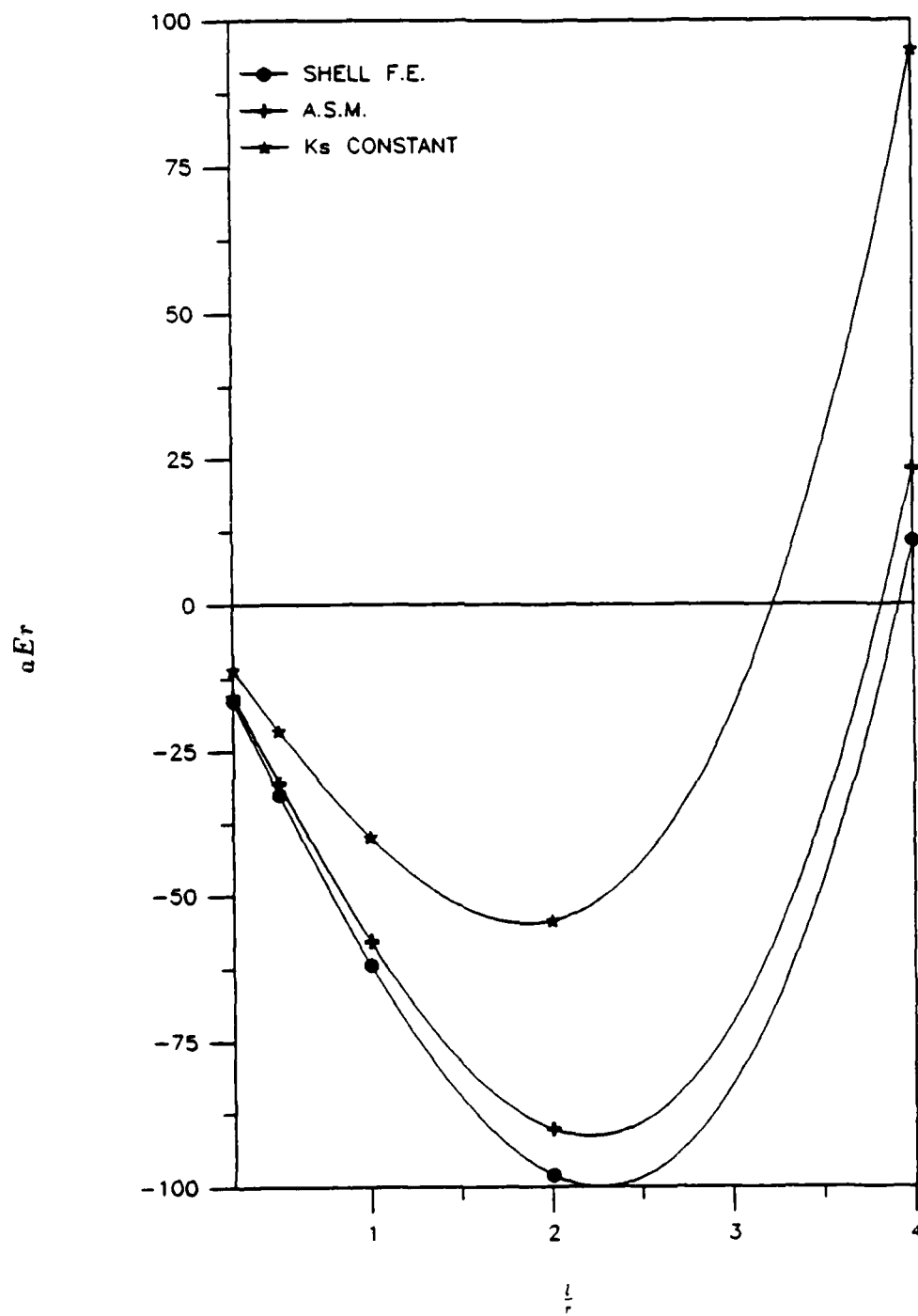


Fig. 58. Beam theory closed form nondimensional flexibility plots compared to finite element nondimensional flexibility plots (aEr) for cylindrical sections ($\Theta = 0$) with varying $(\frac{l}{r})$ ratios and $(\frac{t}{r}) = .0125$.

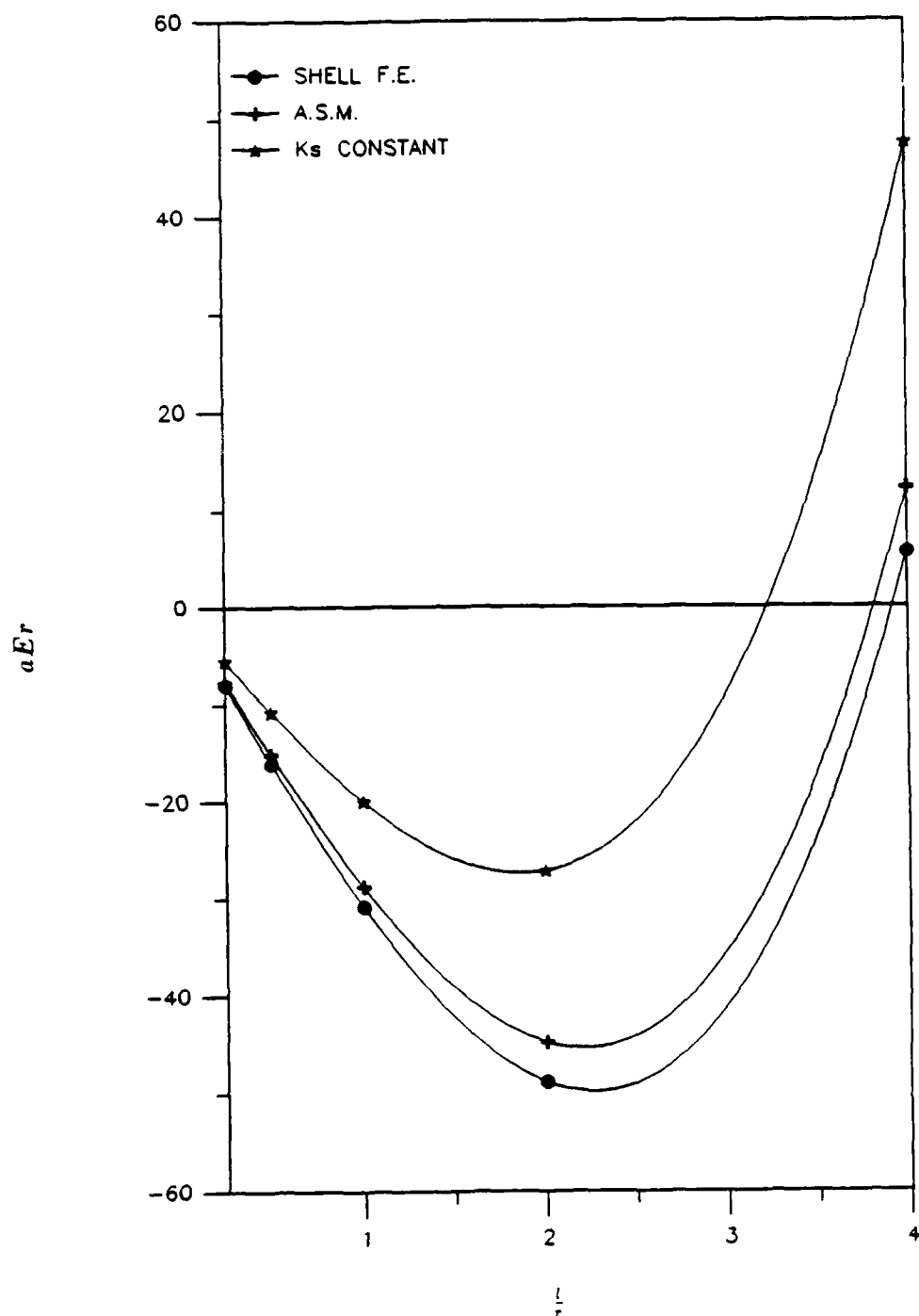


Fig. 59. Beam theory closed form nondimensional flexibility plots compared to finite element nondimensional flexibility plots (aEr) for cylindrical sections ($\Theta = 0$) with varying (l/r) ratios and (t/r) = .025.

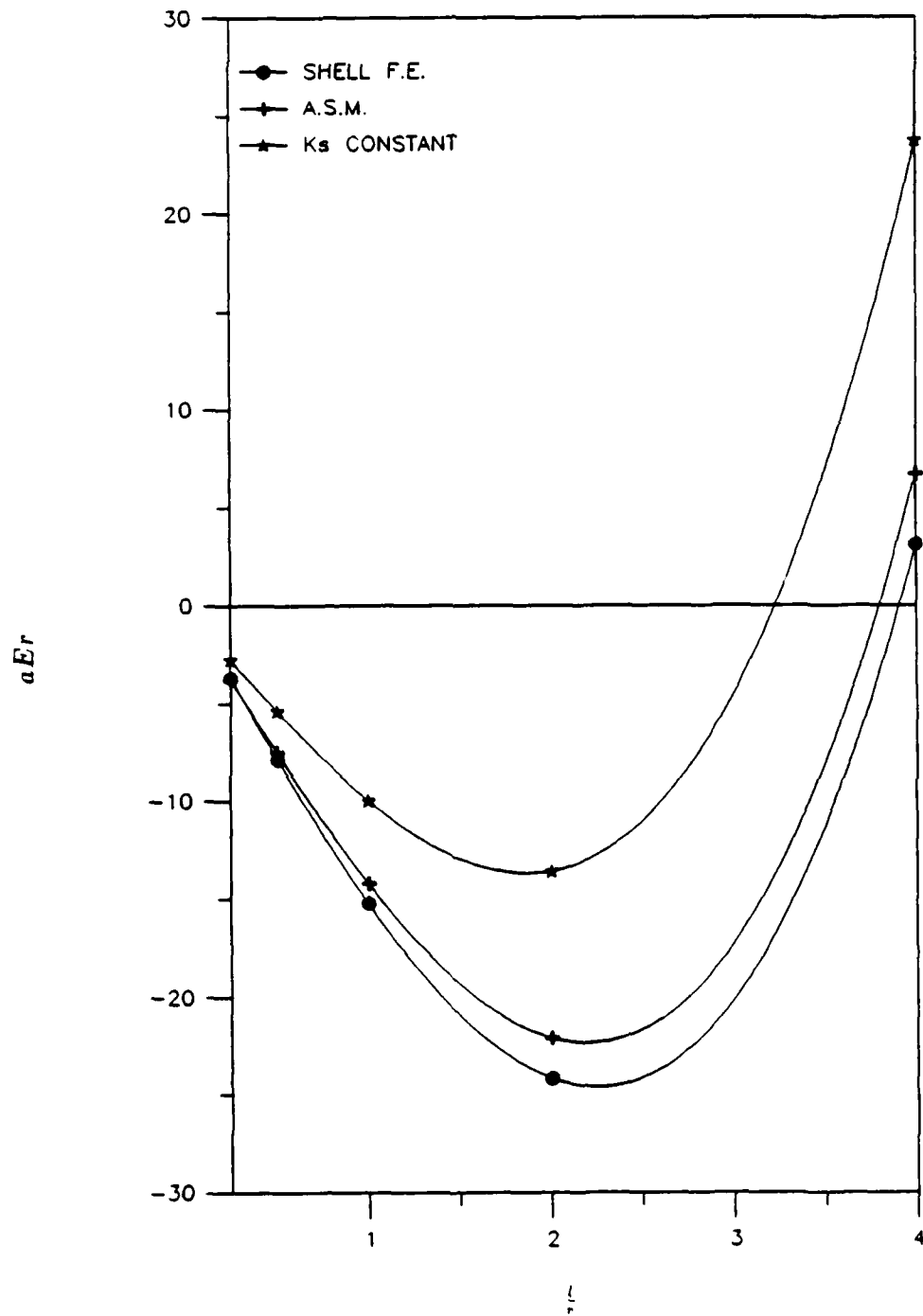


Fig. 60. Beam theory closed form nondimensional flexibility plots compared to finite element nondimensional flexibility plots (aEr) for cylindrical sections ($\Theta = 0$) with varying ($\frac{l}{r}$) ratios and ($\frac{t}{r} = .05$).

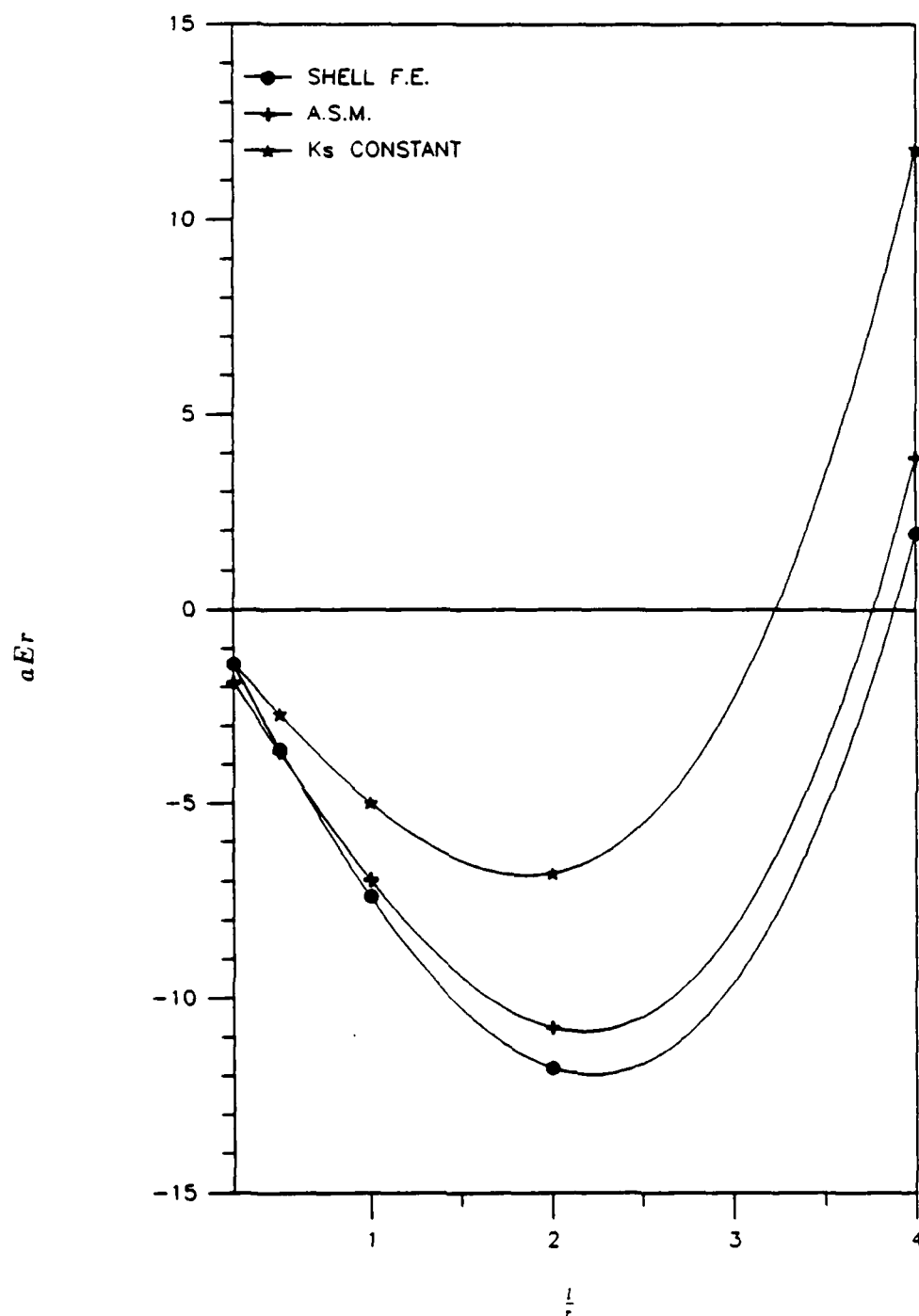


Fig. 61. Beam theory closed form nondimensional flexibility plots compared to finite element nondimensional flexibility plots (aEr) for cylindrical sections ($\Theta = 0$) with varying ($\frac{l}{r}$) ratios and ($\frac{t}{r}$) = .1.

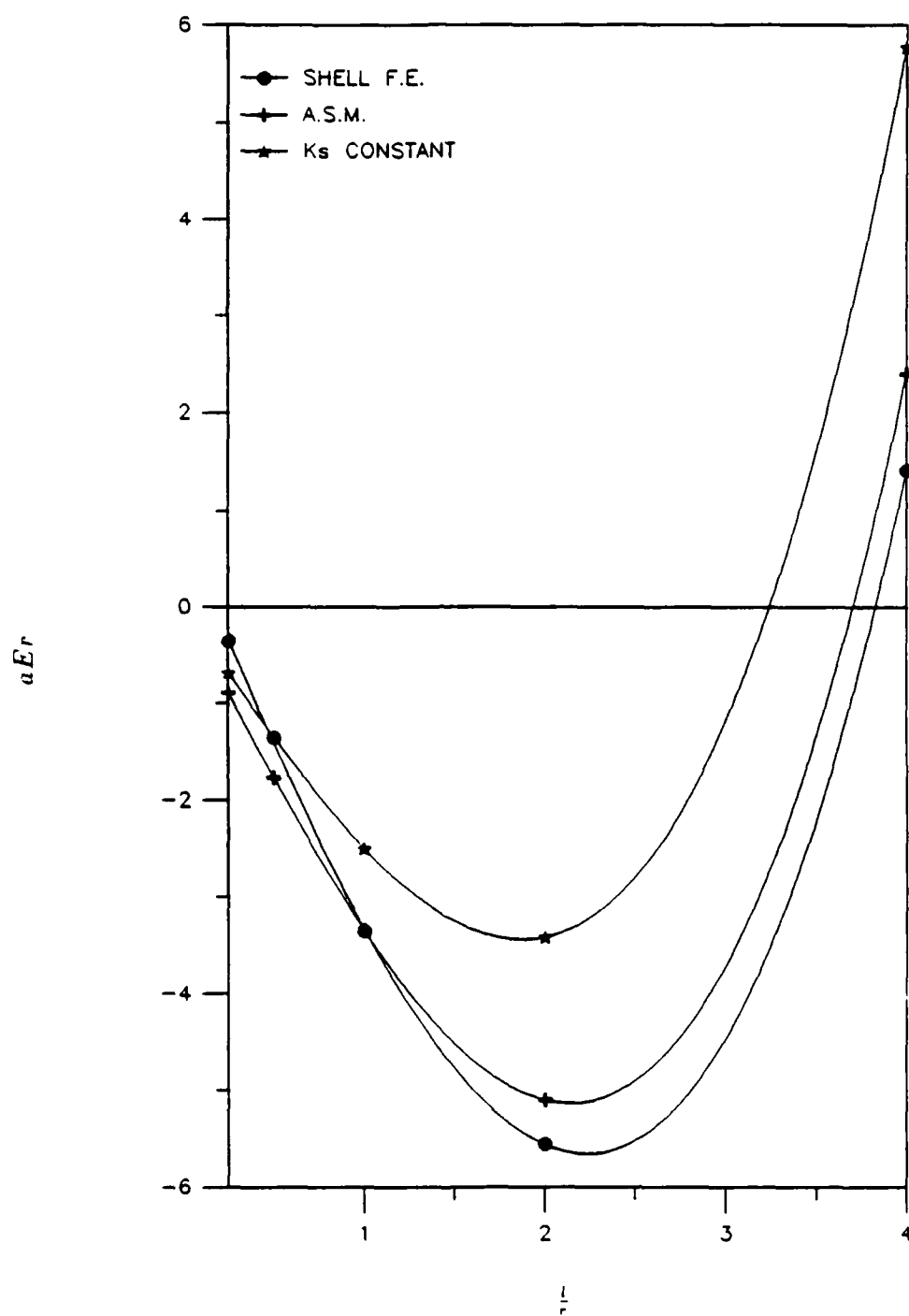


Fig. 62. Beam theory closed form nondimensional flexibility plots compared to finite element nondimensional flexibility plots (aEr) for cylindrical sections ($\Theta = 0$) with varying (l/r) ratios and (t/r) = .2.

5.5 Rotor Transfer Matrix Demonstrations

The impact of modeling conical sections with the shell flexibility coefficients in place of the stepped discrete beam flexibility coefficients is significant. Two models were picked to demonstrate the impact of using shell elements in place of beam elements. The first modeled was the 60° cone test piece of Beamish et al., (1988). The fundamental free-free natural frequency was determined and the mode shape plotted.

The second transfer matrix demonstration was performed on the Space Shuttle Main Engine High Pressure Oxidizer Turbopump (SSME HPOTP). The model station data was as reported in Li (1979). The SSME HPOTP was modeled first using beam element and second using the new shell element data contained in this thesis work. Campbell diagrams were then plotted for both runs. The critical frequencies of the two methods were then compared. A representative mode shape was also plotted for comparison.

5.5.1 60° Cone Test Piece

The 60° cone test piece of Beamish et al., (1988) is illustrated in Fig. 63. The experimental test fundamental mode natural frequency was 788 hertz. Beamish et al., (1988) reported 3231 hertz when modeled with infinite stepped beams and 791 hertz when modeled with shell flexibilities by the frequency method. For this report, the cone was first modeled with three stepped discrete A.S.M. beams as shown in Fig. 64. The station data was input to the Kelly (1989) transfer matrix rotordynamic analysis program. The fundamental first mode natural frequency by this stepped beam method was 2378 hertz. The cone was then modeled with the new shell flexibility coefficients. The shell flexibility coefficients were obtained by interpolating directly off the plots of design data figures 28 through 47. The station data was again input to the Kelly (1989) program but with the new shell flexibility coefficients. The fundamental natural frequency by this shell element transfer matrix method was 734 hertz. The corresponding fundamental mode shapes for both methods along with the test mode shape of Beamish et al., (1988) are plotted in Fig. 65. There are large differences between the natural frequencies predicted using discrete beams and the natural frequencies predicted using the shell element data of this report. This shows that the beam modeling is inadequate for conical shell sections.

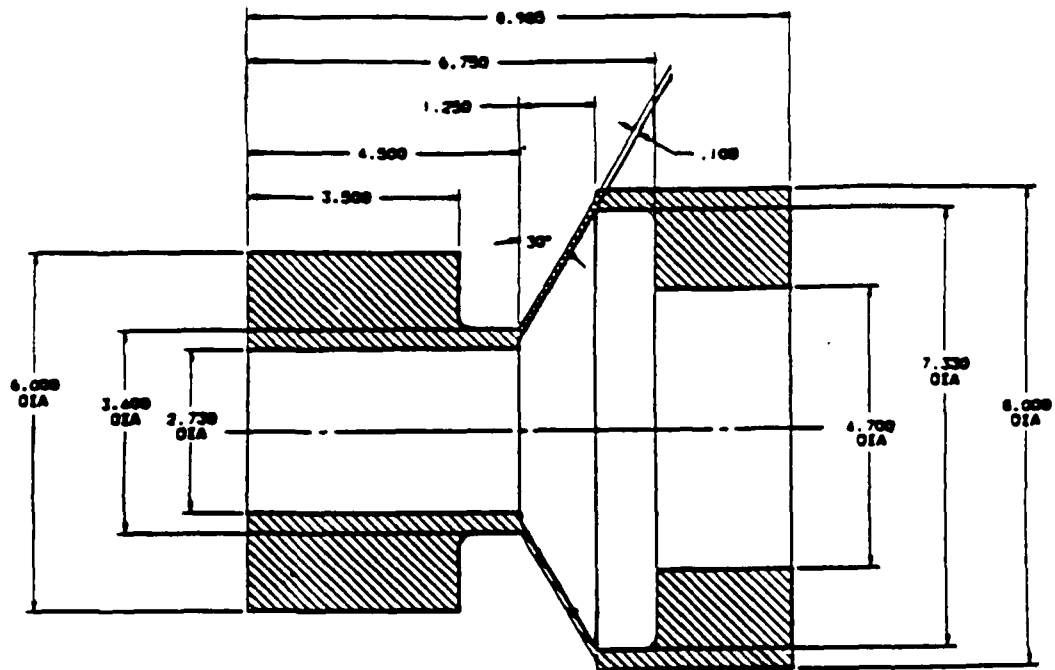


Fig. 63. 60° cone test piece with dimensioning.

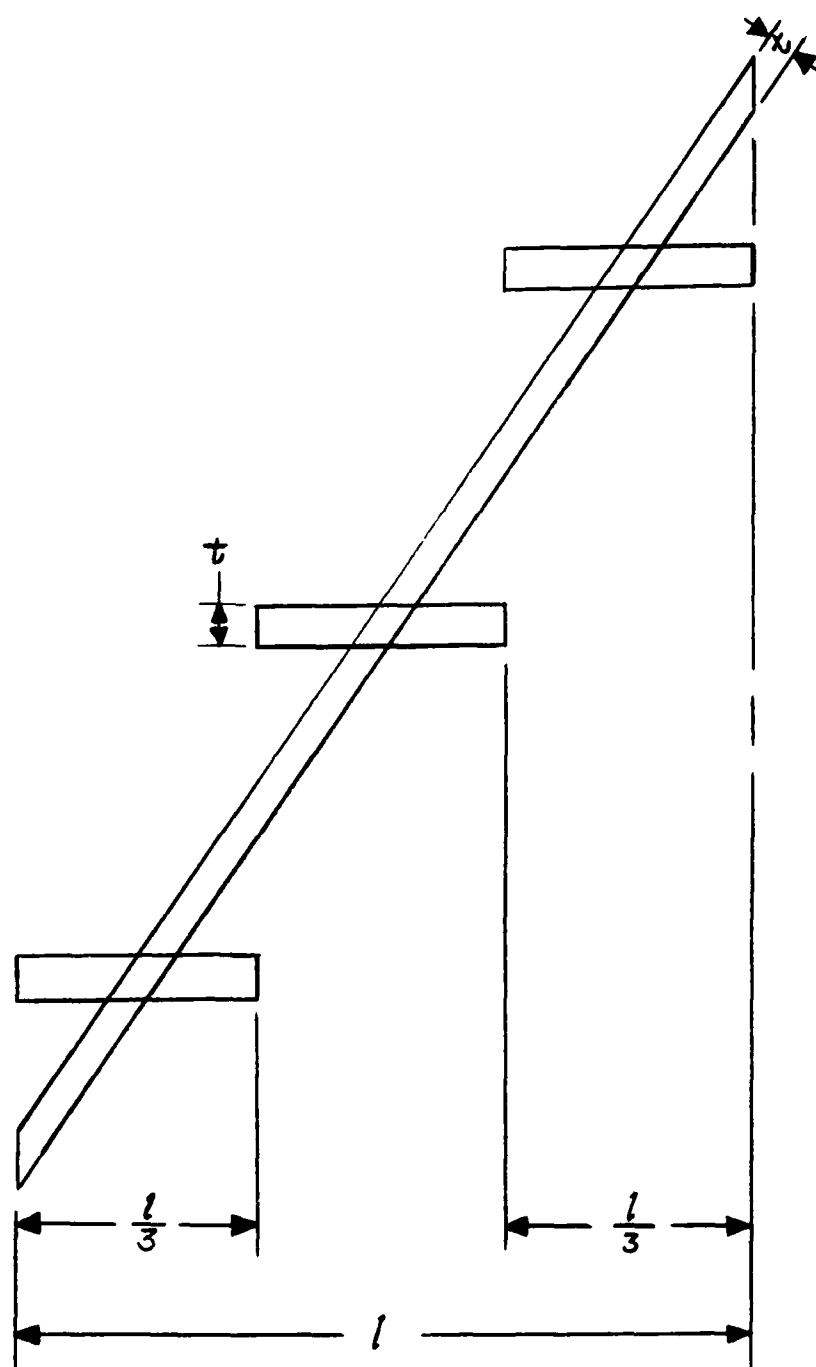


Fig. 64. Three stepped beam model of the 60° cone test piece.

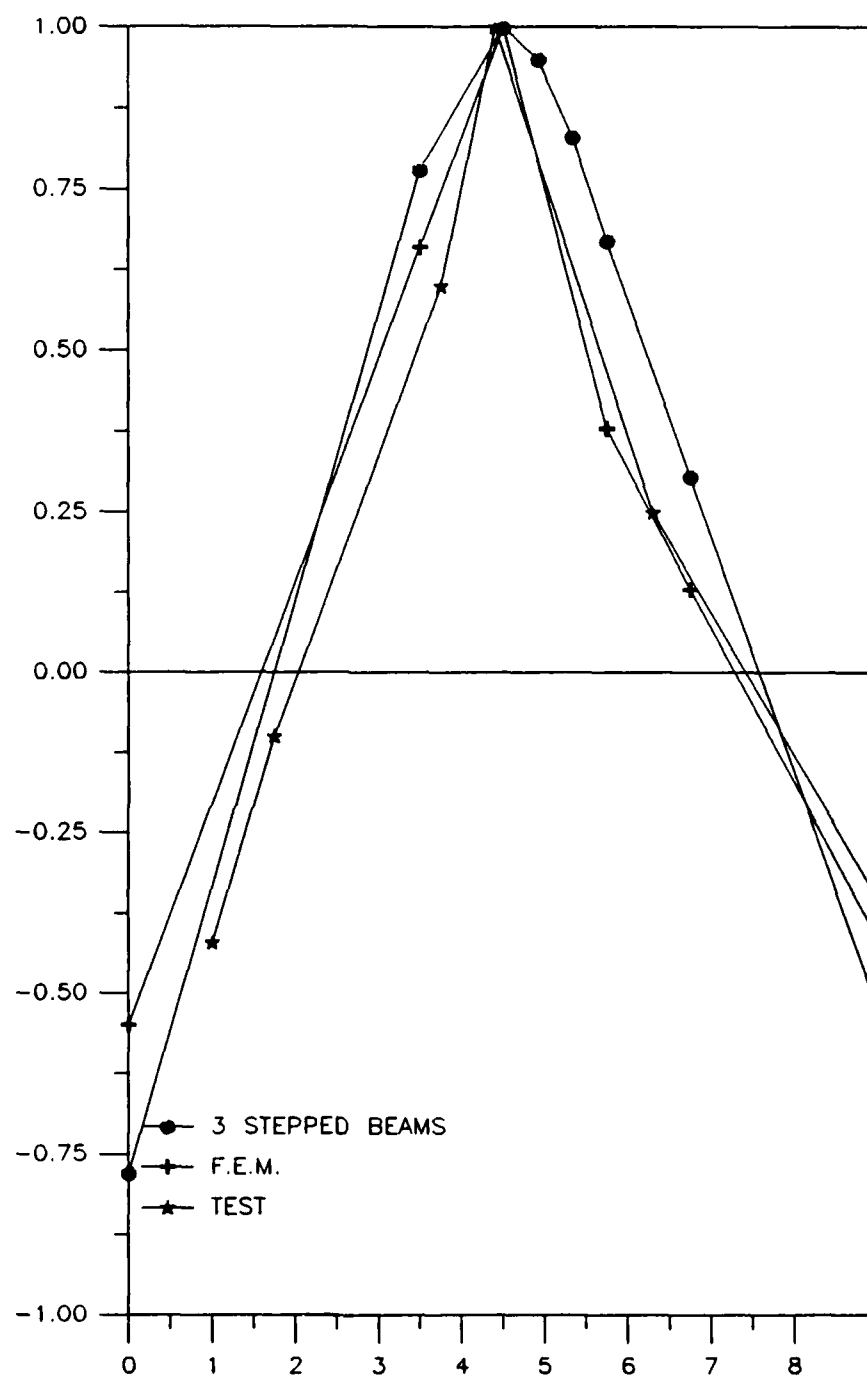


Fig. 65. Cone test piece fundamental mode shape. (Test frequency = 788 Hz. Stepped beams frequency = 2379 Hz. Shell element transfer matrix method frequency = 734 Hz.)

5.5.2 Space Shuttle Main Engine High Pressure Oxidizer Turbopump (SSME HPOTP)

The SSME HPOTP illustrated in Fig. 66 was modeled using the station data as reported in Li (1979). It was first modeled as A.S.M. beam elements input to the Kelly (1989) program. The model was run for eight different rotor running speeds as shown by the data points of the Campbell diagram of Fig. 67. The SSME HPOTP was then modeled with the cylindrical shell flexibilities interpolated off the plots of figures 48 through 62. The model was run for the same eight rotor running speeds as the previous beam elements model. A Campbell diagram was plotted for these runs as shown in Fig. 68. In Table 30, the critical speeds are listed as predicted by both models. It is important to note, for the low natural frequencies, no significant difference between the two methods. However, it is very important to note that as shown in sections 5.3 and 5.4, there are no significant differences between the A.S.M. flexibilities and S.F.E.M. flexibilities for cylindrical sections. Both models here are based on the Li (1979) station data. Li (1979) had reduced the conical sections to cylindrical sections. If the SSME HPOTP was modeled with conical sections as conical sections with the shell flexibilities, differences in predicted critical speeds would be expected. However, the impact on the predicted critical speed for this specific engine using S.F.E.M. in place of the beams has not been determined. The mode shapes of the 9,286 rpm critical speed are plotted for both the A.S.M. and the shell finite element transfer matrix methods on Fig. 69. Again, for the cylindrical sections and lower critical speeds, the A.S.M. method is quite accurate.

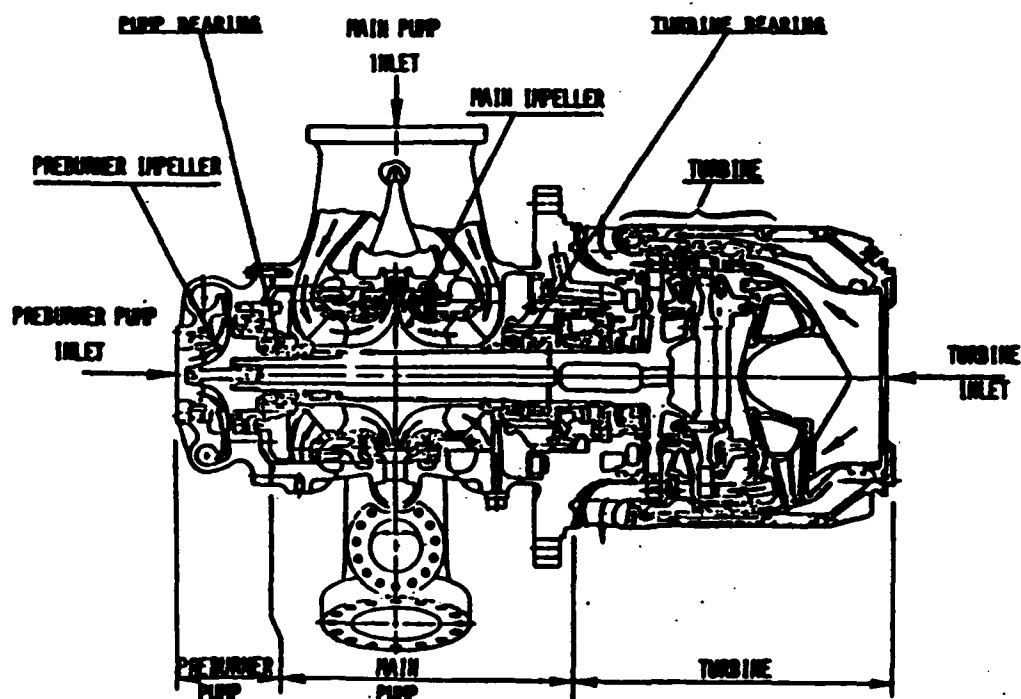


Fig. 66. Space Shuttle Main Engine High Pressure Oxidizer Turbopump Assembly (SSME HPOTP).

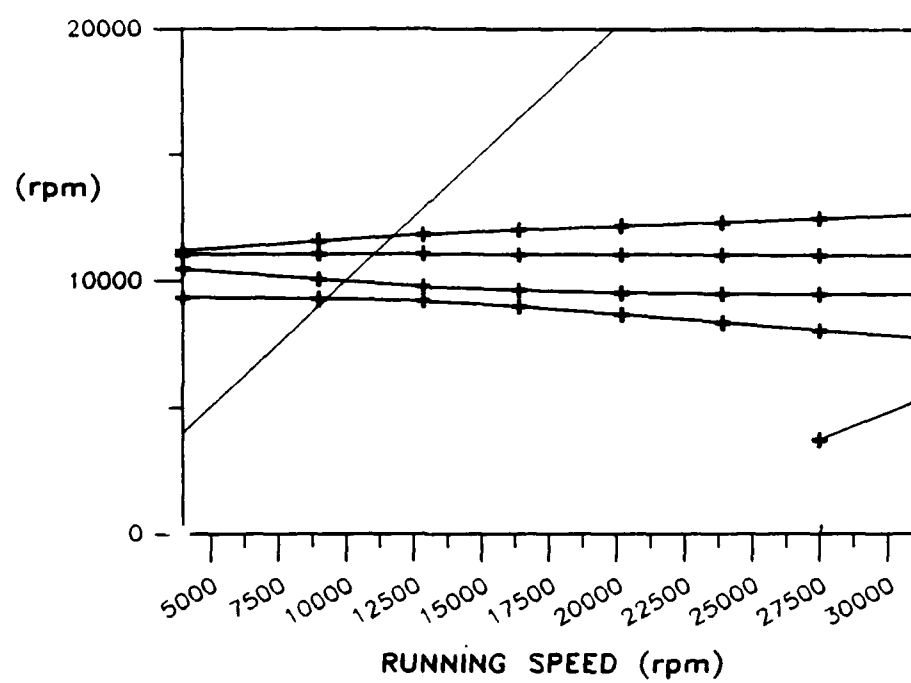


Fig. 67. Campbell diagram for the A.S.M. method.

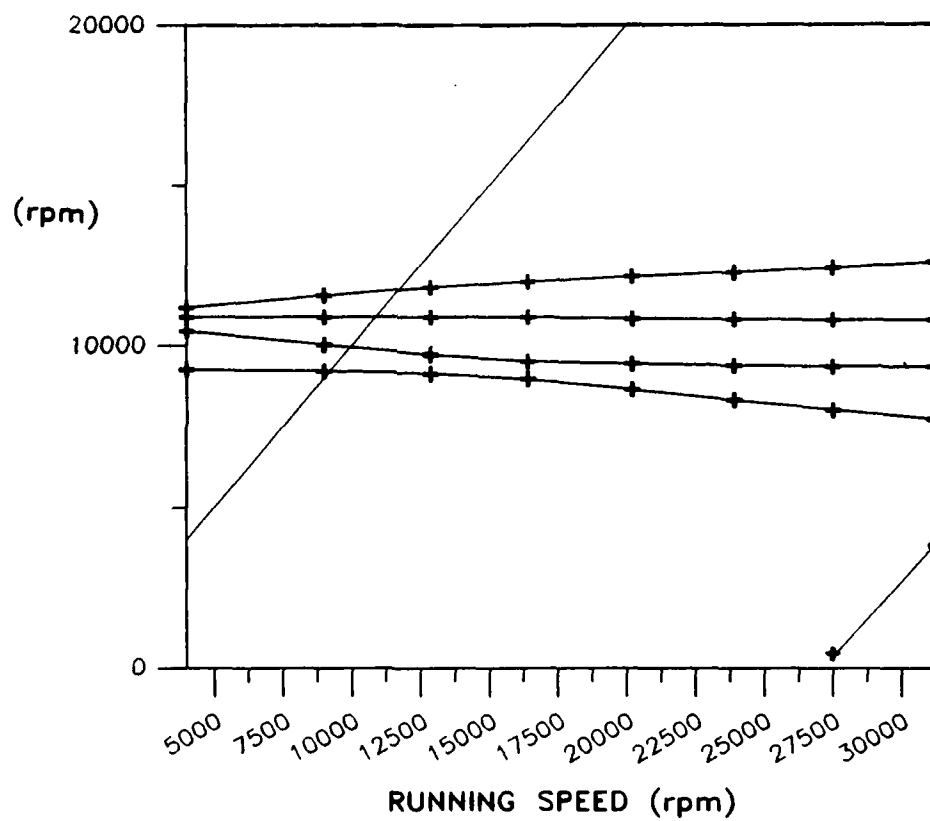


Fig. 68. Campbell diagram for the shell element transfer matrix method.

Table 30. SSME HPOTP Critical Speeds Comparison
between the A.S.M.Method and the Shell Element
Transfer Matrix Method.

Critical Speed Critical	Beam Theory A.S.M. Critical Speed (rpm)	Shell Theory S.E.T.M. Critical Speed (rpm)
1	9,286	9,286
2	10,000	10,000
3	11,116	10,870
4	11,785	11,786

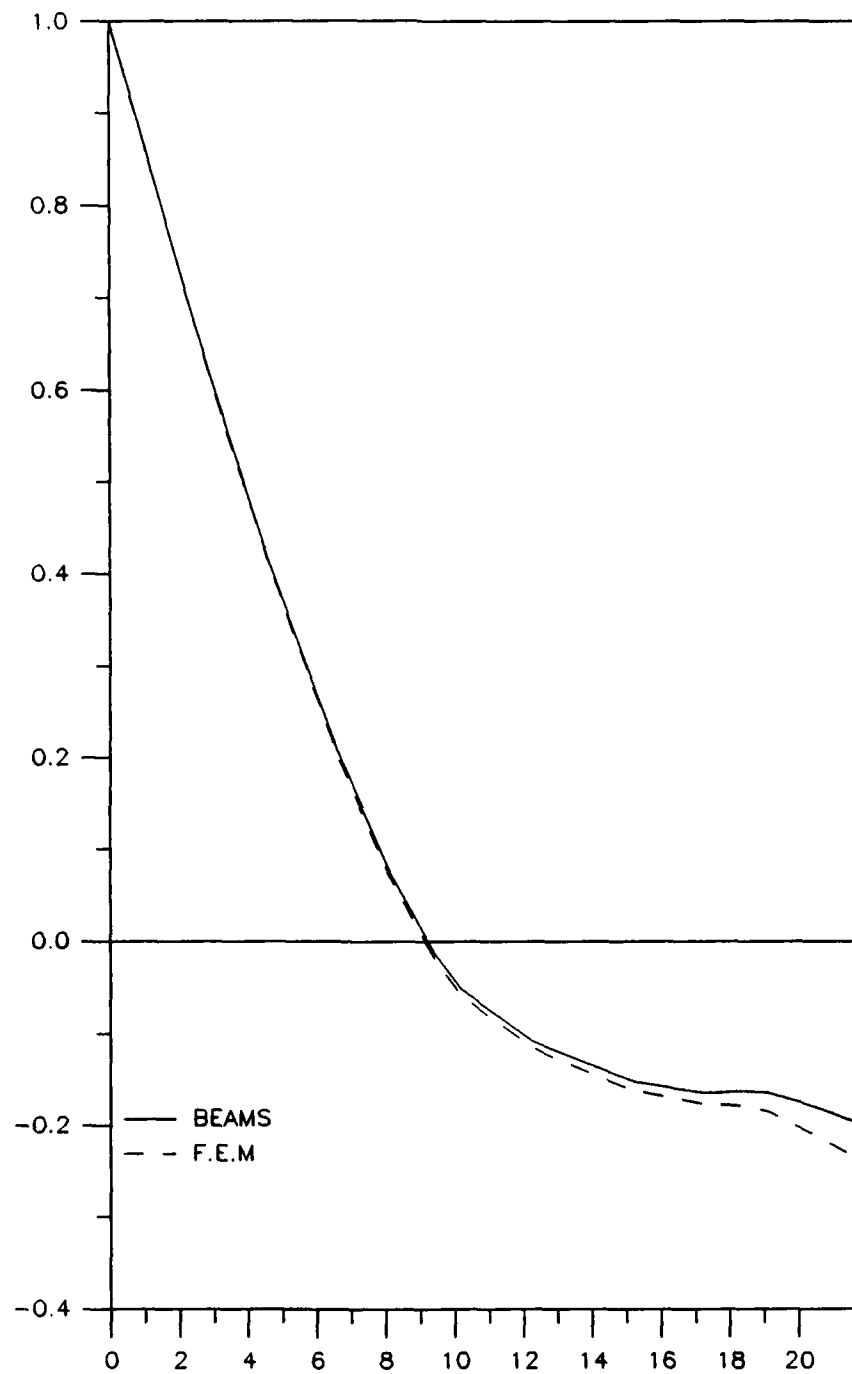


Fig. 69. SSME HPOTP 9000 rpm mode shape.

6. CONCLUSION

Design data in tabular and plot form were developed using shell finite elements. The design data are in nondimensionalized form for ready and easy use by turbomachinery design engineers and analysts. The ovalization of thin and thick-walled cylindrical and conical engine sections was determined to have a negligible effect on rotordynamics applications. The nondimensionalized design data generated are functions of conical section axial length, small end radius, wall thickness, cone angle and Young's modulus of elasticity. The nondimensionalized parameters of these sections cover the complete range of rotors, casings, and housings used throughout the turbomachinery industry. The design data are presented in the form of flexibility coefficients which should be input to the transfer matrix analysis. The need for these flexibility coefficients to be used in the current day transfer matrix computer programs has been demonstrated.

It is highly recommended that these design data be incorporated into the existing computer codes for transfer matrix analysis. The computer codes should also be modified to include a numerical interpolation scheme to generate flexibilities which lie between the tabulated computational design data points contained herein. Because the closed form advanced strength of materials beam theory is quite accurate for many cylindrical geometries, the computer codes should be modified to allow the code to choose between using the A.S.M. beam closed form or the new shell flexibility design data. With these design data shell flexibilities included in the transfer matrix analysis, the accuracy and range of application for turbomachinery is greatly improved.

REFERENCES

- ANSYS Engineering Analysis System Instruction and Theoretical Manuals, 1988, Swanson Analysis Systems, Inc., P.O. Box 65, Houston, Pennsylvania, 15342.
- Antonenko, E.V., 1981, "Accounting for Axis Curvature in Calculating the Strength of a Circular Cylindrical Shell," *Soviet Applied Mechanics* (English Translation of *Prikladnaya Mekhanika*) Vol. 17, No. 5, pp. 470-474.
- Batoz, J.L., Bathe, K.J., Ho, L.W., 1980, "A Study of Three-Node Triangular Plate Bending Elements," *International Journal of Numerical Methods in Engineering*, Vol. 15, pp. 1771-1812.
- Beamish, D.C., Ma, P., 1986, "A Method of Determining the Stiffness of Conical Sections for Rotor Dynamics Analysis," presented at the 9th NRC Machinery Dynamics Seminar, Montreal, Canada.
- Beamish, D.C., Ma, P., 1988, "Modelling of Conical Sections in Transfer Matrix Rotor Dynamics Analysis," 14th Machinery Dynamics Seminar, Edmonton, Alberta.
- Becker, K.H., Steinhardt, E., 1988, "A General Method for Rotordynamic Analysis," NATO/Advanced Study Institute, Troia Beach, Portugal.
- Brazier, L.G., 1927, "On The Flexure of Thin Cylindrical Shells and other "Thin" Sections," R.&M. No. 1081, British A.R.C. (also) *Proceedings of the Royal Society*, London, Ser. A, Vol. 116, pp. 104-114.

Bushnell, D., 1981, "Buckling of Shells-Pitfall for Designers," *AIAA Journal*, Vol. 19, No. 9, pp. 1183-1226.

Gerard, G., Becker, H., 1968, "Handbook of Structural Stability Part III—Buckling of Curved Plates and Shells," NACA T.N. No. 3783.

Greenhill, L.M., Bickford, W.B., Nelson, H.D., 1985, "A Conical Beam Finite Element for Rotor Dynamics Analysis," *ASME Journal of Vibration, Acoustics, Stress and Reliability in Design*, Vol. 107, pp. 421-430.

Gupta, A.K., 1986, "Finite Element Analysis of Vibration of Tapered Beams," *Shock and Vibration Digest*, Vol. 18, No. 5, pp. 3-6.

Hibner, D.H., 1975, "Dynamic Response of Viscous Damped Multi-Shaft Jet Engines," *Journal of Aircraft*, Vol. 12, No. 4.

Kelly, J.H., 1989, "Analysis of Multi-Stage Centrifugal Pumps using Transfer Matrices," Texas A&M University, M.S. Thesis.

Koenig, E.C., 1961, "Analysis for Calculating Lateral Vibration Characteristics of Rotating Systems with Any Number of Flexible Supports; Part I—Method of Analysis," *ASME Journal of Applied Mechanics*, Vol. 28, pp. 585-590.

Li, D.F., 1979, "Dynamic Analysis of Complex Multi-Level Flexible Rotor Systems," University of Virginia, Ph.D. Thesis.

Lund, J.W., Orcutt, F.K., 1967, "Calculations and Experiments on the Unbalance Response of a Flexible Rotor," *ASME Journal of Engineering for Industry*, pp. 785-791.

Lundquist, E.E., 1933, "Strength Tests of Thin-Walled Duralumin Cylinders in Pure Bending," NACA T.N. No. 479.

Lundquist, E.E., 1935, "Strength Tests in Thin-Walled Duralumin Cylinders in Combined Transverse Shear and Bending," NACA T.N. No. 523.

Myklestad, N.O., 1944, "A New Method for Calculating Natural Modes of Uncoupled Bending Vibrations of Airplane Wings and Other Types of Beams," *Journal of Aeronautical Sciences*, Vol. 11, pp. 153-162.

Nelson, H.D., 1980, "A Finite Rotating Shaft Element Using Timoshenko Beam Theory," *Journal of Mechanical Design*, Vol. 102, pp. 793-803.

Osgood, W.R., 1938, "The Crinkling Strength and The Bending Strength of Round Aircraft Tubing," NACA Report No. 632.

Prohl, M.A., 1945, "A General Method for Calculating Critical Speeds of Flexible Rotors," *Journal of Applied Mechanics*, Vol. 67, pp. 142-148.

Razzaque, A., 1984, "On the Four Noded Discrete Kirchhoff Shell Elements," Robinson, J. (ed.), "Accuracy Reliability Training in F.E.M. Technology," pp. 473-483.

Roark, R.J., 1941, "Stresses and Deflections in Thin Shells and Curved Plates Due to Concentrated and Variously Distributed Loading," NACA T.N. No. 806.

Rouch, K.E., Kao, J.S., 1979, "A Tapered Beam Finite Element for Rotor Dynamics Analysis," *Journal of Sound and Vibration*, Vol. 66, No. 1, pp. 119-140.

Sevcik, J.K., 1963, "System Vibration and Static Analysis," ASME Paper 63-AHGT-57, Gas Turbine Conference, Los Angeles, CA.

Stephens, W.B., Starnes, J.H. Jr., Almroth, B.O., 1975, "Collapse of Long Cylindrical Shells Under Combined Bending and Pressure Loads," *AIAA Journal*. Vol.13, No.1, pp.20-25.

Thompson, B.D., Badgley, R.H., 1988, "Application of An Advanced Hybrid Rotordynamics Model to the Complete Structure of a Marine Gas Turbine Engine." ASME Gas Turbine Conference, Honolulu, HI.

Timoshenko, S.P., Woinowsky-Krieger, S., 1959, "Theory of Plates and Shells," 2nd ed., McGraw-Hill Book Company, U.S.A., pp.447-449.

To, C.W.S., 1981, "A Linearly Tapered Beam Finite Element Incorporating Shear Deformation and Rotary Inertia for Vibration Analysis," *Journal of Sound and Vibration*. Vol.78, No.4, pp.475-484.

Tuma, J.J., 1969. "Theory and Problems of Structural Analysis," 1st ed., McGraw-Hill Book Company, U.S.A., pp.167-168.

Wilson, W.M., Olson, E.D., 1941, "Tests of Cylindrical Shells," University of Illinois Engineering Experiment Station, Bulletin Series No.331.

Zienkiewicz, O.C., 1977, "The Finite Element Method," McGraw-Hill Book Company, London.

APPENDIX A

Derivation of Equations (1) and (2)

Referring to the general shaft element of Fig. 1, the load-displacement relationships can be developed. By first summing forces in the y direction,

$$V_{i-1} - V_i = 0 \quad , \quad V_i = V_{i-1} \quad (A1)$$

and by summing moments about the right end,

$$M_i = M_{i-1} + V_{i-1}l \quad (A2)$$

By solving for the radial displacement at the right end,

$$Y_i = Y_{i-1} + \theta_{i-1}l + M_i(f_{y\theta}) - V_i(f_{yy}) \quad (A3)$$

and for the angular displacement at the right end,

$$\theta_i = \theta_{i-1} + M_i(f_{\theta\theta}) - V_i(f_{\theta y}) \quad (A4)$$

By substituting (A1) and (A2) into (A3) and (A4) respectively,

$$Y_i = Y_{i-1} + \theta_{i-1}l + M_{i-1}(f_{y\theta}) + V_{i-1}l(f_{y\theta}) - V_{i-1}(f_{yy}) \quad (A5)$$

$$\theta_i = \theta_{i-1} + M_{i-1}(f_{\theta\theta}) + V_{i-1}l(f_{\theta\theta}) - V_{i-1}(f_{\theta y}) \quad (A6)$$

where $f_{y\theta}$ is defined as the flexibility of the structure for the radial deflection under bending moment loading. f_{yy} is defined as the flexibility of the structure for the radial deflection under shear loading. $f_{\theta\theta}$ is defined as the flexibility of the structure for the rotational deflection under bending moment loading. $f_{\theta y}$

is defined as the flexibility of the structure for the rotational deflection under shear loading.

Assembling equations (A1), (A2), (A5) and (A6) into matrix form to be used in computational analysis, equation (2) of the main text is derived,

$$\begin{Bmatrix} Y_i \\ \theta_i \\ M_i \\ V_i \end{Bmatrix} = \begin{bmatrix} 1 & l & f_{y\theta} & l(f_{y\theta}) - f_{yy} \\ 0 & 1 & f_{\theta\theta} & l(f_{\theta\theta}) - f_{\theta y} \\ 0 & 0 & 1 & l \\ 0 & 0 & 0 & 1 \end{bmatrix} \begin{Bmatrix} Y_{i-1} \\ \theta_{i-1} \\ M_{i-1} \\ V_{i-1} \end{Bmatrix} \quad (2)$$

Now, by defining the transfer matrix flexibility coefficients as;

$$\begin{aligned} a &= l(f_{y\theta}) - f_{yy} \\ b &= f_{y\theta} \\ \alpha &= l(f_{\theta\theta}) - f_{\theta y} \\ \beta &= f_{\theta\theta} \end{aligned} \quad (A7)$$

We can by substitution show the general form of the field transfer matrix in terms of the defined flexibility coefficients which is equation (1) of the main text,

$$\begin{Bmatrix} Y_i \\ \theta_i \\ M_i \\ V_i \end{Bmatrix} = \begin{bmatrix} 1 & l & b & a \\ 0 & 1 & \beta & \alpha \\ 0 & 0 & 1 & l \\ 0 & 0 & 0 & 1 \end{bmatrix} \begin{Bmatrix} Y_{i-1} \\ \theta_{i-1} \\ M_{i-1} \\ V_{i-1} \end{Bmatrix} \quad (1)$$

Assembly of Equation (3)

For the Timoshenko beam element, the flexibility equations derived by advanced strength of materials are;

$$\begin{aligned} f_{y\theta} &= f_{\theta y} = \frac{l^2}{2EI} \\ f_{yy} &= \frac{l^3}{3EI} + \frac{l}{GA_c K_s} \\ f_{\theta\theta} &= \frac{l}{EI} \end{aligned} \quad (A8)$$

where the shear form factor is

$$K_s = \frac{6(1 + \nu)(1 + \frac{r_1}{r_o})^2}{(7 + 6\nu)(1 + \frac{r_1}{r_o})^2 + (20 + 12\nu)(\frac{r_1}{r_o})^2} \quad (A9)$$

By substituting the expressions of (A8) into the expressions of (A7) and substituting again into equation (1), the general field transfer matrix for a beam element becomes equation (3) of the main text,

$$\begin{Bmatrix} Y_i \\ \theta_i \\ M_i \\ V_i \end{Bmatrix} = \begin{bmatrix} 1 & l & \frac{l^2}{2EI} & \frac{l^3}{6EI} - \frac{l}{GA_c K_s} \\ 0 & 1 & \frac{l}{EI} & \frac{l^2}{2EI} \\ 0 & 0 & 1 & l \\ 0 & 0 & 0 & 1 \end{bmatrix} \begin{Bmatrix} Y_{i-1} \\ \theta_{i-1} \\ M_{i-1} \\ V_{i-1} \end{Bmatrix} \quad (3)$$

APPENDIX B

Derivation of Equations (4) through (10)

Recalling equation (1) for the general shaft element of Fig. 1,

$$\begin{Bmatrix} Y_i \\ \theta_i \\ M_i \\ V_i \end{Bmatrix} = \begin{bmatrix} 1 & l & b & a \\ 0 & 1 & \beta & \alpha \\ 0 & 0 & 1 & l \\ 0 & 0 & 0 & 1 \end{bmatrix} \begin{Bmatrix} Y_{i-1} \\ \theta_{i-1} \\ M_{i-1} \\ V_{i-1} \end{Bmatrix} \quad (1)$$

By applying the cantilevered boundary conditions used for multiple station transfer matrix analysis;

$$\begin{aligned} Y_{i-1} &= 0 \\ \theta_{i-1} &= 0 \end{aligned} \quad (B1)$$

and by first applying a shear tip load, V_i , with no bending moment tip load, M_i , the force-displacement relationships can be written. First summing the forces in the y direction,

$$V_{i-1} - V_i = 0 \quad , \quad V_i = V_{i-1} \quad (B2)$$

and by summing moments about the left end,

$$M_{i-1} - V_i l = 0 \quad , \quad M_{i-1} = -V_i l \quad (B3)$$

Now substituting (B2) and (B3) into (1) and solving for the displacements,

$$\begin{aligned} Y_i &= aV_i - bV_i l \\ \theta_i &= \alpha V_i - \beta V_i l \end{aligned} \quad (B4)$$

and solving for the flexibilities a and α ,

$$\begin{aligned} a &= \frac{Y_i}{V_i} + bl \\ \alpha &= \frac{\theta_i}{V_i} + \beta l \end{aligned} \quad (B5)$$

For a unit shear load,

$$\begin{aligned} a &= Y_i + bl \\ \alpha &= \theta_i + \beta l \end{aligned} \quad (B6)$$

By defining Y_v and θ_v as the radial and rotational displacements respectively of the right end due to a shear tip load and no moment load, then the flexibilities become

$$\begin{aligned} a &= Y_v + bl \\ \alpha &= \theta_v + \beta l \end{aligned} \quad (B7)$$

Now applying a bending moment tip load, M_i , with no shear tip load, V_i , the force-displacement relationships can be written. First summing the forces in the y direction,

$$V_{i-1} - V_i = 0 \quad , \quad V_{i-1} = V_i = 0 \quad (B8)$$

and by summing moments about the left end,

$$M_{i-1} - M_i = 0 \quad , \quad M_{i-1} = M_i \quad (B9)$$

Now substituting (B8) and (B9) into (1) and solving for the displacements,

$$\begin{aligned} Y_i &= bM_i \\ \theta_i &= \beta M_i \end{aligned} \quad (B10)$$

and by defining Y_m and θ_m as the radial and rotational displacements respectively of the right end due to a bending moment tip load and no shear tip load, then

$$\begin{aligned} Y_m &= bM_i \\ \theta_m &= \beta M_i \end{aligned} \quad (B11)$$

For a unit load, equations (5) and (7) of the main text are written as

$$b = Y_m \quad (5)$$

$$\beta = \theta_m \quad (7)$$

By substituting (5) and (7) into (B7), equations (4) and (6) are written as

$$a = l(Y_m) + Y_v \quad (4)$$

$$\alpha = l(\theta_m) + \theta_v \quad (6)$$

Now recalling from advanced strength of materials for a Timoshenko beam element with unit loads applied in turn, the flexibilities become;

$$\begin{aligned} Y_m = -\theta_v &= \frac{l^2}{2EI} \\ Y_v &= -\frac{l^3}{3EI} - \frac{l}{GA_c K_s} \\ \theta_m &= \frac{l}{EI} \end{aligned} \quad (B12)$$

and substituting the equations of (B12) into (4) through (7), the flexibility coefficients for a beam element become equations (8), (9) and (10) of the main text,

$$a = \frac{l^3}{6EI} - \frac{l}{GA_c K_s} \quad (8)$$

$$b = \alpha = \frac{l^2}{2EI} \quad (9)$$

$$\beta = \frac{l}{EI} \quad (10)$$

APPENDIX C

Derivation of Equations (11) through (14)

Recall the general structure element of Fig. 1. By fixing the opposite end (i) and loading the new rigid end ($i-1$) so that the same load end conditions exist on the general structure element as before, then the same strain energy state exists and the following analysis can be applied. (See Fig. 70 for an illustration of the general structure element now in the negative attitude.)

By summing forces in the y direction,

$$V_{i-1} - V_i = 0 \quad , \quad V_{i-1} = V_i \quad (C1)$$

and by summing moments about the right end,

$$M_{i-1} + l(V_i) - M_i = 0 \quad , \quad M_{i-1} = M_i - l(V_i) \quad (C2)$$

Solving for the displacements at the right end ($i-1$),

$$\begin{aligned} Y_{i-1} &= Y_i - l(\theta_i) + M_{i-1}(f_{y\theta})_n + V_{i-1}(f_{yy})_n \\ \theta_{i-1} &= \theta_i - M_{i-1}(f_{\theta\theta})_n - V_{i-1}(f_{\theta y})_n \end{aligned} \quad (C3)$$

where "n" denotes the flexibility when loaded in the negative attitude. By assembling into matrix form and isolating the flexibility coefficients in order to obtain the flexibility transformation matrix,

$$\begin{Bmatrix} Y_{i-1} \\ \theta_{i-1} \end{Bmatrix} = \begin{bmatrix} 1 & -l \\ 0 & 1 \end{bmatrix} \begin{Bmatrix} Y_i \\ \theta_i \end{Bmatrix} + \begin{bmatrix} (f_{y\theta})_n & (f_{yy})_n \\ -(f_{\theta\theta})_n & -(f_{\theta y})_n \end{bmatrix} \begin{Bmatrix} M_{i-1} \\ V_{i-1} \end{Bmatrix} \quad (C4)$$

Recalling for a general structural element that;

$$\begin{aligned} a &= l(f_{y\theta}) - f_{yy} \\ b &= f_{y\theta} \\ \alpha &= l(f_{\theta\theta}) - f_{\theta y} \\ \beta &= f_{\theta\theta} \end{aligned} \quad (A7)$$

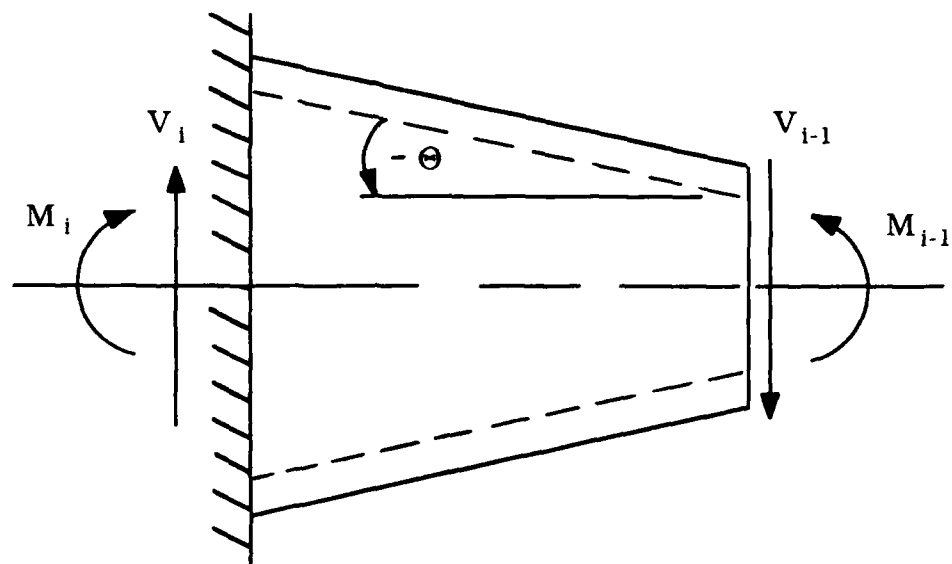


Fig.70. Cone with negative attitude loading for the transformation identities development.

substituting "n" for the negative attitude structure but loaded as in Fig. 1, and solving for the flexibilities,

$$\begin{aligned}
 (f_{y\theta})_n &= b_n \\
 (f_{\theta\theta})_n &= \beta_n \\
 (f_{yy})_n &= l(b_n) - a_n \\
 (f_{\theta y})_n &= l(\beta_n) - \alpha_n
 \end{aligned} \tag{C5}$$

By substituting (C5) into (C4),

$$\begin{Bmatrix} Y_{i-1} \\ \theta_{i-1} \end{Bmatrix} = \begin{bmatrix} 1 & -l \\ 0 & 1 \end{bmatrix} \begin{Bmatrix} Y_i \\ \theta_i \end{Bmatrix} + \begin{bmatrix} b_n & l(b_n) - a_n \\ -\beta_n & \alpha_n - l(\beta_n) \end{bmatrix} \begin{Bmatrix} M_{i-1} \\ V_{i-1} \end{Bmatrix} \tag{C6}$$

Solving for the displacements at end (i),

$$\begin{Bmatrix} Y_i \\ \theta_i \end{Bmatrix} = \begin{bmatrix} 1 & l \\ 0 & 1 \end{bmatrix} \begin{Bmatrix} Y_{i-1} \\ \theta_{i-1} \end{Bmatrix} - \begin{bmatrix} 1 & l \\ 0 & 1 \end{bmatrix} \begin{bmatrix} b_n & l(b_n) - a_n \\ -\beta_n & \alpha_n - l(\beta_n) \end{bmatrix} \begin{Bmatrix} M_{i-1} \\ V_{i-1} \end{Bmatrix} \tag{C7}$$

Recalling the transformation of the positive attitude general structure element, equation(1), and separating the flexibility coefficients in order to obtain the flexibility transformation matrix,

$$\begin{Bmatrix} Y_i \\ \theta_i \end{Bmatrix} = \begin{bmatrix} 1 & l \\ 0 & 1 \end{bmatrix} \begin{Bmatrix} Y_{i-1} \\ \theta_{i-1} \end{Bmatrix} + \begin{bmatrix} b_p & a_p \\ \beta_p & \alpha_p \end{bmatrix} \begin{Bmatrix} M_{i-1} \\ V_{i-1} \end{Bmatrix} \tag{C8}$$

where "p" was inserted to designate the flexibility coefficients of the positive attitude general structure element. Now subtracting (C7) from (C8),

$$\begin{bmatrix} b_p & a_p \\ \beta_p & \alpha_p \end{bmatrix} = \begin{bmatrix} 1 & l \\ 0 & 1 \end{bmatrix} \begin{bmatrix} -b_n & a_n - l(b_n) \\ \beta_n & l(\beta_n) - \alpha_n \end{bmatrix} \tag{C9}$$

Solving for the negative attitude flexibility coefficients in terms of the positive attitude flexibility coefficients,

$$\begin{aligned}
 a_n &= a_p - l(b_p) + l^2(\beta_p) - l(\alpha_p) \\
 b_n &= l(\beta_p) - b_p \\
 \alpha_n &= l(\beta_p) - \alpha_p \\
 \beta_n &= \beta_p
 \end{aligned} \tag{C10}$$

These equations represent the transformation of the flexibility coefficients of the general structure element from the positive attitude to the negative attitude.

Now for the specific case of the conical structure used in turbomachinery, because the cone is an axisymmetric structure, the flexibility matrix is symmetric, thus

$$f_{\theta y} = f_{y\theta} \quad (C11)$$

then by substituting (C11) into (A7),

$$\alpha = l\beta - b \quad (12)$$

Also,

$$\begin{aligned} \alpha_n &= l(\beta_n) - b_n \\ \alpha_p &= l(\beta_p) - b_p \end{aligned} \quad (C13)$$

and finally by substitution of (C13) into (C10), the flexibility coefficient transformation from the positive attitude of a conical element to the negative attitude of the same conical element is written as equations (11) through (14) of the main text,

$$a_n = a_p \quad (11)$$

$$b_n = \alpha_p \quad (12)$$

$$\alpha_n = b_p \quad (13)$$

$$\beta_n = \beta_p \quad (14)$$

APPENDIX D

```

C*****
C
C   ANSYS EXAMPLE INPUT FILE
C   EDWARD ANTHONY L'ANTIGUA
C   TEXAS A&M UNIVERSITY
C*****
/PREP7
/TITLE,ROTOR WITH SHELL ELEMENTS
C
C   SELECT SHELL ELEMENT
C
ET,1,63
C
C   SELECT MATERIAL PROPERTIES
C   YOUNG'S MODULUS,POISSON'S RATIO
C
EX,1,30E6
NUXY,1,0.3
C
C   INPUT STRUCTURE GEOMETRY
C   GENERATE KEYPOINTS
C   GENERATE LINE SEGMENTS
C   GENERATE AREAS
C
R,1,3,2
K,1,0,16
K,2,4,30.9282
K,3,8,45.8564
L,1,2
L,2,3
K,1000,0,0
K,1001,1,0
AROTAT,1,2,.,.,.,1000,1001,360,4
C
C   MESH GENERATION
C
ELSIZE,.6
AMESH,ALL
C
C   FIX ALL LEFT END NODES
C
NRSEL,X,0
D,ALL,ALL
NALL
C
C   CREATE INFINITELY RIGID RIGHT END
C   BY USING D.O.F. CONSTRAINT EQUATIONS
C
CERIG,1,2
CERIG,1,3
CERIG,1,4
CERIG,1,5
CERIG,1,6
CERIG,1,7
CERIG,1,92
CERIG,1,93
CERIG,1,94
CERIG,1,95
CERIG,1,96
CERIG,1,97

```

```

CERIG,1,170
CERIG,1,171
CERIG,1,172
CERIG,1,173
CERIG,1,174
CERIG,1,175
CERIG,1,248
CERIG,1,249
CERIG,1,250
CERIG,1,251
CERIG,1,252
C
C   APPLY RIGHT END LOADING
C
NRSEL,X,8
NRSEL,Y,0
F,ALL,FY,-0.5
NALL
C
C   REORDER SOLUTION WAVEFRONT IN ORDER TO
C   MINIMIZE MATRIX SIZE AND SOLUTION TIME
C
WSORT,X
WSTART
WAVES
C
C   ONE ITERATION FOR LINEAR SOLUTION
C
ITER,1
AFWRIT
FINISH
/EXE
/INPUT,27
FINISH
/EOF
C
C   POST PROCESSING DATA COLLECTION
C
/POST1
/OUTPUT,6
SET,1,1,1
C
C   SELECT MIDLENGTH NODAL DISPLACEMENTS
C   TO CHECK FOR ANY OVALIZATION
C
NRSEL,X,4
NRSEL,Y,0
PRNODE
PLDISP
NALL
NRSEL,X,4
NRSEL,Z,0
PRNODE
PLDISP
NALL
C
C   SELECT END NODAL DISPLACEMENTS TO
C   DETERMINE FLEXIBILITY COEFFICIENTS
C
NRSEL,X,8
NRSEL,Y,0
PRNODE
PLDISP
NALL
NRSEL,X,8
NRSEL,Z,0
PRNODE
PLDISP
NALL
/OUTPUT,1
/EOF

```

VITA

Edward Anthony L'Antigua [REDACTED]

[REDACTED] After graduation from the Holliston, Massachusetts elementary and secondary school system, he entered the United States Air Force Reserve Officers Training Corps at the Georgia Institute of Technology in the fall of 1980. He received his Bachelor of Mechanical Engineering degree and commission as a Second Lieutenant in the USAF in the spring of 1984. Lieutenant L'Antigua served three and one half years as a Special Weapons and Reentry Vehicles Engineer at Kelly Air Force Base, San Antonio, Texas. He was promoted to the rank of Captain and selected for research duty at Texas A&M University to receive a Master of Science degree in Mechanical Engineering. His training at Texas A&M University was selected to prepare him for duty as an engineering instructor at the United States Air Force Academy in Colorado Springs, Colorado. The primary focus of his graduate work has been in the area of Solid Mechanics and its application to the Rotordynamics of Turbomachinery.

[REDACTED]

[REDACTED]